

Ultracold Fermionic Feshbach Molecules

by

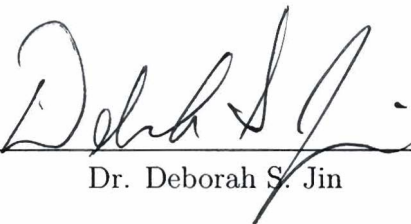
Joshua Zirbel

B.S. Physics, University of Missouri-Rolla, 2001

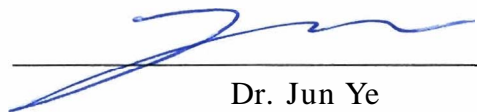
A thesis submitted to the
Faculty of the Graduate School of the
University of Colorado in partial fulfillment
of the requirements for the degree of
Doctor of Philosophy
Department of Physics

2008

This thesis entitled:
Ultracold Fermionic Feshbach Molecules
written by Joshua Zirbel
has been approved for the Department of Physics



Dr. Deborah S. Jin



Dr. Jun Ye

Date July 18, 2008

The final copy of this thesis has been examined by the signatories, and we find that both the content and the form meet acceptable presentation standards of scholarly work in the above mentioned discipline.

Zirbel, Joshua (Ph.D., Physics)

Ultracold Fermionic Feshbach Molecules

Thesis directed by Professor Dr. Deborah S. Jin

This thesis presents experiments creating heteronuclear diatomic molecules from ultracold mixtures of atomic bosons and fermions. The work presented takes advantage of a type of scattering resonance, known as a magnetic Feshbach resonance, to efficiently and selectively create the fermionic molecules. I present studies of the weakly bound, highly vibrationally excited molecules created near the Feshbach resonance. These molecules have inelastic collisions that are affected by the particular atoms involved in the collisions. Inelastic collisions are enhanced or suppressed depending on whether the colliding atoms are bosonic, fermionic, or distinguishable when compared to the molecule's constituent atoms.

Acknowledgements

This section is devoted to the long list of people who have helped me along my journey through graduate school. This list is made longer by the fact that I have had an especially long graduate career.

Of course, I must first thank my advisors. From 2001 until 2006, Carl Wieman was my first thesis advisor. I am continually impressed by his ability to find interesting problems and then find solutions to them. Deborah Jin took over our project and its students after Carl left. Even though Debbie has many obligations she always managed to find the time to help us, either directly by coming into the lab and taking data with us, or indirectly by asking probing questions. She has impressed me with her ability to cut through a problem and partition it into manageable sizes. Although we've forgiven her for being (somewhat) responsible for breaking our magnetic trap, we haven't forgotten and are ready to bring it up if ever we need a get-out-of-jail-free card! She has been incredibly patient and I can't thank her enough for all that she has done for me. Of course, I can't forget the final "Tri-group" advisor, Eric Cornell. Although he was not a direct thesis advisor to me, I thank him for giving suggestions and encouragement during my time at JILA.

The KRb molecule project was, from the beginning, a joint effort of Carl, Debbie, and Jun Ye. Jun has recently become much more involved with the experiment and it has been my pleasure to work with him. He has an infectious

optimistic attitude in spite of daunting challenges and has brilliant suggestions when it comes to almost any problem. Jun possesses a unique way of building confidence in his students by focusing on their positive attributes.

I've worked directly with a few graduate students and post-docs. Scott Papp and I worked together building up the ^{87}Rb - ^{85}Rb experiment from 2001-2003 until I moved to the ^{40}K - ^{87}Rb experiment. Scott has an unmatched intensity for physics and getting things to work. After I moved downstairs, he was always around to give his advice, solicited or otherwise! I thank him for always listening to my incessant questions regarding pretty much anything from lab stuff to life stuff. I look forward to our continued friendship. In 2003, Kang-Kuen Ni joined me in building the ^{40}K - ^{87}Rb experiment and, as a result, has contributed significantly to this thesis work. Kang-Kuen has grown into a capable researcher and, I'm proud to say, she has succeeded into my former role in the lab while doing a better job. I thank her for putting up with both my ups and downs throughout the years and for being a good friend. Travis Nicholson was our undergraduate for the early years and is responsible for building many parts of our apparatus. He is a hard worker so I suspect he'll have many successes in the future. Recently, Brian Neyenhuis has joined us. He is very talented and his pleasant style has made it easy working with him. I look forward to the seeing his future accomplishments. Silke Ospelkaus joined our lab as a post-doc in early 2007. She immediately injected her enthusiasm into the lab. With Silke's help, anything can be accomplished. This thesis would not be possible without her. It has been a pleasure becoming friends with her and her husband, Christian.

A visitor to our lab, Andrew Wilson, was particularly helpful around the lab during the early stages. He also has become a good friend I always look forward to see at various conferences and when he is in the U.S. His attempts to instill confidence in myself are greatly appreciated.

Indirectly, I've worked with many talented students and post-docs. Here is the short list, graduate students: Neil Claussen, Kurt Miller, Sarah Thompson, Jon Goldwin, Cindy Regal, Michele Olsen, Lisheng Chen, Volker Schweikhard, John Obrecht, Juan Pino, Russell Stutz, Jayson Stewart, Laura Sinclair, John Gaebler, Shihkuang Tung, Robert Wild, Tyler Cumby and post-docs: Elizabeth Donley, Stephan Dürr, Eleanor Hodby, Peter Engels, Shin Inouye, Markus Greiner, Aaron Leanhardt, Avi Pe'er, John Perreault, and Giacomo Lamporesi.

JILA has been a wonderful place to work. Part of what has made it great is how well it helps the students and faculty do tasks that might otherwise distract from science. Since I have helped build large portions of two apparatuses, I have worked closely with two shops that have helped immensely: the JILA electronic and machine shops. In particular, Terry Brown, Carl Sauer, Mike Whitmore, Blaine Horner, Hans Greene, Tracy Keep, Todd Asnicar, Tom Foote, and Kim Hagen have been helpful with suggestions and in building many components of our apparatus. In addition to the technical expertise at JILA, the support staff has been invaluable. These staff include those working in the supply office or those assisting the fellows. In particular, Krista Beck has provided me with much assistance over the years while she was an assistant to Carl and Debbie.

My family has been instrumental in developing my ability to make it to this point. I thank my parents for cultivating my desire to ask questions and helping me find some of the answers. My mother, Donna Zirbel, always entertained us with simple head-to-head strategy games. Using these games she would get us to work by having the loser do a chore. I wish work could always be as fun now as it was then. Having a father, James Zirbel, who tried and succeeded in fixing nearly everything gave me many opportunities to see the insides of mechanical things, from boilers, cars, and washing machines to surplus He:Ne laser bar-code scanners. His fix-it-all mentality gave me a sense that almost everything can be

understood and then repaired with the right tools. I thank my sister, Angela Pulfer, for putting up with her kid-brother and giving him the chance to sponge off of her knowledge. My grandmother, Jeanette West, always encouraged me to pursue an education and tried to teach me that almost anything is achievable with adequate preparation and a healthy body & mind. I thank my grandfather, Theodore Morris, for always giving me a history lesson about his experiences during WWII and for teaching me what he could about airplanes, finance, and friendship.

I would also like to thank my teachers and professors before graduate school. In particular I thank: Karen Harrison, Don Sparlin, Gerald Wilemski, Ron Bieniek and Paul Parris.

Finally, I thank all of my friends. In particular I thank Anne Kellerman for giving good advice, sharing her good cooking, & being my biking buddy and Zane Altman for providing encouragement & companionship while writing this thesis.

Contents

Chapter

1	Introduction	1
1.1	KRb Molecules	1
1.2	Why Ultracold Molecules?	2
1.3	Making Ultracold Molecules	3
1.4	History of Ultracold Mixtures of Alkali Atoms	4
1.5	Thesis Outline	5
2	Apparatus	7
2.1	Introduction and Overview	7
2.2	Laser Systems for the Atoms	9
2.2.1	The MOTs	12
2.3	Vacuum Chamber	12
2.3.1	MOT Region	14
2.3.2	Transfer Tube	19
2.3.3	Science Cell	20
2.4	Magnetic Traps and Fields	20
2.4.1	Quadrupole and Transfer Trap	21
2.4.2	Ioffe-Pritchard Trap	21
2.4.3	Oscillating Magnetic Fields	25

2.5	Optical Trap	26
2.6	Imaging System	26
2.7	Computer Control	28
3	Methods	29
3.1	Introduction to Methods	29
3.2	The MOT	30
3.3	The Transfer	31
3.4	IP Evaporation	35
3.5	Optical Trap Evaporation	37
3.6	Absorption Imaging	39
4	Creation of Feshbach Molecules	40
4.1	Feshbach Resonance	40
4.2	Our Early Attempts	42
4.3	Molecule Lifetime	48
4.4	Creating Molecules: New Techniques and Tools	54
4.5	Driving Bad Bound-Bound Transitions	56
4.6	Molecule Association Process	58
4.7	Ultracold, Trapped Molecules	62
4.8	Binding Energy of the Feshbach Molecules	64
4.9	Properties of the Feshbach Molecule	70
4.10	Conclusions	73
5	Inelastic decay of the molecules	76
5.1	Introduction	76
5.2	Collisional Stability of Fermionic Feshbach Molecules	77
5.3	Isolating Collision Partners	79

5.3.1	Distinguishable Atoms	79
5.3.2	Bosonic Atoms	80
5.3.3	Fermionic Atoms	81
5.4	Three-Body Recombination	82
5.5	Conclusions	82
6	Conclusions and future directions	88
6.1	Conclusion	88
6.2	Future Work	89
	Bibliography	95
	Appendix	
A	Magnetic Trap Trouble	102

Tables

Table

2.1	Major impurities of the enriched KCl. Source: Trace Sciences International.	19
5.1	Scattering length, a , dependence of the loss coefficient for various collision partners. 'BF' refers to the Feshbach molecule, 'B' to the boson, 'F' to the fermion, and 'X' to a distinguishable K atom. $P(a)$ and $M(a)$ are log periodic functions in a with modulations resulting from the formation of Efimov states.	78

Figures

Figure

- 2.1 General schematic for the laser system (same for Rb and K lasers). We use saturated absorption on atomic references to detect and stabilize the repump laser frequency. Using the frequency-stabilized repump light we “offset lock” the trap laser frequency by electronically detecting the beatnote between the trap and repump lasers and stabilizing the beatnote to an rf source. Light from both lasers are amplified for the MOTs. 11
- 2.2 Construction of the injection locked laser for amplifying K trap light. On the left, an exploded view of only the collimation tube holder and the cooling stages. On the right, the interior view of the IjLL. A laser diode designed for room-temperature operation at 780 nm was cooled to -45 degrees Celsius to shift the wavelength down to 767 nm. 13

2.3	Schematic of our vacuum chamber. From right to left: Atomic sources supply atoms to the MOTs and keep the MOT cell at higher pressures. We limit migration of contaminants from the MOT cell using the differential pumping tube. The bump region has a borosilicate glass slide to block atomic line-of-sight to the science region. A gate valve can be closed to separate the MOT region from the science region of the vacuum chamber.	15
2.4	A zoomed-in overhead view of the MOT region of the vacuum chamber.	17
2.5	A schematic of the coils of the Ioffe-Pritchard magnetic trap. The large circular pair of coils are the bias coils. The small circular pair of coils are the pinch coils. Finally, the elongated, “racetrack” pair of coils are the Ioffe coils. Electrically, the Ioffe and pinch coils are connected in series. The bias coils are connected in series with each other but are electrically separate from the other coils.	22
2.6	A computer generated model of the magnetic trap and its holder.	23

2.7	Contour plots of the magnitude of the magnetic field produced by a Ioffe-Pritchard Trap. The data is obtained from a computer model of the magnetic field using our coil geometry and dimensions. The horizontal direction of the plot is along the direction of the bias magnetic field. The vertical direction of the plot corresponds to the radial direction of the trap. The color scale is the same for each plot with purple corresponding to a low magnetic field and red corresponding to a high magnetic field. For each plot the current in the Ioffe coils and pinch coils are fixed and have the same value. The difference between the plots comes from increasing the current through the bias coils from low current (top) to high current (bottom). By increasing the bias current, the magnetic trap's depth increases and the radial trap frequencies increase.	24
2.8	Circuit diagram of the rf coil that is impedance matched to 50 Ω at DC-10MHz and near 80 MHz.	25
2.9	Imaging system used to detect the atoms and molecules.	27
3.1	Number of ^{87}Rb atoms recaptured into the MOT after loading a quadrupole magnetic trap. The atoms are held at the indicated gradients for 200 ms. The two data sets are before (Δ) and after (\bullet) optimizing the molasses stage before the quadrupole load. Optical pumping is not optimized.	32

- 3.2 Number transferred past the “bump” as a function of current in the bump coils. The optimized transfer efficiency across only the bump is about 97%. This efficiency is calculated by comparing the number transferred past the bump to the number transferred to just before the bump. It is important that the speed of the track is less than 20 cm/sec for the best transfer efficiency across the bump. The pyrex obstruction totally blocks the cloud’s path for currents below 4.5 amps and the vacuum chamber wall totally blocks the cloud’s path for currents above 8 amps. 34
- 3.3 Effect of forced evaporative and sympathetic cooling on the temperature and number of both atomic species. The clouds’ temperature decreases at the expense of ^{87}Rb atom number (solid circles). The ^{40}K atom number (solid triangles) is only slightly affected. 36
- 3.4 Breit-Rabi diagram for ^{87}Rb at low magnetic field. We evaporatively cool the ^{87}Rb gas by driving the $|2, 2\rangle \rightarrow |1, 1\rangle$ transition. This removes ^{87}Rb atoms from the magnetic trap. We also drive the $|2, 1\rangle \rightarrow |1, 0\rangle$ transition to remove impurity states of ^{87}Rb that inelastically collide with ^{40}K 38
- 4.1 Magnetic field can be used to tune a closed molecular state and the open atomic states into degeneracy. The different magnetic moments of the two states allow the tunability. If these states are coupled, a Feshbach resonance will occur at a magnetic field in the vicinity of the crossing between the two states. The grey arrow indicates how the molecule state can be populated with a slow magnetic-field sweep. 41

- 4.2 Loss of K atoms in the presence of Rb resulting from an interspecies s-wave Feshbach resonance. The atoms are in the $|9/2, -9, 2\rangle_K$ and $|1, 1\rangle_{Rb}$ states and are held at the indicated field for one second before abruptly turning off the magnetic field and imaging them. For this measurement the number of ^{40}K atoms was about 10^5 and the number of ^{87}Rb atoms was about $5 \cdot 10^5$. Both clouds were initially in thermal equilibrium at a temperature of about 500 nK. 44
- 4.3 Loss of K atoms, in the presence of Rb, resulting from an interspecies p-wave Feshbach resonance. The atoms are in the $|9/2, -9, 2\rangle_K$ and $|1, 1\rangle_{Rb}$ states and are held at the indicated field for one second before abruptly turning off the magnetic field and imaging them. For this measurement the number of ^{40}K atoms was about 10^5 and the number of ^{87}Rb atoms was about $5 \cdot 10^5$. Both clouds were initially in thermal equilibrium at a temperature of about 500 nK. 45
- 4.4 Solid lines show the time dependent ramps near the Feshbach resonance. The top figure shows a ramp that should not create molecules. The lower figure shows a ramp direction that should create molecules. 46
- 4.5 The peak optical depth of K after ramping across the Feshbach resonance. The time to complete the ramps of Fig. 4.4 was adjusted. The atomic loss is consistent with molecule formation after ramping slowly from high to low magnetic field (solid circles). The time spent near the resonance is not a significant factor for atomic loss since little loss is observed after ramping slowly from low to high magnetic field (solid triangles). The dashed line indicates the initial optical depth of the K cloud without ramping across the resonance. The optical depth was measured after 12ms of free expansion. . . 47

- 4.6 Solid line shows a typical time-dependent magnetic-field ramp near the Feshbach resonance. The hold magnetic field was changed for each data point of Fig 4.7. The ramps up to and away from the hold field were adiabatic for creating molecules. 49
- 4.7 Finding the resonance location using time-dependent magnetic-field ramps. The transition to more loss occurs when the hold field of Fig. 4.6 is above the resonance position. This loss is due to the creation of molecules which, in this experiment, were quickly removed by the optical trap light. The magnetic field was held for $300 \mu\text{s}$ and the ramps toward and away from the resonance had inverse ramp rates of 0.139 ms/gauss . The solid line is a fit, using an offset error function, to the data. B_0 is taken as the center of the fitted error function. The 10% to 90% width of the error function is taken as the uncertainty in B_0 . Using these criteria, we obtain $B_0 = 546.47 \pm 0.12 \text{ gauss}$. The initial ^{40}K and ^{87}Rb atom numbers were about $1.1 \cdot 10^5$ and $2.9 \cdot 10^5$ and $T = 240 \text{ nK} = 0.8T_c = 0.6T_F$. We detected the atoms at low magnetic field after turning off not only the optical trap but also the magnetic fields. 50
- 4.8 Magnetic-field ramp near the Feshbach resonance to create molecules, probe their lifetime, and reconvert the molecules to atoms for low magnetic-field imaging. The vertical jumps represent diabatic crossings of the resonance. The ramps are adiabatic for creating and dissociating molecules. 52

4.9 A measurement of the lifetime of molecules. We used magnetic-field ramps similar to Fig. 4.8 to reconvert the molecules into atoms. The hold magnetic field for this measurement was 546.2 ± 0.2 gauss. The solid line is the results of an exponential fit to the data. The fitted decay time is $220 \pm 7 \mu\text{s}$ 53

4.10 Rf association spectrum of heteronuclear Feshbach molecules at $B = 546.04$ G. The molecules are created starting from an ultra-cold gas of 1.7×10^5 ^{87}Rb atoms at $T/T_c = 1$ in thermal equilibrium with 8×10^4 ^{40}K atoms. The plot shows the detected atom/molecule number as a function of the detuning $\Delta\nu$ of the rf from the atomic resonance frequency. We observe a large atomic peak at zero detuning and a molecular peak at $E/h = 161$ kHz due to the association of atom pairs into the Feshbach molecule state. In this measurement the rf pulse duration was $600 \mu\text{s}$, which is 50 times longer than an atomic π -pulse. The grey band indicates the expected envelope full width at half maximum for the power broadened atomic transition. The inset shows a simplified energy diagram for magnetic fields below the Feshbach resonance. The upper solid line corresponds to Rb $|1, 1\rangle$ and K $|9/2, -7/2\rangle$, while the lower solid line corresponds to Rb $|1, 1\rangle$ and K $|9/2, -9/2\rangle$. The molecule state is represented by the dashed line. Depending on the detuning, the rf is capable of driving an atomic hyperfine changing transition or magnetoassociation. This data was taken while the atoms and molecules were held in an optical trap derived from a 1064 nm single-frequency fiber laser. 57

- 4.11 KRb molecular potentials. Svetlana Kotochigova has calculated that the 1075nm optical trap laser predominately drives bound-bound transitions from the Feshbach molecule state to vibrational states of either the 3(1) or 2(1) molecular potentials. The molecule potential energy data for this figure was obtained from Ref. [1]. 59
- 4.12 Time dependence of the rf association process at $B = 546.17 \text{ G}$, where the measured molecule binding energy is $E/h = 96 \text{ kHz}$. The plot shows the measured number of molecules created as a function of the $1/e^2$ gaussian rf pulse length. The solid line is a simple fit used to estimate the impact of the observed decay on the maximum number of molecules created. 61
- 4.13 Temperature dependence of Feshbach molecule creation by rf association. Plotted is the molecule conversion fraction N_m/N_K as a function of T/T_c for the Rb atoms. The solid circles (\bullet) are experimental data and the curves are results of a Monte Carlo calculation. The dashed curves represent the uncertainty in the conversion fraction taking into account the uncertainty in the trap frequencies and atom numbers. The molecules are created starting from an atom gas mixture with $N_{\text{Rb}} = 3 \times 10^5$ and $N_K = 1 \times 10^5$. We observe maximum conversion efficiency of 25% at $T/T_c = 1$ 63

- 4.14 (Top inset) Images of the molecule cloud after release from the optical trap. (Top) Radial cloud size for the molecules after release from the optical trap. (Bottom) Sloss of the molecular cloud in the optical trap seen in images of the expanded gas. The expansion time was 3 ms. The observed oscillation in the molecule cloud's position demonstrates that the molecules are indeed trapped. The strong damping seen here is most likely due to anharmonicity of the optical trap. 65
- 4.15 Energy of the heteronuclear Feshbach molecules, relative to the Rb $|1, 1\rangle + \text{K } |9/2, -9/2\rangle$ atomic threshold, plotted as a function of magnetic field. The data (solid circles) agree well with our calculation based on a full coupled-channel theory (solid line). Near the Feshbach resonance one expects a universal relationship between the s-wave scattering length and the binding energy. The black, dashed line shows the predicted binding energy using the universal prediction [2]. Inset: Same as the main plot but looking at the region close to the Feshbach resonance. 68
- 4.16 Calculated molecule energies near the K $|9/2, -9/2\rangle + \text{Rb } |1, 1\rangle$ atomic threshold. All levels have total spin projection quantum number $M_F = -7/2$. The level energies are calculated using a full coupled-channel calculation and have been scaled so that the zero in energy is the K $|9/2, -9/2\rangle + \text{Rb } |1, 1\rangle$ atomic threshold. The bold line is the adiabatic level associated with the 546.7 G Feshbach resonance. 69

4.17	Estimated molecule size vs. magnetic field near the Feshbach resonance as extracted from the experimentally measured binding energy (\bullet). We compare to the universal size prediction, $a/2$ (dashed line). Inset: Closed channel fraction extracted from the experimentally measured binding energy (\bullet)(see Sec. 4.9).	71
4.18	The calculated open-channel molecular size, r_o , as a function of binding energy. The solid red line is the universal prediction, $a/2$. The dashed blue line is the classical outer turning point of the KRb ground state potential.	74
5.1	Molecule loss coefficient β for collisions with distinguishable atoms (K in the $ 9/2, -7/2\rangle$ state) as a function of the heteronuclear scattering length. For large a , we observe β to decrease with increasing scattering length in agreement with numerical calculations (solid red curve). We observe β saturating for small a , ($a \sim 100 a_0$) where the molecular size, $\langle r_{mol} \rangle$, no longer has a strong dependence on a . Inset: β vs. molecule size $\langle r_{mol} \rangle$ as extracted from the measured binding energy of the Feshbach molecules [3]. The green dashed curve is a power law fit $\beta_{fit} \propto \langle r_{mol} \rangle^p$ to the experimental data; we obtain $p = -0.97 \pm 0.16$	84
5.2	Molecule loss coefficient for collisions with indistinguishable bosons versus heteronuclear scattering length. For large a , β increases with increasing a . In this regime the molecular loss is enhanced compared to loss due to molecule collisions with distinguishable atoms (green dashed curve and Fig. 1). For small a , β increases with decreasing scattering length (see Section 5.3.2).	85

- 5.3 Molecule loss coefficient β for collisions with indistinguishable fermions. For large a we observe loss rates scaling as $a^{-1.6\pm 0.2}$. The power law dependence is consistent with numerical calculations for this scattering length regime (solid red curve). In addition, the molecular loss is suppressed compared to inelastic decay of molecules due to collisions with distinguishable atoms (green dashed curve and Fig. 1). Inset: Molecule decay at $a \approx 1300 a_0$. The $1/e$ -lifetime of the molecular cloud is $\tau = 100 \pm 20$ ms 86
- 5.4 Three-body recombination near the heteronuclear Feshbach resonance. The measured K_3 varies as a^4 and saturates at large a due to the unitary limit. The dashed curve is an a^4 fit to the data for $|a| < 4000 a_0$. The solid line is the unitarity limit at 150 nK. . . . 87
- 6.1 Diagram showing the laser frequency we initially used to find excited molecular states. The laser was tuned energies lower than the D1 line of atomic Rb. This corresponds to wavelengths longer than 795 nm. 91
- 6.2 Observed molecule loss due to excitation to excited electronic states of the KRb molecule. Here we start with Feshbach molecules and illuminate them with laser light having the indicated frequency. The Feshbach molecules are lost when the laser light excites them to states where they spontaneously decay and are lost from the trap. 92

6.3 Loss of molecules in the Feshbach state resulting from optical excitation to an excited, bound molecular state of KRb. All experimental parameters were the same as in Fig. 6.4 except here, the initial state is the Feshbach molecular state instead of freely colliding atom pairs. Here, τ is shorter by a factor of 500 compared to freely colliding atom pairs. 93

6.4 Loss of atoms resulting from photoassociation into an excited, bound molecular state of KRb. The τ for this data is about a factor of 500 longer than the data shown in Fig. 6.3. 94

A.1 The resistance of the coil plotted against the temperature of the water flowing through the coil. The slope of the curves is consistent with the thermal coefficient of resistance of copper. The vertical resistance shifts are caused by mechanical perturbations of the coil. These shifts are relatively small at about 1% of the total resistance of the coil. For comparison, if a complete winding were shorted, it would have a shift 13 times larger. 104

A.2 Correlation between the cloud’s measured position and percent resistance change. The data was taken after releasing from the magnetic trap for 15ms of free expansion. The slope is roughly consistent with the slope predicted by a numerical calculation. 106

A.3 A view of the Ioffe coil’s problematic lead. The pressure between the wires at this transition point caused an incomplete short to other windings through the polyimide coating. 107

Chapter 1

Introduction

1.1 KRb Molecules

This thesis discusses some of the first experiments to make ultracold heteronuclear molecules. The motivation behind this work is to efficiently create KRb molecules as a first step toward achieving a long-term goal of producing a relatively dense gas of ultracold polar molecules. To accomplish this, we implemented well-established capturing, cooling and associating techniques used in other ultracold alkali atom experiments. In addition, we developed new techniques that are specific to the mixture of atoms we use: fermionic ^{40}K and bosonic ^{87}Rb . This thesis will present our experimental techniques with an emphasis on the new techniques with the hope that this will prove useful to people either using the existing apparatus or planning on building similar experiments. In addition to experimental techniques, this thesis will describe how loosely-bound KRb molecules were associated and characterized. It will also present a study of inelastic atom-molecule collisions near a Feshbach resonance through measurements of the molecules' lifetime. The atom-molecule collisions are interesting because the atoms involved can be either distinguishable or indistinguishable from the molecule's constituent atoms. This means we were able to test how inelastic rates of the molecules scaled when either fermions, bosons, or distinguishable atoms were allowed to collide with the molecule.

1.2 Why Ultracold Molecules?

The major attractive feature of molecules, compared to atoms, is their rich internal degrees of freedom. Experiments with ultracold molecules can explore the vibrational and rotational structure of the molecule with much better precision than previously attained with higher temperature gases. For example, improvements in precision can be used to test fundamental physics [4, 5, 6]. Additionally, the molecule can offer unique properties to the experimenter that atoms, alone, cannot provide. For example, many molecules are easily affected by external electric fields. Compared to atoms, it is easier to affect the internal energy of the molecule using external electric fields if the molecule possesses a spatial asymmetry. In the simplest case, a molecule composed of two unlike atoms can be manipulated by an external electric field because the two atoms share the electrons in a lopsided way which induces a permanent electric dipole moment.

A perfectly symmetric molecule, like the homonuclear H_2 , will not possess a dipole moment. However, virtually any molecule with an asymmetry will possess a dipole moment of some degree. Remarkably, this even applies to HD, a nearly homonuclear molecule [7, 8]. Although the HD dipole moment is incredibly weak, it played a role in cooling gas clouds in the early universe [9]. The dipole moments of HD and LiH allowed these early gas clouds to radiatively cool and, therefore, collapse into early stars. It is important to note that I am cavalier with the phrase “dipole moment”. My “polar” molecules do not possess a true permanent dipole moment. Instead, they are easily polarized in relatively weak electric fields making it appear as if they possessed a permanent dipole moment. There is currently no direct experimental evidence showing that atoms or molecule possess a true permanent dipole moment but this may change in the near future.

We decided to attempt making ultracold polar molecules because the dipole

moment offered some exciting prospects for future studies at such low temperatures. In particular, because many heteronuclear diatomic molecules have relatively large dipole moments $\gtrsim 1$ Debye, it seemed like it should be easy to partially polarize the molecules in an external electric field, observe long-range dipole-dipole interactions between the molecules, or use the molecules as quantum bits for quantum information processing schemes [10].

1.3 Making Ultracold Molecules

There are several strategies one could pursue to create ultracold molecules. Starting with room temperature molecules one could obtain cold molecules using Stark deceleration [11, 12], buffer gas cooling [13], or velocity selection [14]. The challenge for these methods is obtaining large densities of cold molecules. Another method is to start with an ultracold, dense atomic cloud and produce molecules through association techniques. This method is hindered by the availability of atoms that can be easily cooled. The alkali atoms enjoyed early laser cooling success because of their nearly closed “cycling” transition. Additionally, alkali atoms had been associated into molecules using optical techniques [15, 16, 17]. It was because of these advances and our ability to cool the alkalis that we decided to use ultracold alkali atoms as our starting point for ultracold molecules.

We began constructing the apparatus in the summer of 2003 in an empty lab shared with another molecule experiment. Our plan was to create an apparatus in which a mixture of atoms would be used to form molecules. For collecting and cooling the gases and enhancing molecule production, the experience of Carl Wieman’s and Deborah Jin’s groups would be important. Once the molecules were produced, we would then take advantage of Jun Ye’s laser experience to produce tightly bound molecules having an electric dipole moment.

In 2003, the techniques for trapping and cooling alkali atoms were well estab-

lished. In addition, at about the same time, experimenters had taken advantage of Feshbach resonances to efficiently create loosely bound molecules. These resonances were magnetic-field tunable. So, by ramping the magnetic field near a Feshbach resonance, one could efficiently convert atoms into molecules [18, 19]. These “Feshbach molecules” were well suited for further manipulation steps because their lifetimes could be relatively long and because their size was tunable near the Feshbach resonance. The tunable size could allow for improved Franck-Condon overlap with molecular vibrational states in the excited electronic potential.

1.4 History of Ultracold Mixtures of Alkali Atoms

A major limitation for precision studies using atoms and molecules has historically been that they move at high speeds because of their thermal energy. Such speeds induce uncertainties caused by Doppler broadening and short interaction times. It has, therefore, been a goal of researchers to slow the motion of the atoms and molecules relative to the lab so these limitations are removed [20]. After slowing their motion, collisional interactions can become important and can then be studied and controlled.

The major successes of controlling and cooling atoms’ motion came throughout the 1980’s with the advent of laser cooling. Based on suggestions of Hänsch, Schawlow, Wineland, Dehmelt, and Ashkin, and success of laser cooling ions, it became clear that cooling neutral atoms could be possible. In fact, cooling neutrals to and then trapping them at microKelvin temperatures was possible. These techniques typically slow atoms from speeds of hundreds of miles-per-hour to around one-tenth of a mile-per-hour. The work of cooling and understanding the cooling mechanisms of neutral atomic gases was awarded a Nobel Prize in 1997 and is summarized nicely in the corresponding Nobel lectures [21, 22, 23]

and references therein.

The success of laser cooling culminated in the experimental realization of Bose-Einstein Condensation (BEC) in a dilute, weakly interacting atom gas in 1995. This result was, in itself, a major achievement, which overcame many technical obstacles, and was also awarded a Nobel prize in 2001. Again, the Nobel lectures [24, 25] and references therein are good sources for a summary of the work and more historical details.

Following the creation of BEC, fermionic atoms were put into the cool glare of laser and evaporative cooling. These techniques were equally successful and resulted in fermionic atoms entering the quantum degenerate regime by the late 1990s [26, 27]. The resulting degenerate Fermi gas (DFG) was a clean, defect-free system having well known two-body interactions. A serious goal at that time was to make a low-temperature two-component strongly-interacting Fermi gas and explore the BCS-BEC crossover regime [28, 29, 30, 31, 32, 33]. The experimental realization of this goal in 2004 was aided by using a special tool, called a Fano-Feshbach resonance[19], to control the interatomic interactions between two different spin states of the fermions [34, 35]. Such control over the atoms has given researchers a better understanding of the BCS-BEC crossover.

Although BECs, DFGs, and BCS-BEC physics are not directly related to the experiments described in this dissertation, we utilize similar supporting techniques to create heteronuclear molecules. This is accomplished by capturing and cooling two types of atoms: bosons and fermions. The resulting mixture of atoms are coaxed into forming fermionic diatomic molecules using a Feshbach resonance.

1.5 Thesis Outline

Chapter 2 will give details of the $^{40}\text{K} + ^{87}\text{Rb}$ apparatus. It will describe what the apparatus was supposed to accomplish for our science goals. It will also include

a brief compilation of atomic parameters, a motivation for and layout of our optical system, a description of the vacuum chamber and how we create ultracold samples of K and Rb. Chapter 4 will describe how we created heteronuclear molecules using Feshbach resonances. Chapter 5 will describe experiments that explored inelastic collisions between various atomic species and the loosely bound molecules. Most of Chapter 5 has been derived from a published article [36]. Finally, Chapter 6 will summarize the thesis and give a look toward future experiments.

Chapter 2

Apparatus

2.1 Introduction and Overview

The apparatus is the machinery responsible for capturing, cooling, controlling, and detecting the atoms and molecules that are used in the experiments described in subsequent chapters. It incorporates a diverse set of tools including computers and software, optics, lasers, digital and analog circuits, a mechanical motion stage and an ultra-high-vacuum chamber. Most of these tools had been perfected and incorporated in other laboratories in JILA and elsewhere. It was our goal to reproduce the good from other labs while avoiding the bad. I've found that the best way to reproduce results is to copy the methods. I will try to point the reader in the direction of the references of the methods when I can. This chapter is devoted to giving the reader technical details and a basic flavor of how and why we chose certain elements of the apparatus. I will attempt to point out whether these choices are either physically justified or aesthetically preferred. I hope this will not only help the future users of the apparatus but will also help guide others interested in building similar apparatuses.

Inside of an ultra-high vacuum (UHV) chamber, we use standard techniques of laser cooling and trapping combined with evaporative cooling to obtain mixtures of ultracold ^{40}K and ^{87}Rb atoms suitable for Feshbach molecule formation. I will discuss these techniques in greater detail in a subsequent chapter. Briefly, these

techniques start by using a magneto-optical trap (MOT) to capture and cool atoms from a room-temperature gas. The MOT is located in a section of the vacuum chamber having relatively large partial pressures of K and Rb. Typically we selectively capture about 10^7 ^{40}K and 10^9 ^{87}Rb atoms in the MOT. These trapped clouds have temperatures of a few hundred micro-Kelvin. Once the MOTs are fully loaded, we compress the MOT and transiently cool the atoms using polarization gradient cooling. After this preparation, the atoms are optically pumped into the magnetically trappable stretched states and are ready to be transferred into a quadrupole magnetic trap. After all laser fields are turned off, the quadrupole trap is suddenly turned on and captures K and Rb atoms. Using a mechanical motion stage, the quadrupole trap is then physically moved from the high pressure region of the vacuum chamber to a lower pressure region called the Science cell. Here, the atoms are transferred into a standard Ioffe-Pritchard (IP) magnetic trap. In the magnetic trap we use microwave fields to force evaporative cooling of the ^{87}Rb atom gas, which sympathetically cools the ^{40}K gas. Once the temperature is about $1\ \mu\text{K}$ we load the atoms into a far off-resonant optical dipole trap. This trap can hold atoms in any of the possible hyperfine states rather than just the low-field seeking states that are trapped by the magnetic trap. We use rf and microwave fields to transfer the ^{40}K and ^{87}Rb atoms into their energetically lowest hyperfine states and then increase the local magnetic field to approximately 500 gauss. Here, we continue to evaporative cool the clouds of atoms inside the optical trap until the gas reaches quantum degeneracy.

Since the apparatus is a marriage of two sub-apparatuses, one for ^{40}K and one for ^{87}Rb , the overall complexity of the apparatus increases by at least a factor of two when compared to a single-species apparatus. The apparatus' overall reliability decreases with the addition of more lasers, electronics, and equipment to deal with the ^{40}K atoms, ^{87}Rb atoms, and molecules. Because of this, the intrinsic

reliability of each component needs to be as high as possible for as long as possible for the sanity of the graduate students and advisors. It is, therefore, unacceptable to build important components of the apparatus too hastily because any time that was saved will be eventually consumed (and then some) while debugging problems later. As a simple example, assume I have an external cavity diode laser (ECDL) whose frequency stabilizing servo stays locked for an average time of one hour. If I rely on six similar ECDLs in the apparatus, the average time between failures would be 10 minutes. This failure rate is unacceptable when collecting data at a rate of a single point every 2 minutes!

2.2 Laser Systems for the Atoms

To accomplish the cooling and, later, detection of the ultracold gas, we require light that is very nearly single frequency when compared to the natural frequency width of the atoms' electronic transition. For the case of K and Rb, the natural widths are approximately 6 MHz. Diode lasers stabilized by an external cavity are able to easily achieve linewidths down to about 100 kHz and they are smaller and less expensive than other solid-state lasers. Fortunately, because of the Compact Disc writer market, laser diodes (LD) with ample power at the Rb transition wavelength of 780 nm have been readily available. However, these lasers are becoming more obsolete with the current market shift towards higher density discs and downloadable media.

Each atom species requires a laser system for cooling, optical pumping, and detecting the atoms. An overly simple schematic is shown in Fig. 2.1. Each system is composed of two major lasers, which we call repump and trap lasers for their roles in the MOT. The repump laser's frequency is referenced to an atomic source using saturated absorption spectroscopy. The trap laser's frequency needs to be changed during an experimental cycle, for example, from the frequency

that is needed for loading the MOT to the frequency for imaging the atomic cloud. It is because of these frequency changes that we use a fast photodiode and a phase/frequency detector to “offset” lock the trap laser to the repump laser. More details related to this technique can be found in Scott Papp’s thesis [37]. The major advantage of this technique is the ease of changing the laser frequency using a computer controlled voltage. We use a voltage controlled oscillator (VCO) to provide the local frequency reference for the difference frequency between the repump and trap lasers. The VCO’s frequency is easily controlled with an external voltage from the control computer.

We amplify the trap lasers using injection locked lasers (IjLLs)[38, 39, 40]. By coupling trap light into the rejection port of an optical isolator, we inject a small amount (≈ 1 mW) of trap laser power into the IjLL. The injected beam into the IjLL is aligned by measuring the output power of the IjLL after the output port of the optical isolator. The threshold current of the IjLL shifts to lower current with proper alignment of the injecting beam. Using the IjLL reduces the operating current of the trap lasers and gives plenty of laser power for detection of the atoms. For both IjLLs, we use a 780 nm diode laser (Sharp model GH0781JA2C). It is important that the non-injected, free-running wavelength of the IjLL is close to the required operating wavelength. The IjLL’s free-running wavelength can be tuned by adjusting the IjLL diode’s temperature. We use a diode that is approximately at Rb’s D2 wavelength at room temperature and we cool the Rb IjLL only to 10 degrees Celsius and stabilize this temperature to about 0.001 degrees Celsius. To reach the K wavelength at 767nm, the K IjLL is cooled to -45 degrees Celsius with a stability of 0.001 degrees Celsius. Because this temperature is well below the dew point, it is important that the K IjLL is properly sealed from the atmosphere to prevent moisture from depositing on the cold laser holder. We used Torr Seal $\text{\textcircled{R}}$ to seal the electrical leads and rubber gaskets to seal the lid and base of the

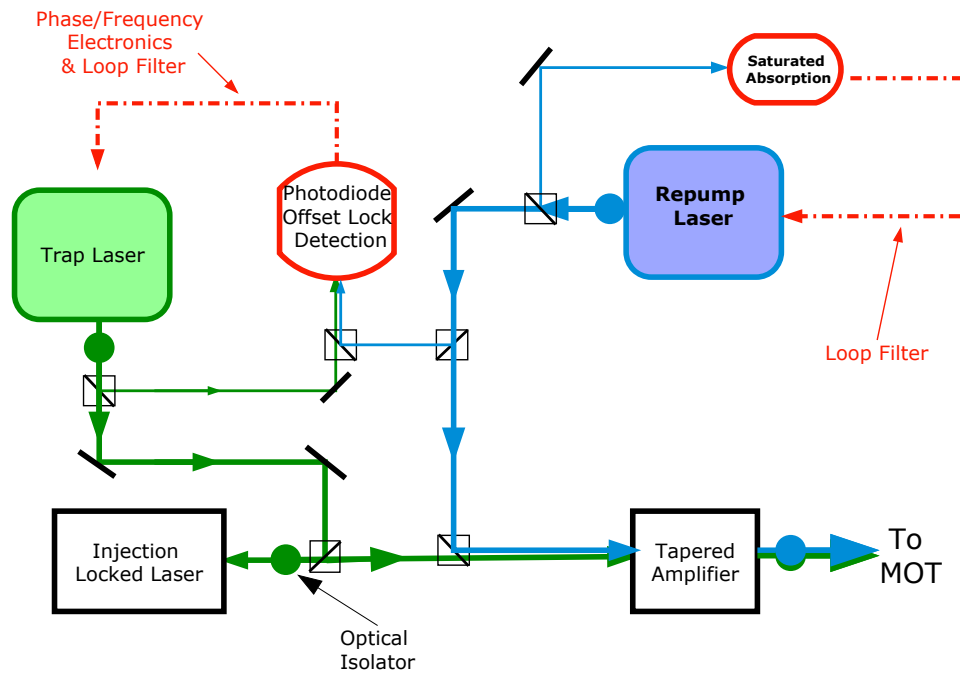


Figure 2.1: General schematic for the laser system (same for Rb and K lasers). We use saturated absorption on atomic references to detect and stabilize the repump laser frequency. Using the frequency-stabilized repump light we “offset lock” the trap laser frequency by electronically detecting the beatnote between the trap and repump lasers and stabilizing the beatnote to an rf source. Light from both lasers are amplified for the MOTs.

IjLL box. We also insulate the holder to reduce blackbody and convective heat transfer. Figure 2.2 shows a diagram of the K IjLL. A hole is cut into the bottom of the aluminum box to allow direct contact between the Peltier cooler and chilled water plate. Having this direct contact was critical to obtain sufficiently low temperatures.

For both laser systems we combine light from the IjLL and the repump into a Tapered Amplifier (TA). The TA provides 300 mW of optical power. Here we use Eagleyard TAs controlled by Thorlabs current controllers (Model LDC 340). Both repump and trap light are amplified by the TA and sent to polarization maintaining (PM) fibers for spatial filtering and delivery to the MOTs at the vacuum chamber. After the fiber, there is 150mW of total power for the MOTs.

2.2.1 The MOTs

The MOT beams are formed after the polarization maintaining fibers by combining the K and Rb light and enlarging the beams. The K and Rb light are combined on a polarizing beam splitting (PBS) cube. After the cube, the polarizations of K and Rb are perpendicular to each other but they need to be parallel for the MOT. So, we use a high-order waveplate (29.5λ) to rotate the K light's polarization to be parallel to the Rb light's polarization. Subsequent polarization manipulations for the MOT are carried out by large diameter $\frac{1}{2}$ and $\frac{1}{4}$ wave plates that affect both wavelengths almost equally. A telescope composed of three lenses is used to enlarge the MOT beams so they have a diameter of 3 centimeters.

2.3 Vacuum Chamber

We use a ultra-high vacuum (UHV) chamber to isolate the ultracold atoms from the room temperature atmosphere. A simplified schematic of the vacuum

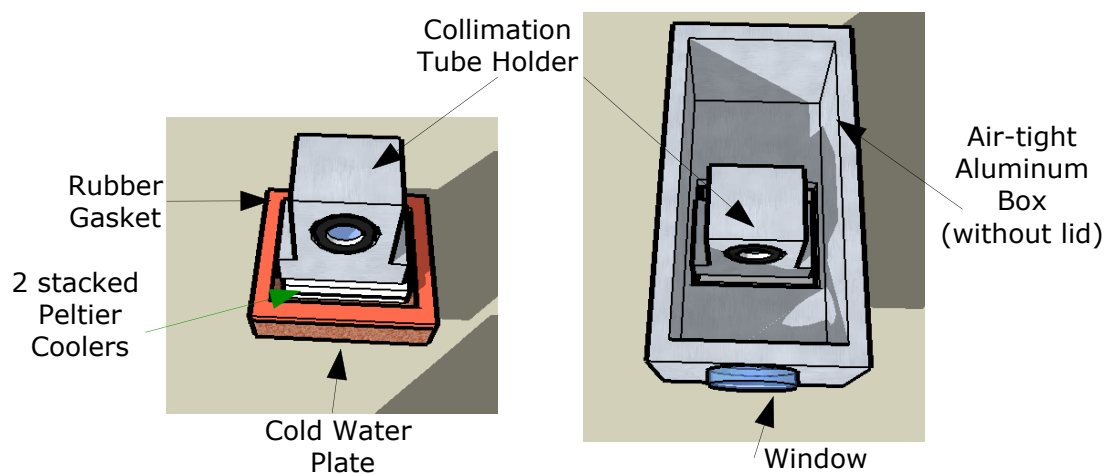


Figure 2.2: Construction of the injection locked laser for amplifying K trap light. On the left, an exploded view of only the collimation tube holder and the cooling stages. On the right, the interior view of the IjLL. A laser diode designed for room-temperature operation at 780 nm was cooled to -45 degrees Celsius to shift the wavelength down to 767 nm.

chamber is shown in Fig. 2.3. This chamber contains our atomic sources of Rb and K in a higher pressure region designed for the initial capture and cooling of the atomic gases. This initial section of the vacuum chamber is called the “MOT cell”. A series of tubes connects the MOT cell to a lower pressure region, called the “Science cell”. These transfer tubes limit the conductance of gas from the MOT cell to the Science cell.

Although Rb and K are dominant in the MOT region, other contaminants can pollute the rest of the ultra-high vacuum chamber. These other contaminants will limit our ultracold gas lifetimes and number of atoms after evaporation. Therefore, it was important to condition the stainless steel components before assembling the vacuum chamber. We started by cleaning the components using detergents, deionized water and alcohols to remove any machine oil or finger prints. Once we had chemically cleaned the parts we treated the stainless steel components to minimize Hydrogen outgassing. Typically this can be done by baking them either in vacuum or in air. We did an air bake at 400 degrees Celsius for one day. Presumably, baking in air causes an oxide layer to form on the stainless steel and limits the migration of hydrogen off of the walls of the chamber [41, 42].

After assembly and initial pump-down, we baked the chamber at 250 degrees Celsius for a week. This helped to further purge the chamber of water and adsorbed gases. Since alkali atoms attack glass at high temperatures, we were careful to keep the alkali sources from exceeding 250 degrees Celsius during the bake. In spite of this, we noticed a yellow/brown discoloration of the glass in the ampoules of rubidium and potassium.

2.3.1 MOT Region

The MOT cell, shown in Fig. 2.4, is evacuated down to UHV pressures. Atomic sources create a low-pressure vapor of Rb and K inside the cell. From

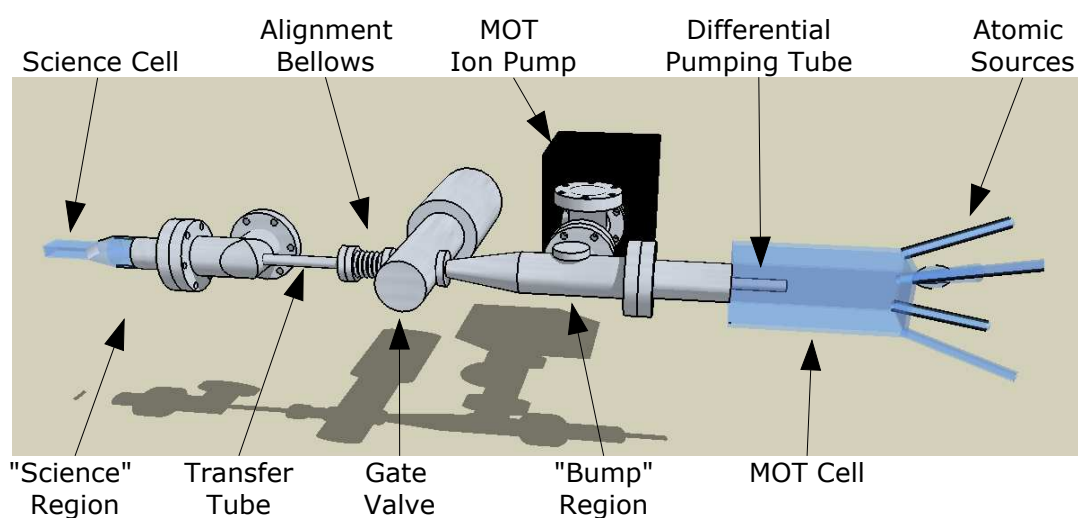


Figure 2.3: Schematic of our vacuum chamber. From right to left: Atomic sources supply atoms to the MOTs and keep the MOT cell at higher pressures. We limit migration of contaminants from the MOT cell using the differential pumping tube. The bump region has a borosilicate glass slide to block atomic line-of-sight to the science region. A gate valve can be closed to separate the MOT region from the science region of the vacuum chamber.

these nearly room-temperature gases, ultracold clouds are captured and cooled to only a few hundred microKelvin. Because the MOTs require optical access, the cell is made of borosilicate glass so it is transparent to the laser light for Rb and K. Electromagnetic coils are positioned near the MOT cell to provide the required magnetic fields for the MOTs and a quadrupole magnetic trap. Surrounding the cell, an aluminium oven, heated by resistive heaters, keeps the borosilicate walls at about 60° Celsius. This temperature helps keep the K atoms from sticking to the walls of the cell.

The MOT cell is connected to the rest of the vacuum chamber through a long narrow tube. Because of its size, the tube limits migration of atoms from the MOT cell to the rest of the chamber. This tube has a conductance of about 1 liter of air per second. At the end furthest from the MOT, the tube opens into the bump region. Here, a borosilicate glass obstruction is positioned perpendicular to the differential pumping tube. This obstruction was intended to prevent line-of-sight atoms from readily entering the science region. The bump region is pumped by a 20 liter per second ion pump (Gamma Vacuum TiTan 20S). The tube connecting the bump region to the ion pump has a conductance of about 38 liters per second. This conductance creates an effective pumping speed in the bump region of about 13 liters per second and about 0.9 liters per second in the MOT cell. This design ensures the pump always has a pressure that is at least 20 times lower than the MOT cell and helps prevent alkali buildup on the high voltage cells inside the ion pump. Assuming the MOT cell is the only source of contamination for the entire chamber, the total pressure differential from the MOT cell to the science cell should be about a factor of 180 if nitrogen were the major contaminant. Magnetic trap lifetimes in both regions indicate the differential is about 80. Hydrogen probably contributes most to the discrepancy between the calculated and measured conductances since it is desorbed from the stainless

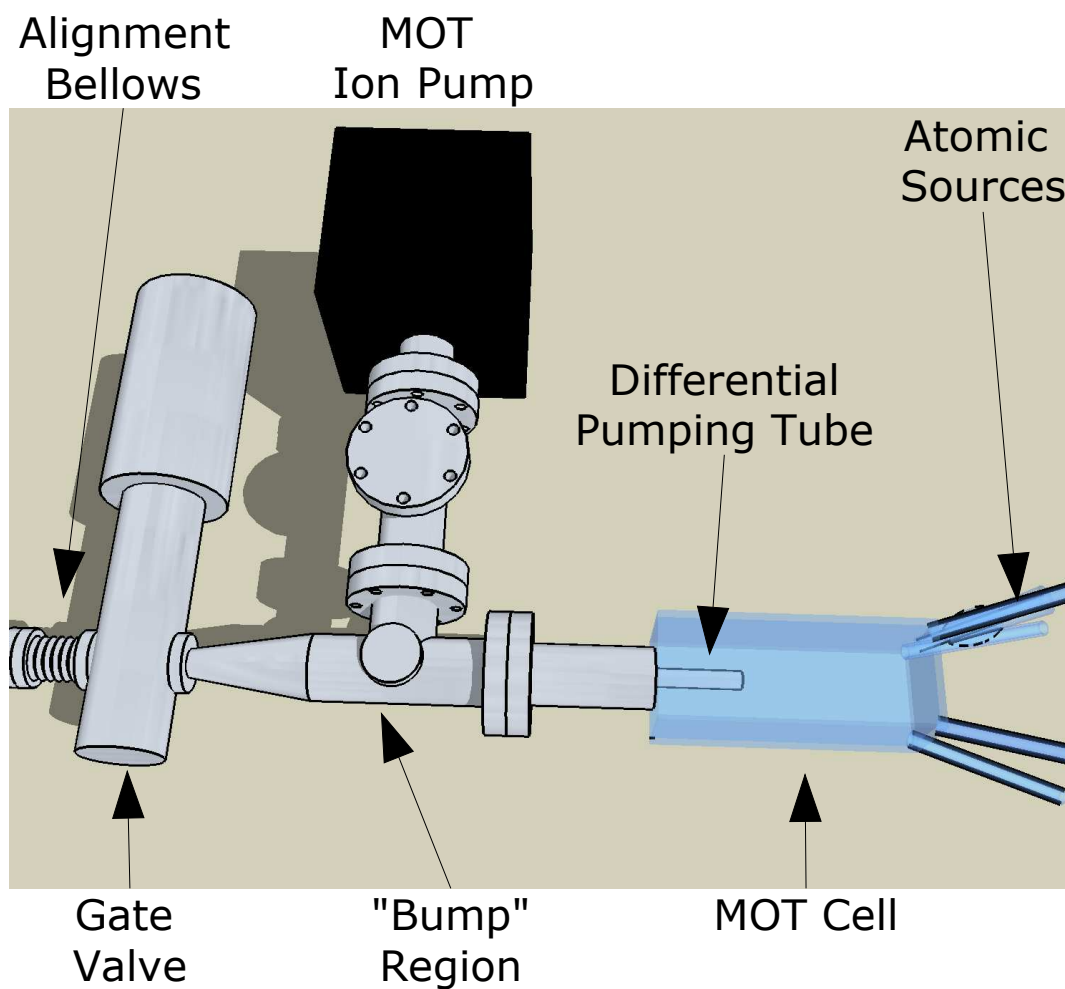


Figure 2.4: A zoomed-in overhead view of the MOT region of the vacuum chamber.

steel walls of the vacuum chamber and it is not pumped efficiently by the ion pumps.

2.3.1.1 Atom Sources

For our chamber, we use two different types of atomic sources. For Rb, we use pure Rb contained inside of a glass ampoule. The Rb was purchased from Alfa Aesar, who claims the purity of Rb is 99.75%. There are two ampoules, each containing 1 gram of Rb attached to the MOT cell. One of the ampoules was broken in-situ to expose the Rb metal to the interior of the MOT cell. Since there is no valve separating the ampoule from the MOT cell, the ampoule was broken after the initial bake of the MOT cell. If future bake-outs of the MOT cell are required, it will be necessary to remove the opened ampoule of Rb otherwise Rb will be evaporated from the ampoule and deposited throughout the vacuum chamber. The ampoule was chosen because of its high purity and simplicity. There are no electrical feed-throughs or extra materials to contaminate the vacuum. However, we are unable to easily control the amount of Rb in the chamber. The flux of Rb into the MOT cell is controlled by the conductance of the ampoule arm and Rb's saturated vapor pressure at room temperature.

There are also two ampoules containing enriched K attached to the MOT cell. However, at best, only one milligram of K is contained in each ampoule. During the bake of the MOT cell, the K appears to have reacted with the borosilicate glass, which caused a yellow/brown discoloration inside the ampoule. The reaction appears to have depleted the metallic K so we chose not to open the K ampoules to the MOT cell. As a backup to the ampoules, we installed four homemade enriched K dispensers. Each dispenser is made by combining 12 mg of KCl salt, that has been enriched in ^{40}K , with shavings of calcium inside a Nichrome "boat" [43]. The molar ratio of K to Ca is approximately 1:5. The KCl

Element	ppm	Element	ppm
Cu	9	Fe	<50
Cr	<10	Ca	<200
Na	15	Rb	200
Zn	18	Mg	280
Sr	25	Ba	1100
		Total	<1907

Table 2.1: Major impurities of the enriched KCl. Source: Trace Sciences International.

was purchased from Trace Sciences International. We purchased the KCl in 2003 and the enrichment was 5.2% in ^{40}K . Today, according to Trace Sciences' website, enrichments exceeding 13% in ^{40}K are available.

For improved MOT conditions and reduced background gases, it is important that impurities in the sources are minimized. The metallic calcium used in the dispenser is 99.98% pure according to Alfa Aesar. The KCl contains impurities of other elements. Trace Sciences provided the impurity fractions and compositions, which are reproduced in Table 2.1. Rb is listed as an impurity at the 200 parts per million level. We empirically discovered this fact when we set up and captured Rb in our MOT **before** breaking the Rb ampoule!

2.3.2 Transfer Tube

Separating the MOT chamber and the science chamber is an in-line gate valve (VAT Inc. Part number: 48124-CE01). The valve was included so changing either side of the chamber would be easier. It has a conductance of 10 liters per second. A bellows nipple is attached to the gate valve on the science cell side. These bellows allow for easier alignment of the entire transfer tube and have a conductance of about 11 liters per second. Following the bellows, a 3 inch section of 0.5 inch OD tubing finishes the narrow section of the transfer tube. This small

section has a conductance of about 1.9 liters per second and is directly welded into a larger diameter elbow.

2.3.3 Science Cell

The science cell is a borosilicate glass fluorometer cell (from Starna cells) with an interior height of 10 mm, width of 20 mm, and length of 45 mm. The cell is attached to a glass-to-metal flange. This is attached to the elbow as shown in Fig. 2.3. This elbow is attached to a large diameter section containing the titanium sublimation pump (TSP) and the science region's ion pump. The TSP cartridge (Varian part number: 9160050) contains three filaments of titanium. After baking the science cell, current was passed through a filament heating it until titanium was evaporated and deposited onto the vacuum chamber's walls. The large surface area of titanium creates the pumping surface. Titanium absorbs hydrogen and reacts with nitrogen, oxygen, and other gases. These interactions create impressive pumping speeds of a few liters per second for every square centimeter, meaning our TSP's speed could be as high as 1000 liters per second. Although impressive, these speeds are only possible for sufficiently reactive or absorbable gases. Noble gases and methane are not pumped by the titanium and require the ion pump. We apply a new titanium layer about once a year.

2.4 Magnetic Traps and Fields

In this section I will describe the magnetic traps and magnetic fields we use to control the atoms. These fields are generated by passing current through coils located near the vacuum chamber. The magnetic fields must have particular spatial geometries to trap the atoms and we use two typical geometries, a quadrupole field and Ioffe-Pritchard field. The first type is used for the MOT and for transferring atoms to the science cell. The second type is used to trap and evaporatively

cool the atoms. While the atoms are in the second trap, we use microwave and radio-frequency (RF) oscillating magnetic fields for evaporative cooling. These fields require a special set of coils designed to broadcast the microwave and RF fields at the atoms.

2.4.1 Quadrupole and Transfer Trap

The quadrupole fields for the MOT and the transfer trap are generated by the same pair of coils. The coils are wound from square hollow tubing have 20.5 turns each. They have an inside diameter of 3.2 inches and an outside diameter of approximately 4.9 inches and a 0.7 inch thickness. They are centered on the transfer tube with a face-to-face separation of 4.25 inches. At the maximum current of our power supply, 440 A, the coils can generate magnetic-field gradients of about 180 G/cm. We move the coils using a linear positioner (Parker 404XR series). This positioner has a total travel length of about 800 mm.

2.4.2 Ioffe-Pritchard Trap

The Ioffe-Pritchard trap [44] is similar to the trap for the ^{85}Rb - ^{87}Rb experiment's trap [37]. Tracy Keep from the JILA machine shop helped design the trap. Figure 2.5 is a view of only the coils from Tracy's computer model. It has two elongated "racetrack" coils for the Ioffe coils that are electrically connected in series with the pinch coils. The bias coils are electrically separate.

We control the fields produced by the coils in the Ioffe-Pritchard trap by controlling the current that passes through them. Since there are two electrically separate sets of coils, we have two servos for stabilizing the currents in each set. This, in turn, stabilizes the magnetic field for the atoms.

All of the coils are made of square copper tubing. The tubing is wrapped in a polyimide coating to minimize electrical shorts. However, we discovered a weak



Figure 2.5: A schematic of the coils of the Ioffe-Pritchard magnetic trap. The large circular pair of coils are the bias coils. The small circular pair of coils are the pinch coils. Finally, the elongated, “racetrack” pair of coils are the Ioffe coils. Electrically, the Ioffe and pinch coils are connected in series. The bias coils are connected in series with each other but are electrically separate from the other coils.

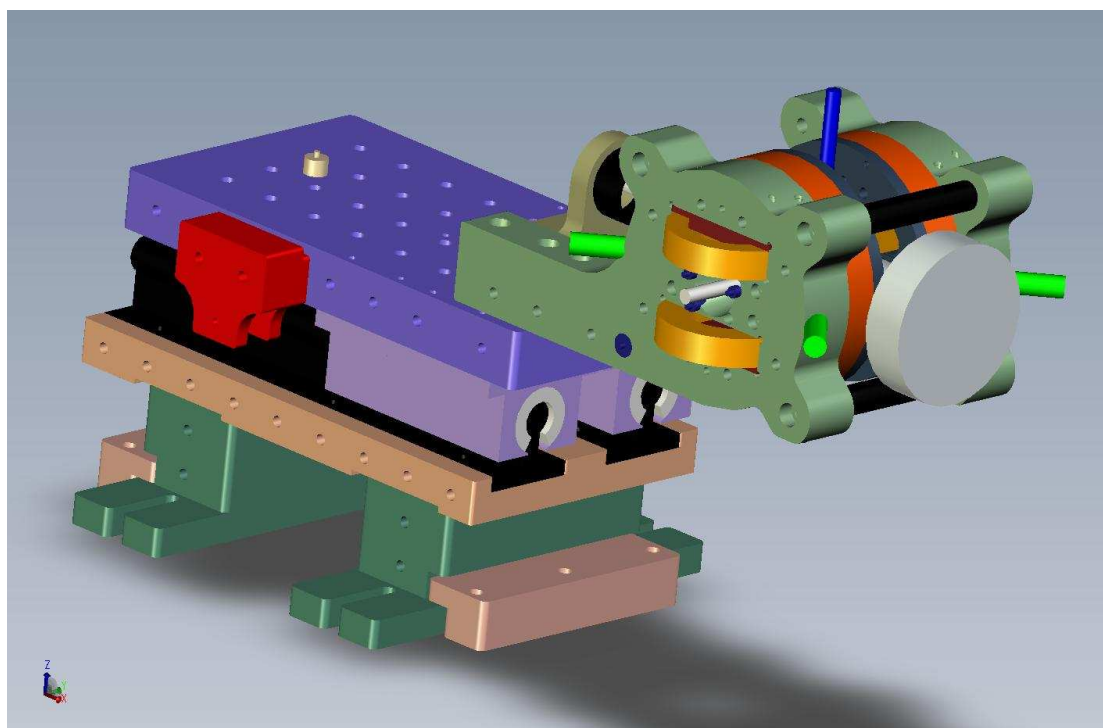


Figure 2.6: A computer generated model of the magnetic trap and its holder.

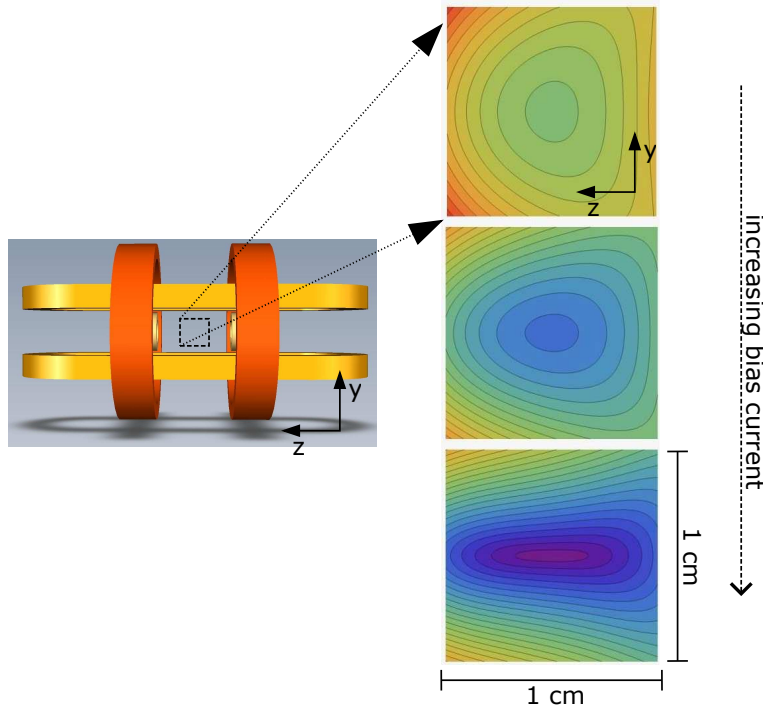


Figure 2.7: Contour plots of the magnitude of the magnetic field produced by a Ioffe-Pritchard Trap. The data is obtained from a computer model of the magnetic field using our coil geometry and dimensions. The horizontal direction of the plot is along the direction of the bias magnetic field. The vertical direction of the plot corresponds to the radial direction of the trap. The color scale is the same for each plot with purple corresponding to a low magnetic field and red corresponding to a high magnetic field. For each plot the current in the Ioffe coils and pinch coils are fixed and have the same value. The difference between the plots comes from increasing the current through the bias coils from low current (top) to high current (bottom). By increasing the bias current, the magnetic trap's depth increases and the radial trap frequencies increase.

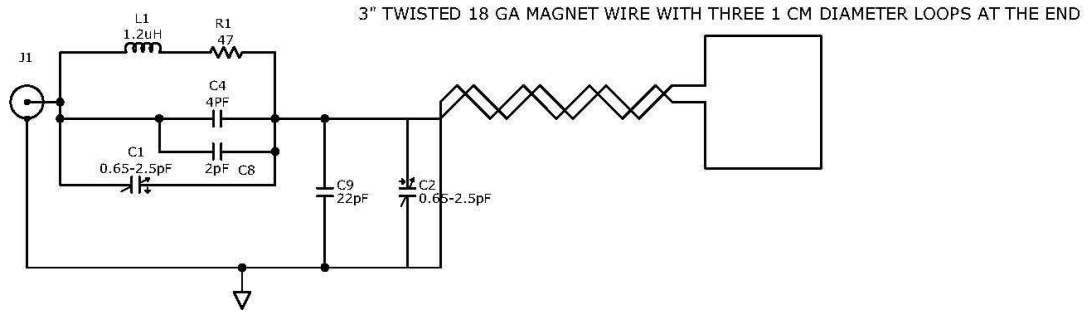


Figure 2.8: Circuit diagram of the rf coil that is impedance matched to 50Ω at DC-10MHz and near 80 MHz.

short in the Ioffe coils that was created in the coil winding process. See Appendix A for more details. We circulate chilled water through the coils to dissipate the heat generated through resistive heating.

2.4.3 Oscillating Magnetic Fields

We use rf and microwave frequency magnetic fields to control the internal states of the atoms. These fields are produced using two coils, one for rf and one for microwave.

The rf coil is designed to operate below 100MHz. The coil is made from two turns of 22 AWG wire with twisted-pair leads. The coil acts approximately like an inductor below its self resonance of about 300 MHz. We optimize the frequency dependent impedance of the coil to match 50Ω at DC-10 MHz and at 80 MHz. Figure 2.8 shows a circuit diagram of the coil.

The microwave coil is impedance matched at a slightly higher frequency than the ^{87}Rb hyperfine splitting (6.8 GHz) for the frequencies used for evaporation. It also is matched near 8 GHz for manipulation of the states of ^{87}Rb in a large magnetic field. The microwave coil is positioned in close in proximity to the atoms for improved coupling.

2.5 Optical Trap

In addition to trapping atoms with magnetic fields, it is also possible to trap atoms in optical fields. Using optical fields enables trapping of states that aren't magnetically trappable. Travis Nicholson constructed our first optical trap and general details of the trap can be found in his undergraduate honor's thesis [45]. We used his design to take our initial molecule data using magnetic-field sweeps.

Later, we modified his design to create a trap with a waist of $50\ \mu\text{m}$. This weaker trap was intended to lower the density of the atoms to reduce inelastic losses. The design was further modified after discovering that the 1075 nm fiber laser was causing significant loss of the Feshbach molecules. After this discovery, we replaced the 1075 nm multi-mode laser with a 1064 nm single-mode laser.

2.6 Imaging System

To detect the atom and molecule clouds, we resonantly drive optical transitions of the atoms and molecules with laser light. The clouds cast shadows in the laser beams. The shadows are imaged onto a CCD array of a digital camera. We use a Princeton Instruments MicroMAX 1024B camera (Model: MicroMAX-1024B). This camera has 16-bit readout resolution and 1024×1024 pixels with each pixel having dimensions $13.0 \times 13.0\ \mu\text{m}$. The quantum efficiency of the detector is about 75% at wavelengths of 780 nm.

We image the atom's shadow onto the camera using achromat lenses. The lens closest to the atoms has a focal length of 80 mm, a diameter of 25 mm and is placed about 80 mm from the atoms. The second lens has a focal length of 190 mm, a diameter of 50 mm and is placed about 270 mm from the first lens. Finally, the camera is placed about 190 mm from the second lens. Figure 2.9 shows the imaging layout.

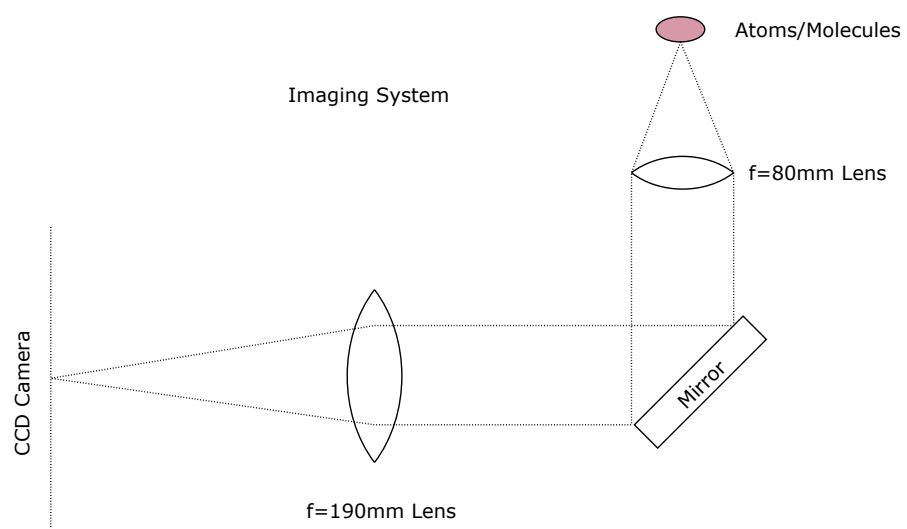


Figure 2.9: Imaging system used to detect the atoms and molecules.

2.7 Computer Control

We use computers to control the experimental timing. The computer controls up to 64 digital output lines using a digital input/output(DIO) board. This DIO board is made by Viewpoint Systems (model: 64-DIO64PCI). The DIO board's internal clock sets the timing for the entire experimental sequence. The computer also has three digital to analog converters (D/AC) boards made by National Instruments (model: NI-PCI6733). These D/AC boards are synchronized with the DIO board. Two of the PCI6733 boards generate 16 outputs of computer controlled analog voltages. The other PCI6733 board generates the detailed, time-dependent ramps for the optical trap.

Chapter 3

Methods

3.1 Introduction to Methods

In this chapter I will describe the techniques we use in preparing ultracold mixtures of ^{40}K and ^{87}Rb . Although these techniques are similar to those used in single-species experiments, they become slightly more complex because of interactions between the species [46, 47].

The prepared mixture should have temperatures and numbers that are adequate for association of atoms into molecules. Efficient association of ultracold atoms near a Feshbach resonance requires an ultracold atom gas near quantum degeneracy [48]. Quantum degeneracy in both ^{40}K and ^{87}Rb gases requires that the temperature of the gases is near the Fermi temperature (T_F) for ^{40}K and the BEC transition temperature (T_c) for ^{87}Rb . These degeneracy temperatures depend on the harmonic trapping potential and the number of atoms, N_K and N_{Rb} . They are given in Eqns. 3.1 and 3.2.

$$T_F = \frac{\hbar\bar{\omega}_K}{k_B} (6N_K)^{\frac{1}{3}} \quad (3.1)$$

$$T_c = \frac{\hbar\bar{\omega}_{Rb}}{k_B} \left(\frac{N_{Rb}}{1.202} \right)^{\frac{1}{3}} \quad (3.2)$$

Here, $\bar{\omega}$ is the geometric mean of the three angular trapping frequencies, k_B is the Boltzmann constant, and \hbar is the Planck constant divided by 2π . Since we

want both gases to be near quantum degenerate, we need these temperatures to be approximately equal, $T_F \approx T_c$. We typically prepare atom gasses with a number ratio of $N_{\text{Rb}}:N_{\text{K}}$ about 3:1. The evaporation is stopped when the temperature of the atom clouds reaches about $T = 1.2 T_c$ and $T = 0.6 T_F$.

3.2 The MOT

As mentioned previously, we use a two-species magneto-optical trap (MOT) to capture and cool atoms from a room-temperature vapor. The MOT uses three retroreflected laser beams that mutually intersect at the zero of a quadrupole field with a 10 G/cm gradient along the vertical direction. The laser beams have frequencies that are slightly lower than the ^{40}K and ^{87}Rb cycling transitions and are combined with light that is tuned to the repump transition for the atoms. Since the exponential fill time in the MOTs is typically around three seconds, we capture atoms in the MOTs for at least 15 seconds to ensure complete filling of the MOTs. The densities within the MOTs are limited by radiation trapping in the optically thick clouds. To increase the densities of the clouds for loading into the quadrupole trap, we compress the MOT [49] by reducing the repump beams' optical power and changing the trap lasers' detuning. After compressing, we further cool the ^{87}Rb gas using a molasses stage. The molasses stage is done in the absence of the quadrupole field. Finally, the MOT laser beams are turned off and, in a weak magnetic field, we optically pump the atoms into the weak-field seeking “stretched state” for both ^{87}Rb and ^{40}K ($|2, 2\rangle$ and $|9/2, 9/2\rangle$, respectively).

After optically pumping the atoms, the quadrupole magnetic field is turned on again to capture the spin polarized atoms. First the clouds are loaded into a weak (30 G/cm vertically) trap for 200 ms. This trap only holds ^{87}Rb in the $|2, 2\rangle$ state while possibly holding up to seven spin states of ^{40}K . After the 200 ms filter time, the trap is then linearly ramped to 100 G/cm in 700 ms. Ramping to the

strong gradient compresses the atom clouds in preparation for the transfer to the science cell.

Recapturing atoms into the MOT is simple and useful for diagnosing problems with the preparation steps. We do this by suddenly turning the MOT back on to its normal operating parameters. We can then sensitively detect the MOT fluorescence and compare this to the fluorescence of a full MOT. For example, Figure 3.1 shows MOT recapture after loading ^{87}Rb atoms into the quadrupole trap versus the vertical trapping gradient. The atoms were held at each gradient for 200 ms, which is long enough for untrapped states to be lost. The two data sets were taken before (\triangle) and after (\bullet) optimizing the molasses cooling stages. The sharp step-like transitions occur at about 15 G/cm and 30 G/cm represent the gradient required to support different weak-field seeking states of ^{87}Rb against gravity. The states have magnetic moments of μ_B and $\mu_B/2$ respectively. For this data, the optical pumping was not optimized for the $|2, 2\rangle$ state as shown by the large increase in total number of recaptured atoms above 30 G/cm. We also use MOT recapture to measure the lifetime of the atoms in the quadrupole trap inside the MOT cell. Typically, this lifetime is about 2 seconds. As discussed in the next section, the atom clouds can be transferred to other locations along the transfer tube then back to the collection cell for MOT recapture. Using this technique, we can measure the lifetime at different locations in the vacuum chamber.

3.3 The Transfer

We transfer the atoms from the MOT cell to the science cell using a linear positioner (also known as “the track”) [50]. The relatively short magnetic-trap lifetime of 2 seconds in the MOT cell limits the number of atoms we can efficiently transfer from the MOT to the science cell. We begin the transfer from the MOT cell 500 ms after the load of the weak quadrupole trap. This occurs while the trap

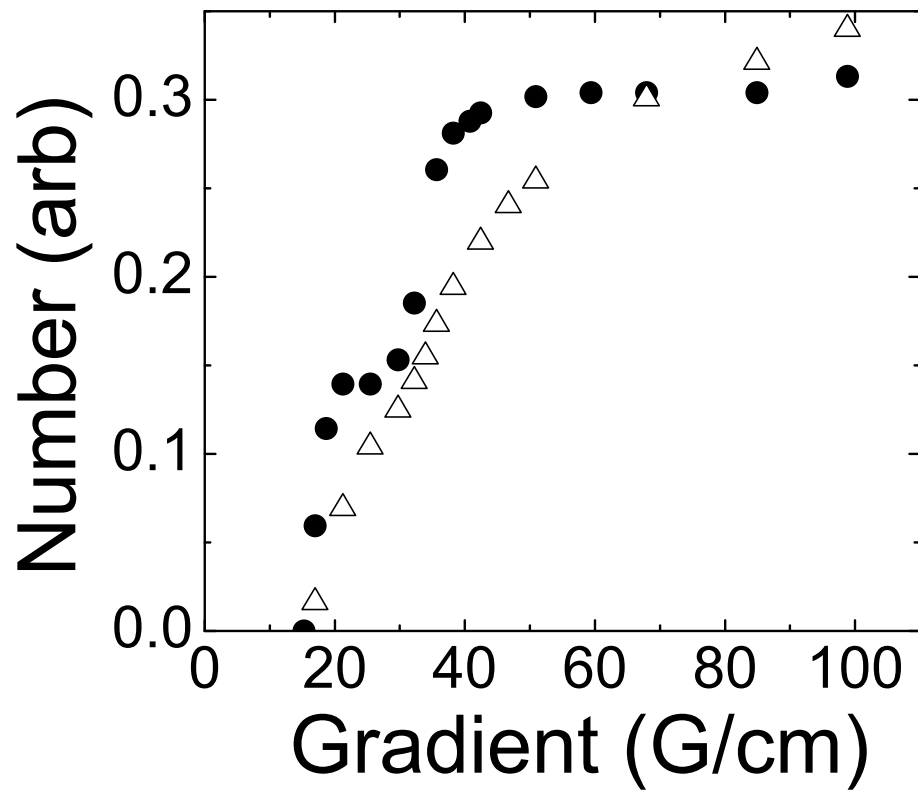


Figure 3.1: Number of ^{87}Rb atoms recaptured into the MOT after loading a quadrupole magnetic trap. The atoms are held at the indicated gradients for 200 ms. The two data sets are before (\triangle) and after (\bullet) optimizing the molasses stage before the quadrupole load. Optical pumping is not optimized.

is ramping to 100 G/cm.

The positioner leaves the MOT's position with an acceleration of 1 m/s^2 for 340 ms until it reaches a speed of 34 cm/s. After traveling 15.25 cm, the cart slows to 20 cm/s in 140 ms for the bump region. This speed was chosen by minimizing losses past the bump. Here, the cloud's position is shifted vertically by a static bias magnetic field provided by a pair of coils. These coils are turned on well before the positioner reaches the bump region. To avoid the pyrex obstruction, the position of the cloud needs to shift downward by about 1 cm. A bias field of about 100 G is needed for this shift. Figure 3.2 shows the result of transferring past the obstruction as a function of current in the bias coils. The decrease in efficiency for large currents (large bias fields) is caused by too large of a vertical shift pushing the cloud into the wall of the vacuum chamber. After optimizing, the efficiency of transferring atoms past the bump is about 97%. This efficiency is determined by comparing the number of atoms transferred past the bump to the number transferred to just before the bump. The overall efficiency to the science cell is about 10% of the full MOT. This is quite low relative to other track systems and is caused, predominantly, by the transition into the first section of the transfer tube (40% efficient) and the short lifetime of the trapped atoms in the MOT cell (60% efficient). Additional contributions to the loss are the optical pumping (70% efficient) and losses in the bellows section of the transfer tube (70% efficient). Except for the optical pumping, it should be possible to improve these losses. For example, lengthening the initial section of transfer tube so that its opening is closer to the MOT position would minimize the time that the atoms spend in the high-pressure MOT cell. It could also make it easier to apply magnetic shim fields to efficiently "funnel" the atoms into the tube. The losses at the bellows are probably caused by magnetic fields that can also be shimmed.

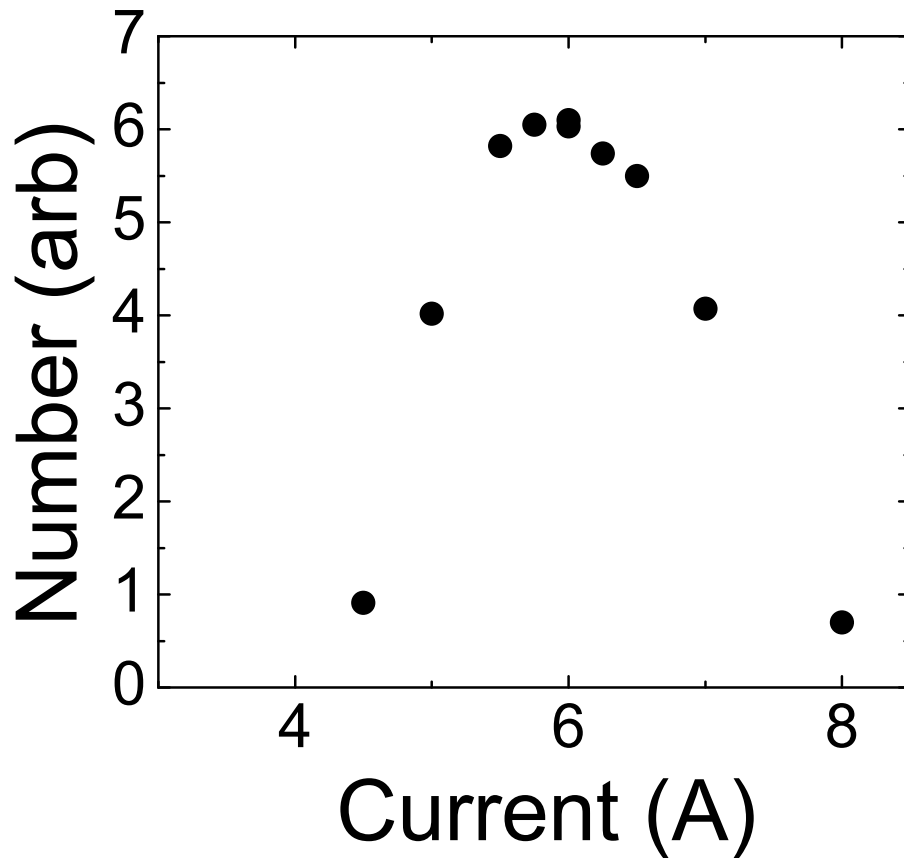


Figure 3.2: Number transferred past the “bump” as a function of current in the bump coils. The optimized transfer efficiency across only the bump is about 97%. This efficiency is calculated by comparing the number transferred past the bump to the number transferred to just before the bump. It is important that the speed of the track is less than 20 cm/sec for the best transfer efficiency across the bump. The pyrex obstruction totally blocks the cloud’s path for currents below 4.5 amps and the vacuum chamber wall totally blocks the cloud’s path for currents above 8 amps.

3.4 IP Evaporation

After transferring the mixture to the science cell, we load the a weak Ioffe-Pritchard trap by turning on the pinch-Ioffe bar coils to 220 amps and the bias coils to 20 amps. At these currents, the measured ^{87}Rb trapping frequencies in the $|2, 2\rangle$ state are $\omega_z = 2\pi \cdot 20$ Hz and $\omega_r = 2\pi \cdot 23$ Hz. We then compress the trap by increasing the current in the bias coils to 88 amps. At these currents, the magnetic fields from the pinch coils and bias coils nearly cancel. The bias field here is about 1.7 gauss and the trap frequencies are $\omega_z = 2\pi \cdot 20$ Hz and $\omega_r = 2\pi \cdot 156$ Hz. At the start of evaporation, we typically have about $3 \cdot 10^8$ ^{87}Rb atoms and $2 \cdot 10^6$ ^{40}K atoms at about 500 μK .

We evaporatively cool the ^{87}Rb gas by driving the $|2, 2\rangle \rightarrow |1, 1\rangle$ transition. By sweeping the microwave frequency from high to low, the most energetic atoms are removed leaving the remaining atoms at lower temperatures. The evaporation efficiency depends on the microwave power, time-dependence of the frequency sweep, and the collision rate in the gas. Others have discussed the intricacies of evaporative cooling and details can be found in Ref. [51] and references therein. The ^{40}K gas is sympathetically cooled by collisions with ^{87}Rb atoms. Figure 3.3 shows the effect of the forced/sympathetic evaporation on the atom clouds. The ^{87}Rb and ^{40}K clouds are cooled at the expense of ^{87}Rb atom number.

The first data we obtained on sympathetic cooling showed significant number losses in the ^{40}K cloud near the end of evaporation. If we didn't load ^{40}K , we discovered that there was an impurity of ^{87}Rb in the $|2, 1\rangle$ state at the end of evaporation. However, if we loaded ^{40}K , the $|2, 1\rangle$ state was depleted along with the ^{40}K . The microwaves do not depopulate this state and inelastic losses in ^{87}Rb are low. Initially, we thought these atoms were being created throughout the evaporation by optical or rf fields but the number of atoms in the $|2, 1\rangle$

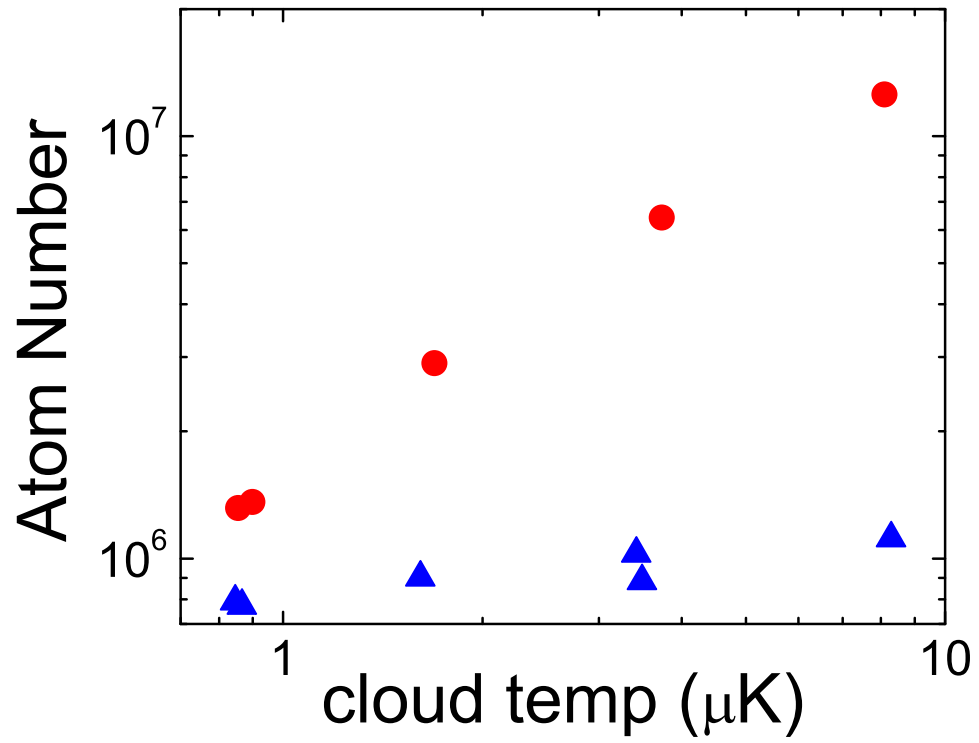


Figure 3.3: Effect of forced evaporative and sympathetic cooling on the temperature and number of both atomic species. The clouds' temperature decreases at the expense of ^{87}Rb atom number (solid circles). The ^{40}K atom number (solid triangles) is only slightly affected.

state remained constant throughout the experiment. Presumably, the atoms do not adiabatically follow the local magnetic field during the transfer of atoms from the quadrupole trap into the Ioffe-Pritchard trap. To remove the $|2, 1\rangle$ atoms, we continuously drive the $|2, 1\rangle \rightarrow |1, 0\rangle$ transition at the magnetic field of the bottom of the trap throughout the microwave evaporation.

3.5 Optical Trap Evaporation

After evaporation in the Ioffe-Pritchard magnetic trap we have 5×10^6 Rb and 1×10^6 K atoms at $3 \mu\text{K}$. These atoms are transferred into a far-off-resonance optical dipole trap with a $50 \mu\text{m}$ waist derived from a single-frequency fiber laser operating at a wavelength of 1064 nm . The dipole trap is a convenient tool for trapping atoms having Zeeman states that aren't magnetically trappable. These states are immune to two-body inelastic losses and have the Feshbach resonance used to create the Feshbach molecules discussed in Ch. 4. Once the optical dipole trap is loaded, we use rf adiabatic rapid passage to transfer the atoms into the magnetically untrappable $|1, 1\rangle$ and $|9/2, -7/2\rangle$ states of ^{87}Rb and ^{40}K , respectively. The gases are then simultaneously evaporated at a field of $B=540 \text{ G}$ by lowering the optical power in the trapping beam until 3×10^5 Rb at $T/T_c \sim 1$ and 1×10^5 K at $T/T_F \sim 0.6$ remain. T_c is the critical temperature for the onset of Bose-Einstein condensation (BEC) and T_F is the Fermi temperature. At the end of the optical trap evaporation we adiabatically increase the optical trap power until the measured radial trapping frequencies are $211 \pm 4 \text{ Hz}$ and $136 \pm 2 \text{ Hz}$ for K and Rb, respectively. The ratio of these frequencies is 1.55 ± 0.04 . Assuming a harmonic potential, the ratio should be given by $\sqrt{\frac{m_{\text{Rb}}}{m_{\text{K}}}} \approx 1.47$. The discrepancy is resolved because the potential is not harmonic. The disparity in atomic mass causes the two clouds to be pulled by gravity to different equilibrium positions in the trapping beam. The ^{87}Rb cloud is in a lower and more anharmonic region of

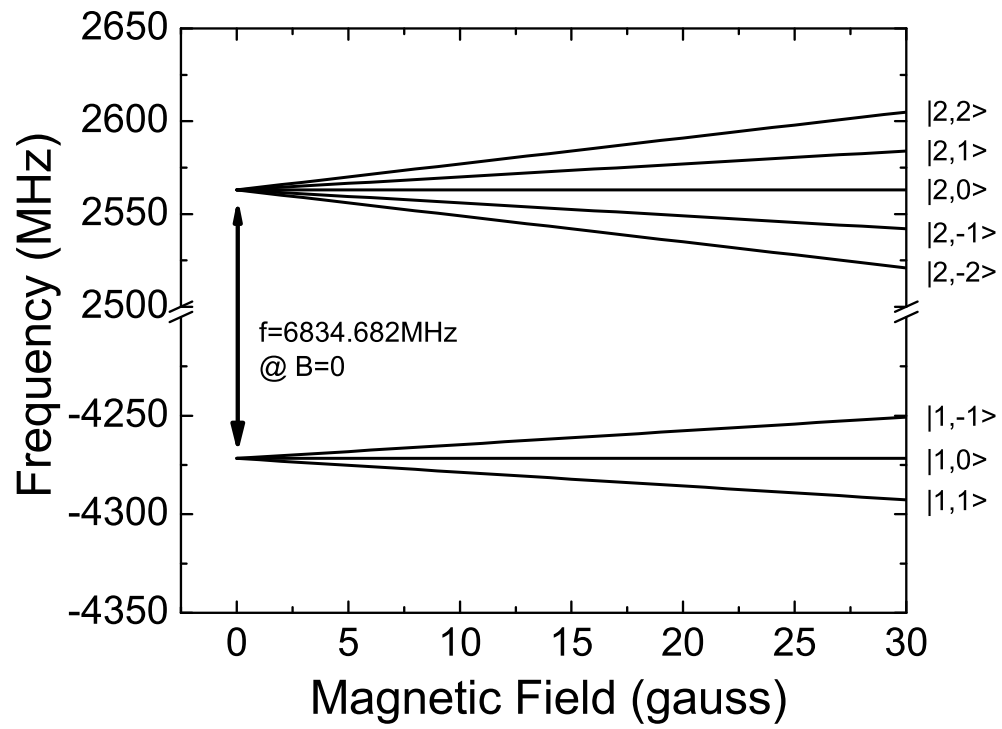


Figure 3.4: Breit-Rabi diagram for ^{87}Rb at low magnetic field. We evaporatively cool the ^{87}Rb gas by driving the $|2,2\rangle \rightarrow |1,1\rangle$ transition. This removes ^{87}Rb atoms from the magnetic trap. We also drive the $|2,1\rangle \rightarrow |1,0\rangle$ transition to remove impurity states of ^{87}Rb that inelastically collide with ^{40}K .

the trapping beam. Here the ^{87}Rb trap frequency should be lower than the one calculated using the ^{40}K trap frequency and assuming a harmonic potential.

3.6 Absorption Imaging

We extract the number and temperature of the atoms from time-of-flight, resonant absorption images. The gas is suddenly released from the trap and allowed to freely expand before imaging. Using a resonant light pulse of the appropriate frequency, we selectively image the shadow cast by K or Rb atoms in a particular spin state. The number and temperature are extracted by analyzing the spatial variation of the optical depth of the cloud. We use similar imaging techniques as other groups, see, for example, Jacob Roberts's thesis [52](Sec. 4.11).

Chapter 4

Creation of Feshbach Molecules

4.1 Feshbach Resonance

Magnetic-field-tunable Feshbach resonances, also known as Fano-Feshbach resonances, are useful tools for controlling the interactions between ultracold atoms. Their utility has been demonstrated in a variety of situations. For example, Feshbach resonances are used for the efficient evaporation of ^{85}Rb [53, 52] and ^{133}Cs [54], which has led to BEC in those species. In ^{85}Rb , the interacting BEC has been studied under the influence of changing the scattering length [53, 55, 56, 57]. Feshbach resonances have also been used to efficiently evaporate Fermi gases and have allowed for detailed studies of the BCS-BEC crossover [34]. Finally, Feshbach resonances have been used to convert ultracold atoms into molecules [58, 59, 48]

Feshbach resonances in ultracold alkali collisions has been reviewed elsewhere [19]. Briefly, the resonance results when a ro-vibrational molecule state in a closed channel is coupled to the open, scattering channel. In our case, the relative energies of the closed-channel bound state and the open-channel threshold can be tuned with a magnetic field since the magnetic moments between the two channels are different. This is shown schematically in Fig. 4.1.

Weakly bound molecules can be efficiently created from atoms if the magnetic field is swept slowly across the Feshbach resonance in a direction that takes

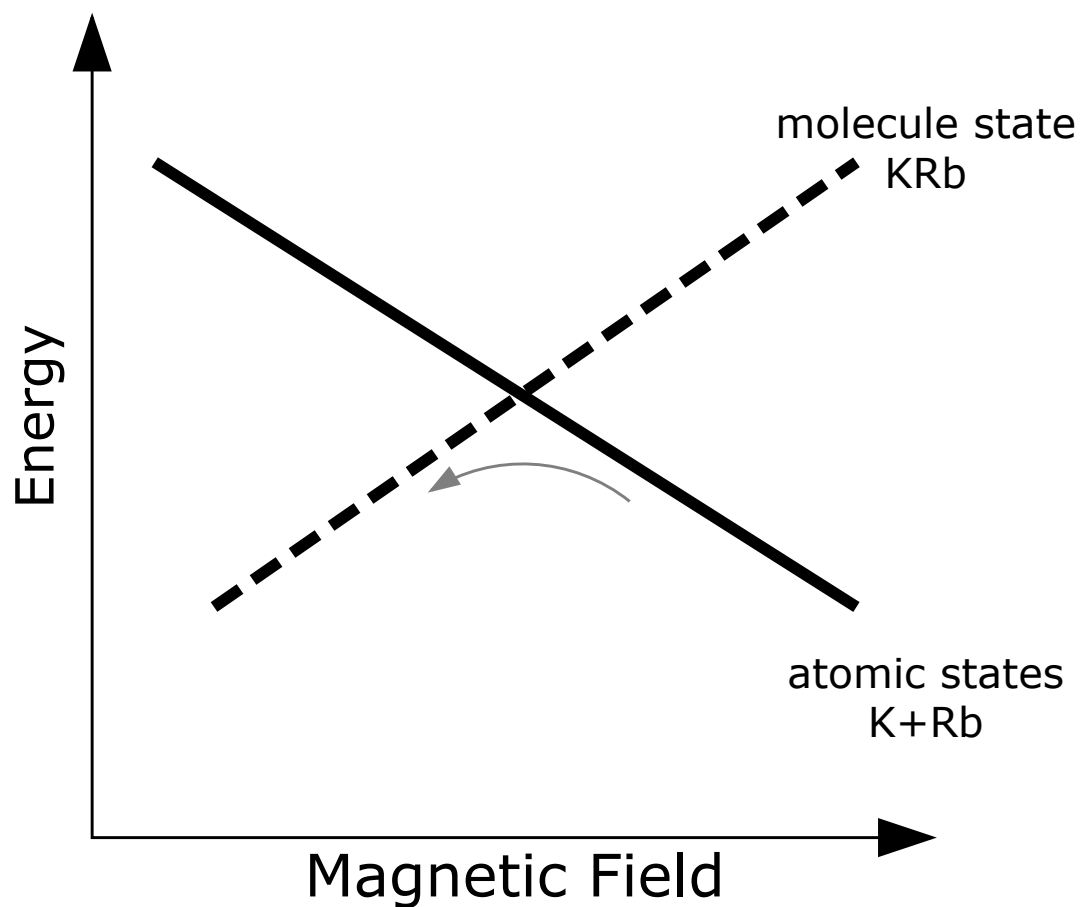


Figure 4.1: Magnetic field can be used to tune a closed molecular state and the open atomic states into degeneracy. The different magnetic moments of the two states allow the tunability. If these states are coupled, a Feshbach resonance will occur at a magnetic field in the vicinity of the crossing between the two states. The grey arrow indicates how the molecule state can be populated with a slow magnetic-field sweep.

the closed channel state from higher energy to lower energy relative to the open channel [60, 18, 59, 48]. In Fig.4.1, this direction is shown by lowering the magnetic field through the crossing. Hodby *et al.* [48] has described this technique in detail. Briefly, the crossing is analogous to an avoided crossing in a two-level system. Like a two-level crossing, the rate of the magnetic-field sweep near the Feshbach resonance controls the population that is converted into the molecular state. However, it is not exactly like a two-level crossing. In particular, the closed-channel molecule state is coupled to the continuum of states connected to the open-channel. When the closed-channel has a higher energy relative to the open-channel threshold (the right side of Fig 4.1), this coupling causes the closed-channel to have a finite lifetime. A further complication to the two-level analogy is that the molecule formation process depends on pairs of atoms that are near to one another in phase-space. Therefore, the atom gases may not be totally converted into molecules during a sweep if the atoms are not close enough in phase-space.

In addition to magnetic-field sweeps, the closed channel can be populated using oscillating magnetic fields. This technique has been utilized in other experiments when crossing the resonance is not favorable [61, 46, 62]. Furthermore, this technique has been extended to the radio-frequency (rf) domain and used to couple atoms of another spin state into Feshbach molecules [63, 3].

4.2 Our Early Attempts

When we began our search for the known resonance positions in 2006, there was some uncertainty in the assignment of the ro-vibrational states that were coupled to the open channel. JILA first reported ^{40}K and ^{87}Rb interspecies resonance locations in the energetically lowest states of ^{40}K and ^{87}Rb [64]. These resonances were assigned particular partial wave character using a comparison

with theory. However, later the LENS group repeated and expanded upon this measurement and determined that the assignment was incorrect [65]. Their assignment was based on both theory and the qualitative observation that the width of a suspected p-wave resonance was smaller at lower temperatures.

We repeated these measurements not only to ensure our magnetic field was calibrated but also to determine if the suspected p-wave resonance was in fact p-wave. The measurements were performed starting with a cold mixture in an optical trap with ^{87}Rb atoms in the $|1, 1\rangle$ state and ^{40}K atoms in the $|9/2, -9/2\rangle$ state. We ramped the magnetic field to a location near the resonance position and held the atoms at this field for one second. During the hold time, inelastic losses could deplete the clouds. Afterwards, the field was turned off and the clouds were imaged to determine the loss. Figures 4.2 and 4.3 shows two of the loss curves. The s-wave resonance is located near 546 gauss as shown in Fig. 4.2. The losses are maximized at the resonance locations. The double peaked structure of Fig. 4.3 shows the p-wave resonance. Here we measured the positions to be 515.18 ± 0.06 gauss and 515.32 ± 0.06 gauss for the two peaks. The uncertainty comes from the magnetic-field calibration. The double-peaked structure is understood [66] and results from the magnetic dipole-dipole interaction of the atoms. These results confirmed that this was a p-wave resonance, as reported by the LENS group.

As mentioned previously, the magnetic field can be swept in the vicinity of the Feshbach resonance. We ramped the magnetic field across the resonance as shown in Fig. 4.4. Figure 4.5 shows the atomic response to these ramps. The data is consistent with molecule formation when the magnetic field is ramped appropriately.

We also used the ramp experiments to find the resonance locations. In principle, this should be more accurate than using the inelastic loss measurements since the inelastic loss rate may not peak exactly on resonance. We prepared

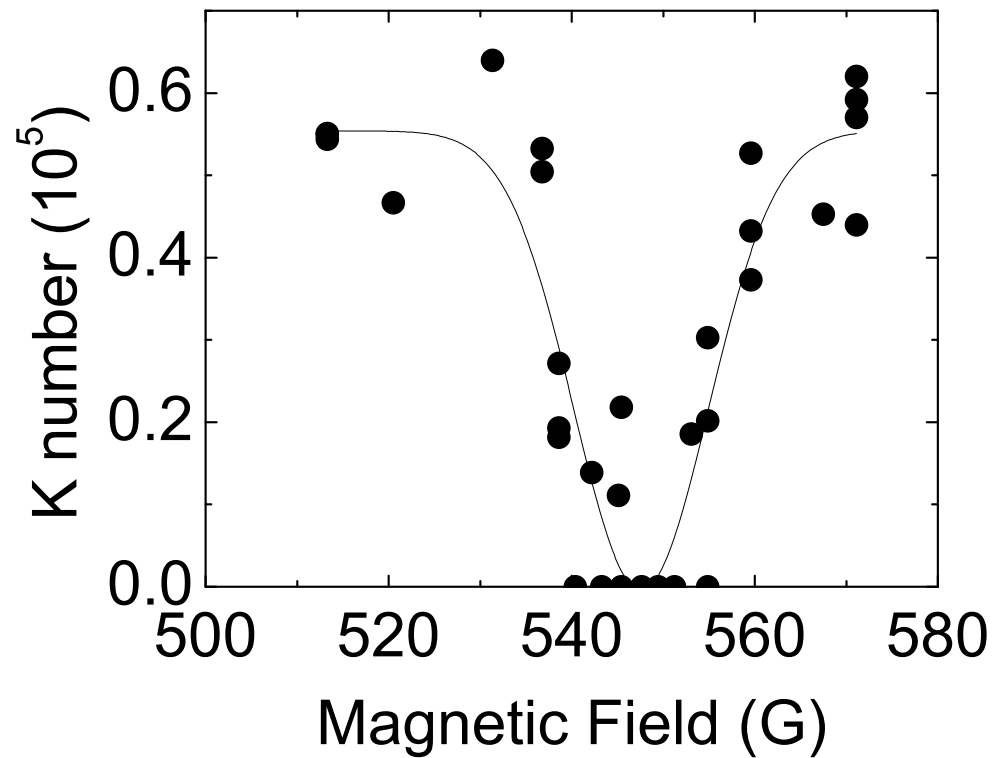


Figure 4.2: Loss of K atoms in the presence of Rb resulting from an interspecies s-wave Feshbach resonance. The atoms are in the $|9/2, -9, 2\rangle_K$ and $|1, 1\rangle_{Rb}$ states and are held at the indicated field for one second before abruptly turning off the magnetic field and imaging them. For this measurement the number of ^{40}K atoms was about 10^5 and the number of ^{87}Rb atoms was about $5 \cdot 10^5$. Both clouds were initially in thermal equilibrium at a temperature of about 500 nK.

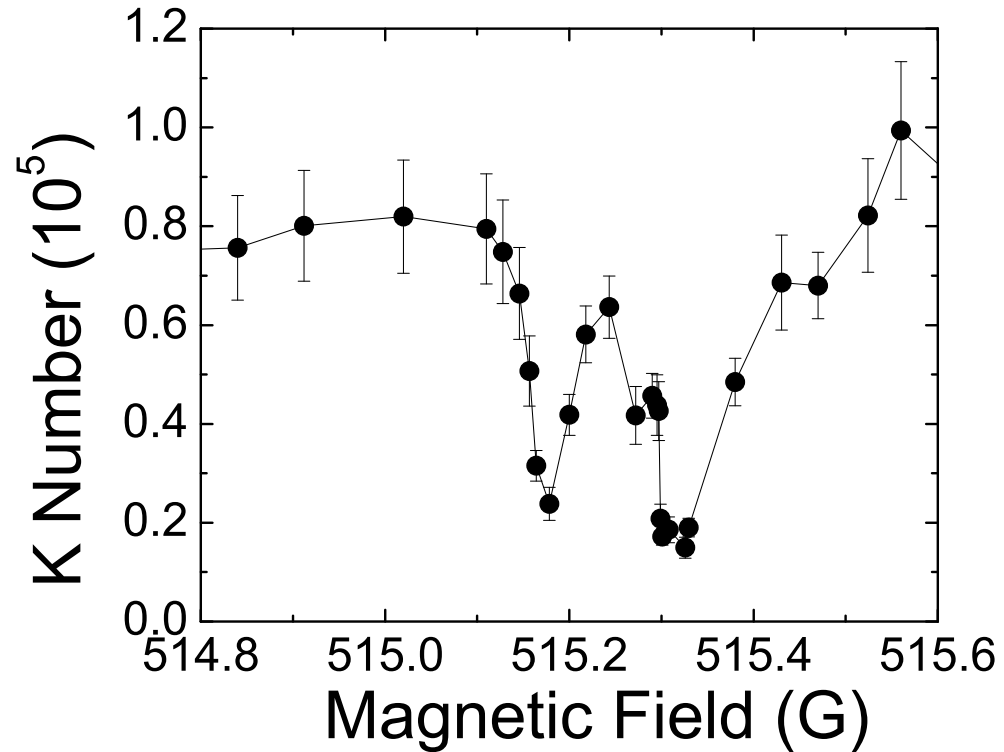


Figure 4.3: Loss of K atoms, in the presence of Rb, resulting from an interspecies p-wave Feshbach resonance. The atoms are in the $|9/2, -9, 2\rangle_K$ and $|1, 1\rangle_{Rb}$ states and are held at the indicated field for one second before abruptly turning off the magnetic field and imaging them. For this measurement the number of ^{40}K atoms was about 10^5 and the number of ^{87}Rb atoms was about $5 \cdot 10^5$. Both clouds were initially in thermal equilibrium at a temperature of about 500 nK.

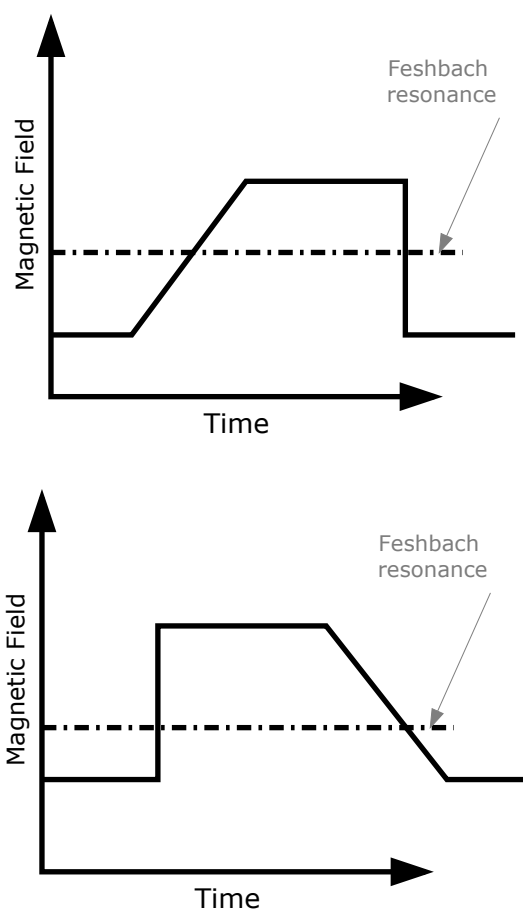


Figure 4.4: Solid lines show the time dependent ramps near the Feshbach resonance. The top figure shows a ramp that should not create molecules. The lower figure shows a ramp direction that should create molecules.

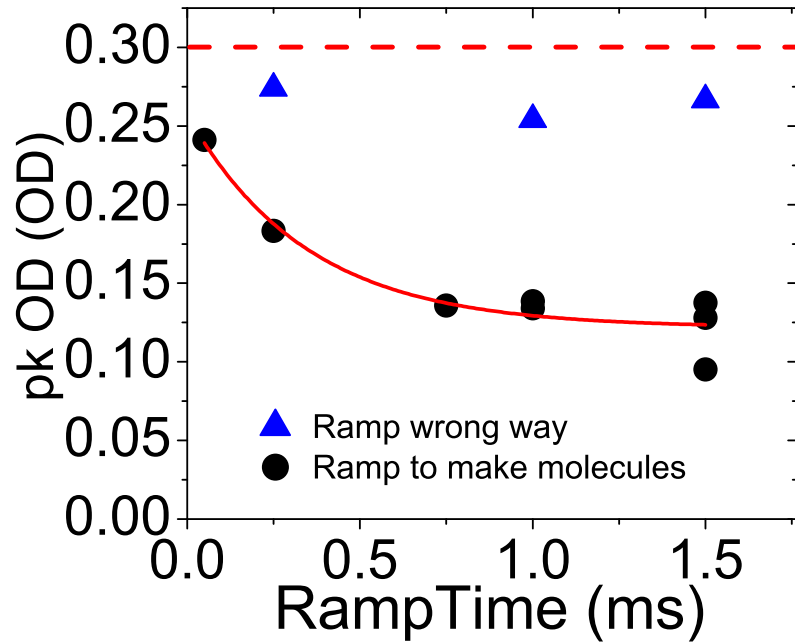


Figure 4.5: The peak optical depth of K after ramping across the Feshbach resonance. The time to complete the ramps of Fig. 4.4 was adjusted. The atomic loss is consistent with molecule formation after ramping slowly from high to low magnetic field (solid circles). The time spent near the resonance is not a significant factor for atomic loss since little loss is observed after ramping slowly from low to high magnetic field (solid triangles). The dashed line indicates the initial optical depth of the K cloud without ramping across the resonance. The optical depth was measured after 12ms of free expansion.

^{40}K and ^{87}Rb in the $|9/2, -9/2\rangle$ and $|1, 1\rangle$ states, respectively, and ramped the magnetic field in the vicinity of the Feshbach resonance as shown in Figure 4.6. Here, the ramps are slow enough to ensure molecule creation can proceed efficiently but not so slow that inelastic losses dominate [48]. By measuring where molecule formation occurs, we can measure the resonance location. We varied the hold magnetic field while observing the atom number. The results are shown in Figure 4.7. With this measurement, we measured the s-wave resonance location to be 546.47 ± 0.12 gauss. We fit the data using an error function. The uncertainty given here corresponds to the 10%-90% width of the transition. This data was taken with the atoms held in the optical trap where the atomic densities were high which could lead to losses near the resonance. Such losses could cause the measured location of the Feshbach resonance to be shifted systematically to lower magnetic fields. Since this data was taken using only ramps that approach the Feshbach resonance from below, the losses near the resonance could be caused by three-body recombination or two-body photoassociation from the trapping laser instead of two-body Feshbach molecule formation.

At this point, we were able to create molecules but could only detect loss of atoms and could not detect the molecules directly. Being able to directly detect the molecules is important for further studies of molecular properties.

4.3 Molecule Lifetime

After creating the molecules, our goal was to find their lifetime and what limited it. We had intentionally selected the lowest-energy Zeeman states for each of the atoms. This choice eliminates inelastic two-body, or dipolar, losses since they are energetically forbidden. However, three-body losses can occur through a process called vibrational quenching. This occurs when vibrationally excited molecules release their vibrational energy through collisions with other atoms

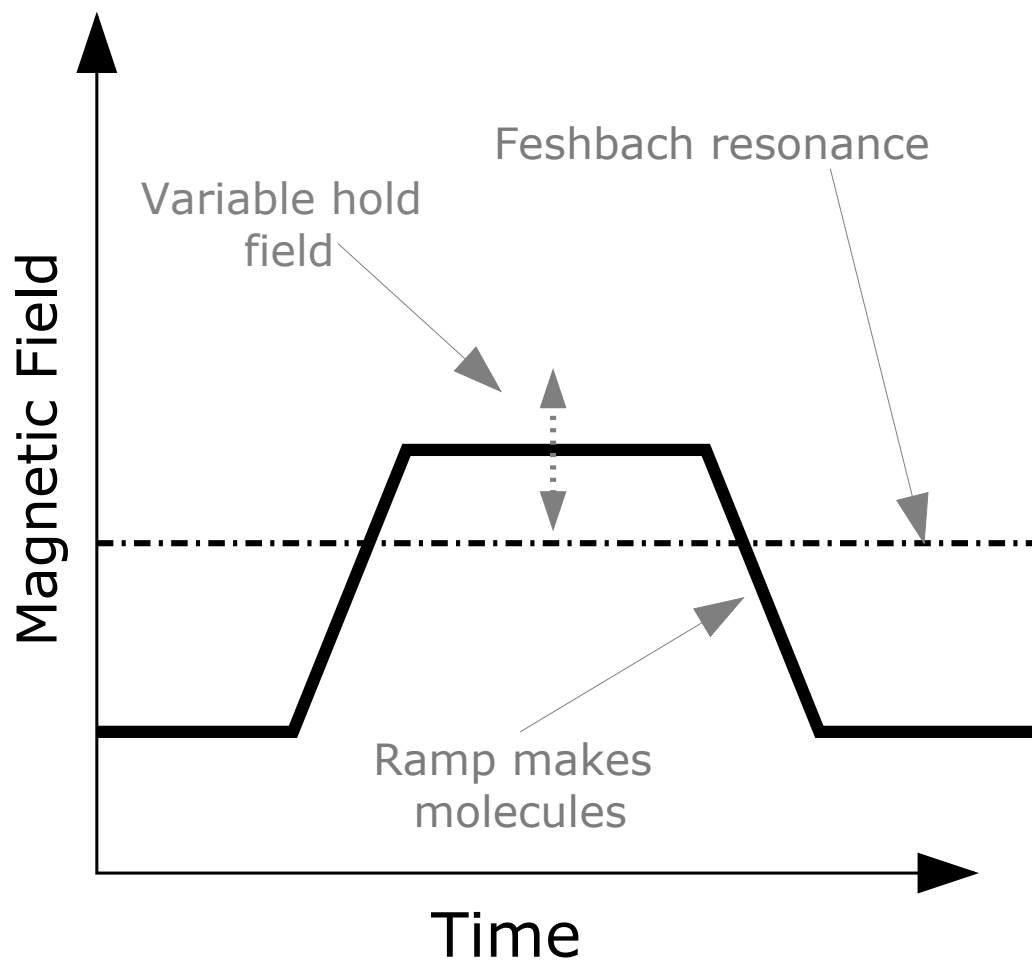


Figure 4.6: Solid line shows a typical time-dependent magnetic-field ramp near the Feshbach resonance. The hold magnetic field was changed for each data point of Fig 4.7. The ramps up to and away from the hold field were adiabatic for creating molecules.

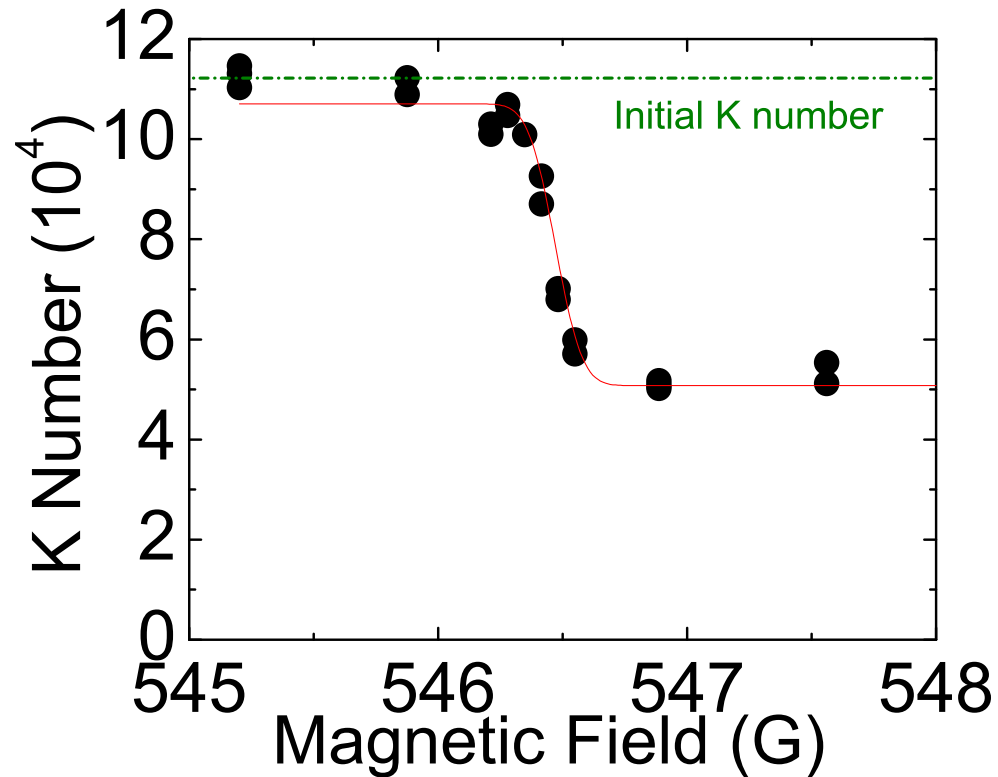


Figure 4.7: Finding the resonance location using time-dependent magnetic-field ramps. The transition to more loss occurs when the hold field of Fig. 4.6 is above the resonance position. This loss is due to the creation of molecules which, in this experiment, were quickly removed by the optical trap light. The magnetic field was held for $300 \mu\text{s}$ and the ramps toward and away from the resonance had inverse ramp rates of 0.139 ms/gauss . The solid line is a fit, using an offset error function, to the data. B_0 is taken as the center of the fitted error function. The 10% to 90% width of the error function is taken as the uncertainty in B_0 . Using these criteria, we obtain $B_0 = 546.47 \pm 0.12 \text{ gauss}$. The initial ^{40}K and ^{87}Rb atom numbers were about $1.1 \cdot 10^5$ and $2.9 \cdot 10^5$ and $T = 240 \text{ nK} = 0.8T_c = 0.6T_F$. We detected the atoms at low magnetic field after turning off not only the optical trap but also the magnetic fields.

and molecules. Since collisions are not suppressed between Bosons, we suspected that inelastic collisions with the bosonic ^{87}Rb would occur at a relatively fast rate. We also suspected that, in analogy to other Fermi systems [67, 68], the molecule lifetime would be relatively long when it was limited by collisions with the fermionic ^{40}K .

Using a technique developed by others [68, 69], we attempted to measure the molecular lifetime by creating molecules, waiting a specific time for molecular loss to occur, and reconvertng the molecules back to atoms. We accomplished this by ramping across the resonance as shown in Fig. 4.8. The first, vertical crossing of the FR is diabatic and does not contribute significantly to atom loss. The ramp crossing the FR from above creates molecules and the second ramp breaks the molecules into atoms for low field detection. The final crossing of the FR is diabatic. The hold field and duration of the hold define the interesting parameter space.

By ramping across the Feshbach resonance to create molecules then ramping back to convert the molecules back into atoms, we were able to measure the molecule lifetimes. Results of a lifetime measurement are shown in Fig. 4.9. The measured lifetime is $220\ \mu\text{s}$ at a hold magnetic field of 546.2 ± 0.2 gauss.

These measurements suffered from the fact that we were not directly detecting the molecules, but rather, we were reconvertng the molecules back into atoms. The lifetime measurements were strongly affected by even modest fractional atom number noise. Also, the atoms were detected using absorption imaging at low magnetic fields. This means we were turning off the ≈ 547 gauss magnetic field while crossing the Feshbach resonance a final time. These limitations led us to consider new ways to detect the molecules in the absence of a fluctuation background.

As discussed in the next section, we found that we were able to directly

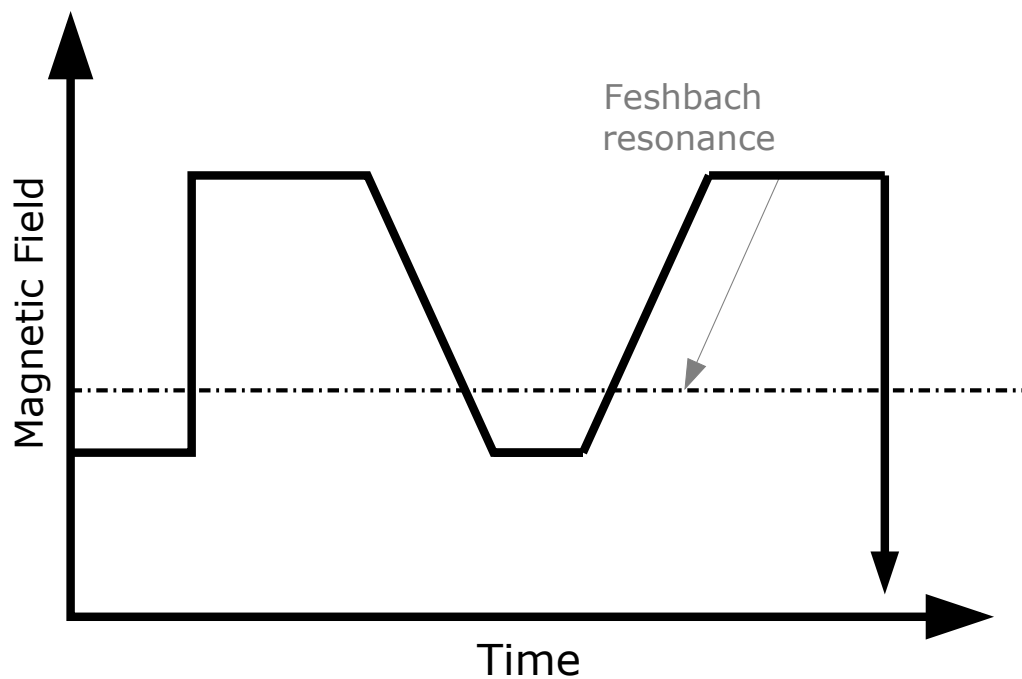


Figure 4.8: Magnetic-field ramp near the Feshbach resonance to create molecules, probe their lifetime, and reconvert the molecules to atoms for low magnetic-field imaging. The vertical jumps represent diabatic crossings of the resonance. The ramps are adiabatic for creating and dissociating molecules.

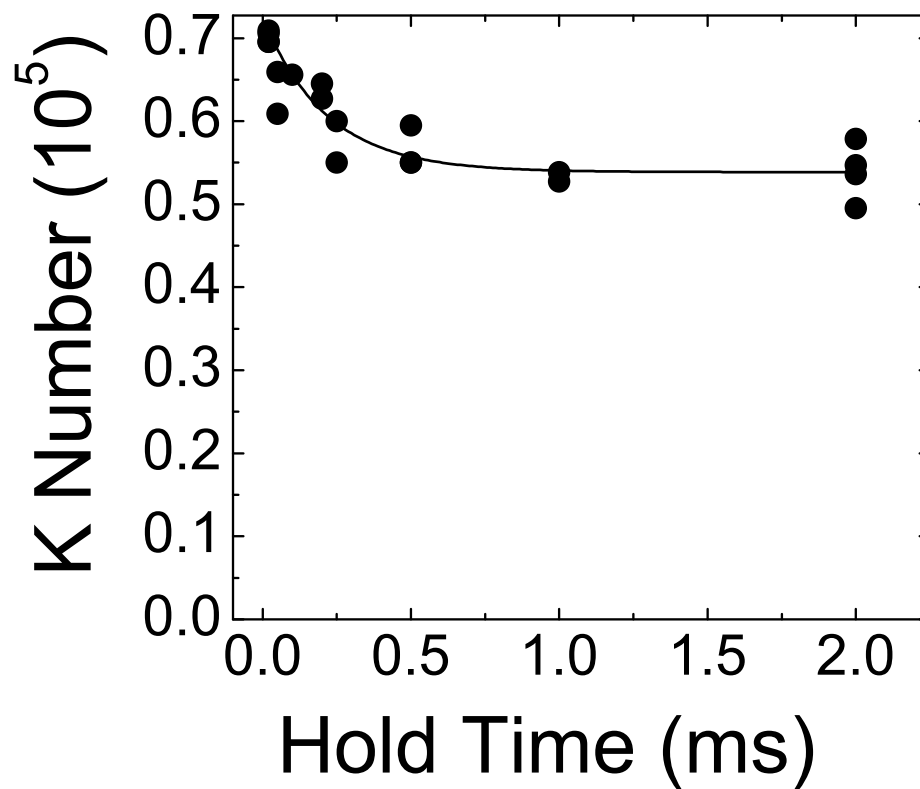


Figure 4.9: A measurement of the lifetime of molecules. We used magnetic-field ramps similar to Fig. 4.8 to reconvert the molecules into atoms. The hold magnetic field for this measurement was 546.2 ± 0.2 gauss. The solid line is the results of an exponential fit to the data. The fitted decay time is $220 \pm 7 \mu\text{s}$.

detect the molecules at high magnetic field using absorption imaging. Because the atoms and molecules can both absorb the same frequency imaging light, it was convenient to start with the atoms in a different Zeeman state. We then could use spin-selective absorption imaging to see the molecules directly.

4.4 Creating Molecules: New Techniques and Tools

To directly detect the molecules, we adopted a procedure similar to that used by the Hamburg group [63] and created the Feshbach molecules using radio-frequency (rf) oscillating magnetic fields. In this scheme, the ^{40}K atoms are prepared in a higher energy spin-state and driven to the Feshbach resonance state with an rf field. In the work by the Hamburg group the atoms were confined in a 3D optical lattice potential with precisely one atom pair per site. Confinement in an optical lattice has two advantages. First, the tight confinement of a pair of atoms in each lattice site meant that the initial motional state of each atom pair was the ground state of the trapping potential at that site. Magnetoassociation can then proceed by driving a transition between two well defined quantum states. Second, confinement of the atoms and molecules in the optical lattice protected the Feshbach molecules from collisions. This protection is important because the extremely weakly bound molecules can suffer heating and loss through inelastic collisions that cause vibrational quenching.

In our case, we created the fermionic heteronuclear $^{40}\text{K}^{87}\text{Rb}$ Feshbach molecules in a far-detuned optical dipole trap. In this relatively weak trap, the atoms start in a near-continuum of motional states, and furthermore, atoms and molecules are free to collide. Without using the confinement in an optical lattice, we found similar overall efficiency in the radio frequency (rf) association of ultracold heteronuclear molecules and created as many as 25,000 molecules at a temperature of about 300 nK. We studied the association process and measured the magnetic-

field dependent binding energy of the Feshbach molecules. Compared to previous results [63], we extended our measurements to magnetic fields much farther from the Feshbach resonance and calculated basic properties of the molecules such as their size and quantum state composition.

We extract the number and temperature of the atoms and molecules using time-of-flight, resonant absorption images. The gases are suddenly released from the optical trap and allowed to expand in the homogeneous magnetic field before imaging. Using a resonant light pulse of the appropriate frequency, we selectively image K or Rb atoms in a particular spin state at high magnetic field.

To create molecules, we utilize a Feshbach resonance between Rb $|1, 1\rangle$ and K $|9/2, -9/2\rangle$ atoms at $B_0 = 546.76$ G [64]. Similar to previous work using this resonance [63], we start with atoms at a magnetic field near the Feshbach resonance and apply a transverse rf magnetic field to convert atom pairs to molecules. However, unlike the work of ref. [63], in our experiment the atom pairs are not confined in an optical lattice. Therefore, the atoms are free to collide.

In Fig. 4.10 we show a typical rf association spectrum for a magnetic field tuned 0.7 G below the Feshbach resonance. The Rb and K atoms are initially prepared in the $|1, 1\rangle$ and $|9/2, -7/2\rangle$ states, respectively, and we apply an rf pulse with a frequency tuned near the atomic K Zeeman transition, $|9/2, -7/2\rangle \rightarrow |9/2, -9/2\rangle$. For these data we applied a gaussian rf pulse with a $600 \mu\text{s}$ $1/e^2$ full-width and an rf strength that can drive a $12 \mu\text{s}$ π -pulse on the atomic K Zeeman transition. The effect of the rf pulse is detected by counting the number of K atoms transferred to the previously unoccupied $|9/2, -9/2\rangle$ state. For this purpose, we implemented spin-state selective absorption imaging of the cloud in the optical trap at $B = 546$ G. We observe two peaks in the rf spectrum: one at the frequency of the atomic K Zeeman transition and one shifted to higher frequency. The higher frequency peak corresponds to a stimulated transition from a pair of

atoms into the Feshbach molecule state. The shift of this spectral feature from the atomic transition reveals the binding energy of the molecule. In comparing the widths of the two features it is important to note that the atom transition is power broadened by the rf pulse, which has a duration 50 times longer than the measured time for an atomic π -pulse. The smaller width of the molecule feature indicates that the coupling strength is much weaker for molecule association than for the atomic Zeeman transition. The full width at half maximum of the molecule feature is 7 kHz. This is consistent with the thermal distribution of the relative energies for atom pairs.

We are able to easily observe the molecular rf association feature because the Feshbach molecules can absorb the imaging light that is resonant with the K atom cycling transition at high magnetic field. Presumably, the first photon dissociates the weakly bound molecule and subsequent photons scatter off the resulting K atom. Compared to the case of homonuclear molecules, this direct imaging is possible for a larger range of Feshbach molecule binding energies. This is because the energy separation between the excited and ground electronic potentials varies relatively slowly with internuclear distance, R , since the heteronuclear excited and ground electronic potentials both vary as $1/R^6$. In contrast, for the homonuclear case, the excited electronic potential varies as $1/R^3$ and the ground potential varies as $1/R^6$.

4.5 Driving Bad Bound-Bound Transitions

After unambiguously creating and detecting KRb Feshbach molecules, we measured their lifetimes in the optical trap and discovered it was comparable to the 200 μ s we had measured previously using ramps. We began to suspect that the optical trap could be causing the short lifetime. To test this, we measured the molecule lifetime without the presence of the optical trap light. After creating

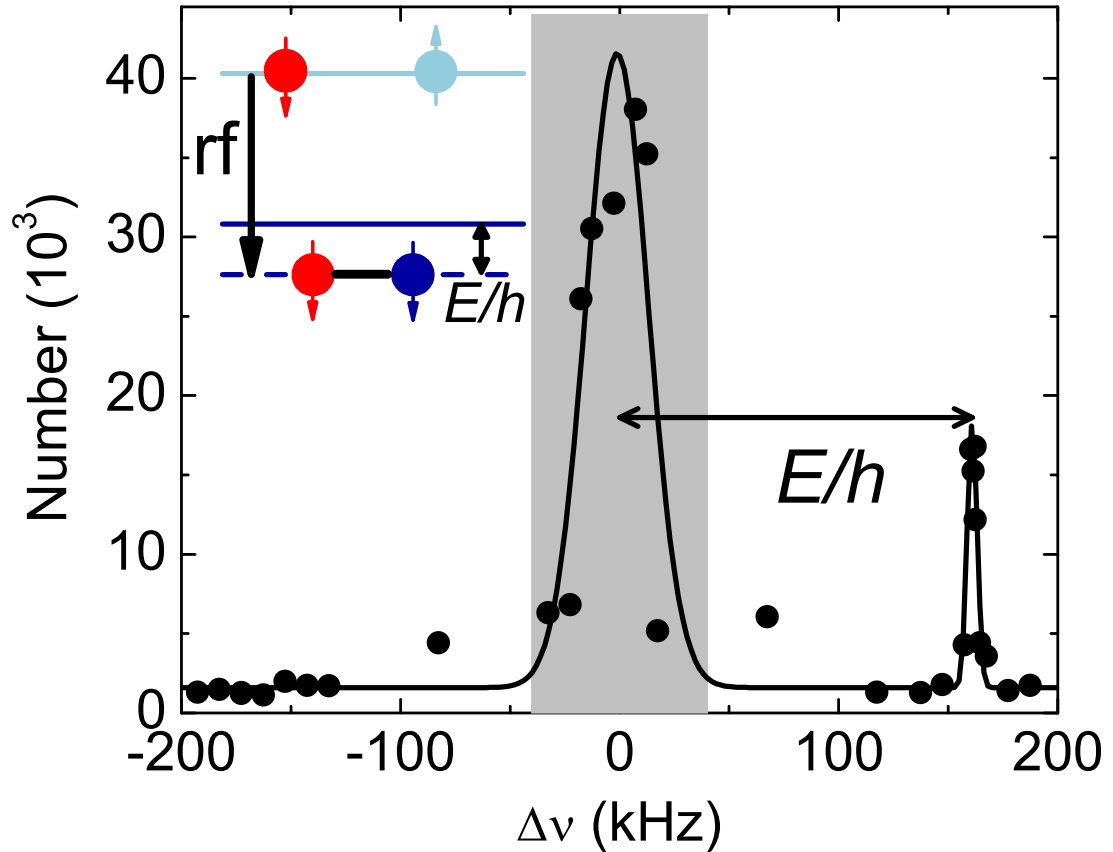


Figure 4.10: Rf association spectrum of heteronuclear Feshbach molecules at $B = 546.04$ G. The molecules are created starting from an ultracold gas of 1.7×10^5 ^{87}Rb atoms at $T/T_c = 1$ in thermal equilibrium with 8×10^4 ^{40}K atoms. The plot shows the detected atom/molecule number as a function of the detuning $\Delta\nu$ of the rf from the atomic resonance frequency. We observe a large atomic peak at zero detuning and a molecular peak at $E/h = 161$ kHz due to the association of atom pairs into the Feshbach molecule state. In this measurement the rf pulse duration was $600 \mu\text{s}$, which is 50 times longer than an atomic π -pulse. The grey band indicates the expected envelope full width at half maximum for the power broadened atomic transition. The inset shows a simplified energy diagram for magnetic fields below the Feshbach resonance. The upper solid line corresponds to Rb $|1, 1\rangle$ and K $|9/2, -7/2\rangle$, while the lower solid line corresponds to Rb $|1, 1\rangle$ and K $|9/2, -9/2\rangle$. The molecule state is represented by the dashed line. Depending on the detuning, the rf is capable of driving an atomic hyperfine changing transition or magnetoassociation. This data was taken while the atoms and molecules were held in an optical trap derived from a 1064 nm single-frequency fiber laser.

the molecules, the optical trap was turned off. We measured the molecule lifetime under these conditions and discovered it was longer than a few milliseconds. The longest lifetime that could be measured was limited by the expansion of the cloud. Since the expansion lowered the density, it is possible that density dependent collisional loss rates were also decreasing during the expansion. To check the effect of the optical trap light for a lower density cloud, we turned off the optical trap for a millisecond then turned the optical trap back on for the lifetime measurement. Again we found the lifetime was about 200 μs in the presence of the optical trapping light.

The optical trap light came from a multi-longitudinal mode, 1075nm fiber laser (model YLR-10-1075-LP from IPG photonics). We believe the laser was exciting the Feshbach molecules to the lowest vibrational states of the 3(1) excited state potential. This is shown in Fig. 4.11. As discussed in Chapter 6, we would later deliberately take advantage of this Feshbach enhancement for bound-bound transitions. To eliminate the limit to the molecule lifetime, we switched to using a single-longitudinal mode fiber laser operating at 1064 nm for the optical trap. This new laser did not excite molecules in the Feshbach state. However, since the long-term goal of this experiment is to create more deeply bound polar molecules, we note that a similar problem may exist for other, more deeply bound vibrational states of the ground-state potential.

4.6 Molecule Association Process

Because the atoms are free to move and collide in the trap, it is interesting to look at the time dependence of the rf association. The number of molecules observed as a function of the rf pulse duration is shown in Fig. 4.12. The gaussian $1/e^2$ width of the pulse is plotted on the horizontal axis. For these data, the peak rf strength is fixed and only the duration of the rf pulse is changed. The number

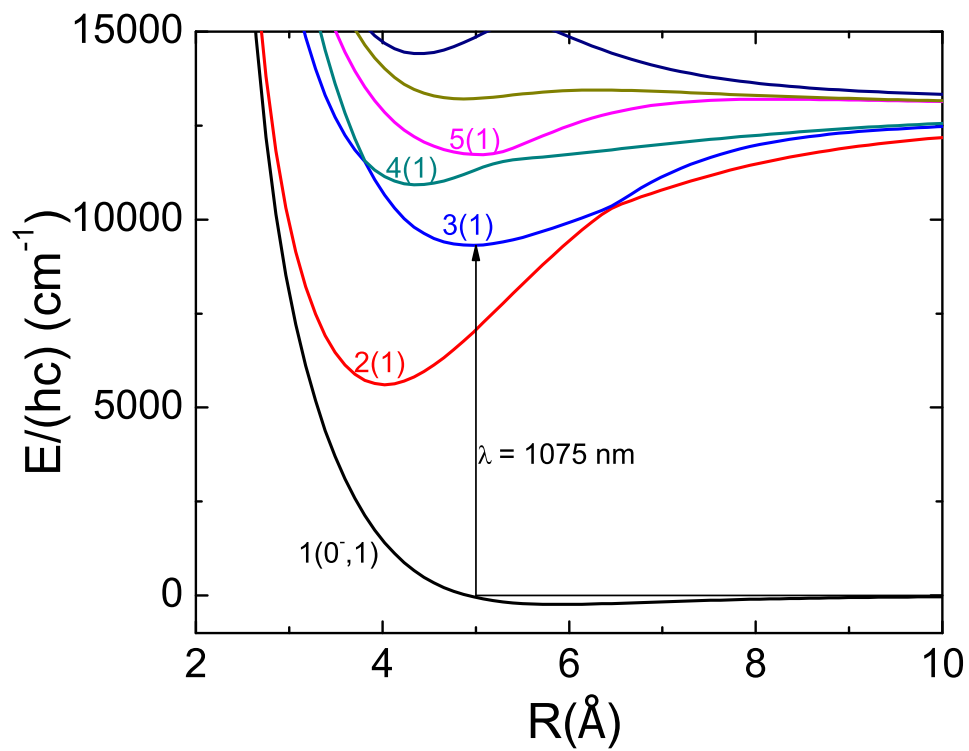


Figure 4.11: KRB molecular potentials. Svetlana Kotochigova has calculated that the 1075nm optical trap laser predominately drives bound-bound transitions from the Feshbach molecule state to vibrational states of either the 3(1) or 2(1) molecular potentials. The molecule potential energy data for this figure was obtained from Ref. [1].

of molecules increases rapidly for the first few hundred microseconds and then slowly decays. We do not observe Rabi oscillations. This is not surprising since we are driving transitions from a near continuum of free atom states to the bound molecule state. The observed decay results from atom-molecule collisions [36]. To estimate the effect of this decay on the maximum number of molecules created we fit the data to the product of a linear growth and an exponential decay (curve in Fig. 4.12). We find that the decay causes a 30% reduction in the maximum number of molecules created at the peak of the curve in Fig. 4.12. Since the maximum molecule creation in Fig. 4.12 corresponds to approximately 10% of the total number of K atoms, this raises the question of what limits the maximum conversion fraction?

Previous studies of molecule creation by slow magnetic-field sweeps across a Feshbach resonance have shown that the maximum conversion fraction depends on the phase space density of the atoms [48]. Not surprisingly, for a two-species atom gas mixture, the molecule conversion efficiency also depends on the spatial overlap of the two atom clouds [46]. We have measured the molecule conversion fraction as a function of temperature for Feshbach molecules produced using rf association at $B=546.17$ G. For this measurement, the gas mixture was initially cooled to a temperature below the critical temperature, T_c , for the onset of Bose-Einstein condensation of the Rb gas. The temperature is then varied simply by waiting a variable amount of time in a sufficiently deep trap and letting the gas slowly heat up before creating Feshbach molecules. With this technique, the number of Rb and K atoms is kept nearly constant. To create Feshbach molecules we use rf adiabatic rapid passage and sweep the rf frequency from 80.132 MHz to 80.142 MHz in 2 ms. The results are shown in Fig. 4.13.

We found that the maximum conversion fraction occurs at $T/T_c \approx 1$. Here, 25% of the K atoms are converted to molecules; this corresponds to 25,000

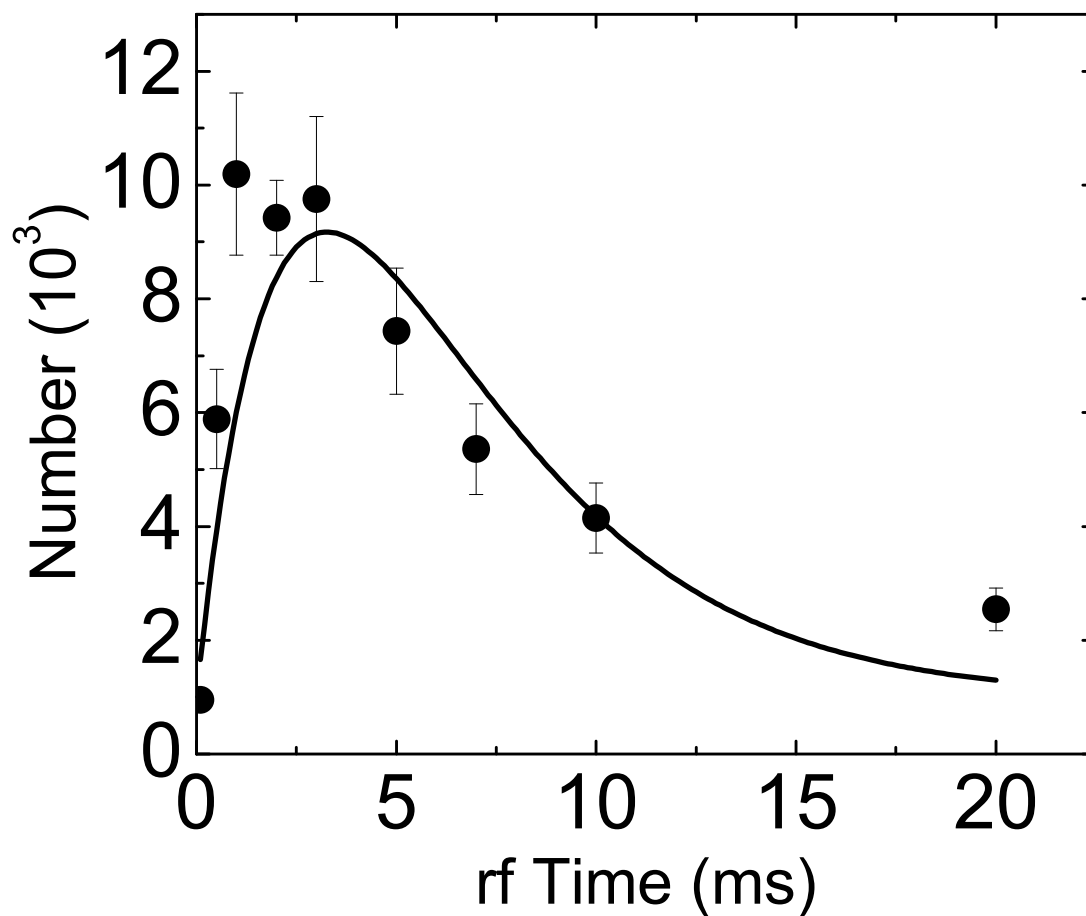


Figure 4.12: Time dependence of the rf association process at $B = 546.17$ G, where the measured molecule binding energy is $E/h = 96$ kHz. The plot shows the measured number of molecules created as a function of the $1/e^2$ gaussian rf pulse length. The solid line is a simple fit used to estimate the impact of the observed decay on the maximum number of molecules created.

molecules. It is interesting to compare the measured conversion fraction for rf association to the prediction of a phenomenological model introduced in ref. [48]. This model, using experimentally determined parameters, has been successful in predicting the molecule conversion efficiency for Feshbach molecules created by slow magnetic-field sweeps and slow magnetic-field oscillations [48, 46], but has not previously been compared to data for rf association. Following the procedure outlined in [48], Michele Olson calculated the predicted maximum conversion efficiency using realistic trap potentials and distributions of our atomic clouds. The curves in Fig. 4.13 show the results of the calculation, multiplied by 0.70 to approximately include the effect of the molecule loss seen in Fig. 4.12. The dashed curves represent the uncertainty in the conversion fraction due to the uncertainty in the trap frequencies and atom numbers. The agreement between the model for association by slow magnetic-field sweeps and the data for rf association is quite good. The predicted dependence on temperature agrees with our experimental results for rf association. The peak in the molecule conversion fraction as a function of T/T_c can be understood as a balance between two factors: phase-space density and the spatial overlap of the two clouds. As T/T_c decreases, the phase-space density increases but, below $T/T_c = 1$, the onset of Rb BEC reduces the spatial overlap of the Rb cloud with the K cloud. The effect of gravitational sag also reduces the spatial overlap of the two clouds and at $T/T_c = 1$ the model predicts a 30% reduction in molecule conversion efficiency when compared to the case with no gravitational sag.

4.7 Ultracold, Trapped Molecules

A feature of using rf association to create heteronuclear Feshbach molecules is that we can selectively image the Feshbach molecules using light resonant with the appropriate K atom spin-state. The upper part of Fig. 4.14 shows the radial

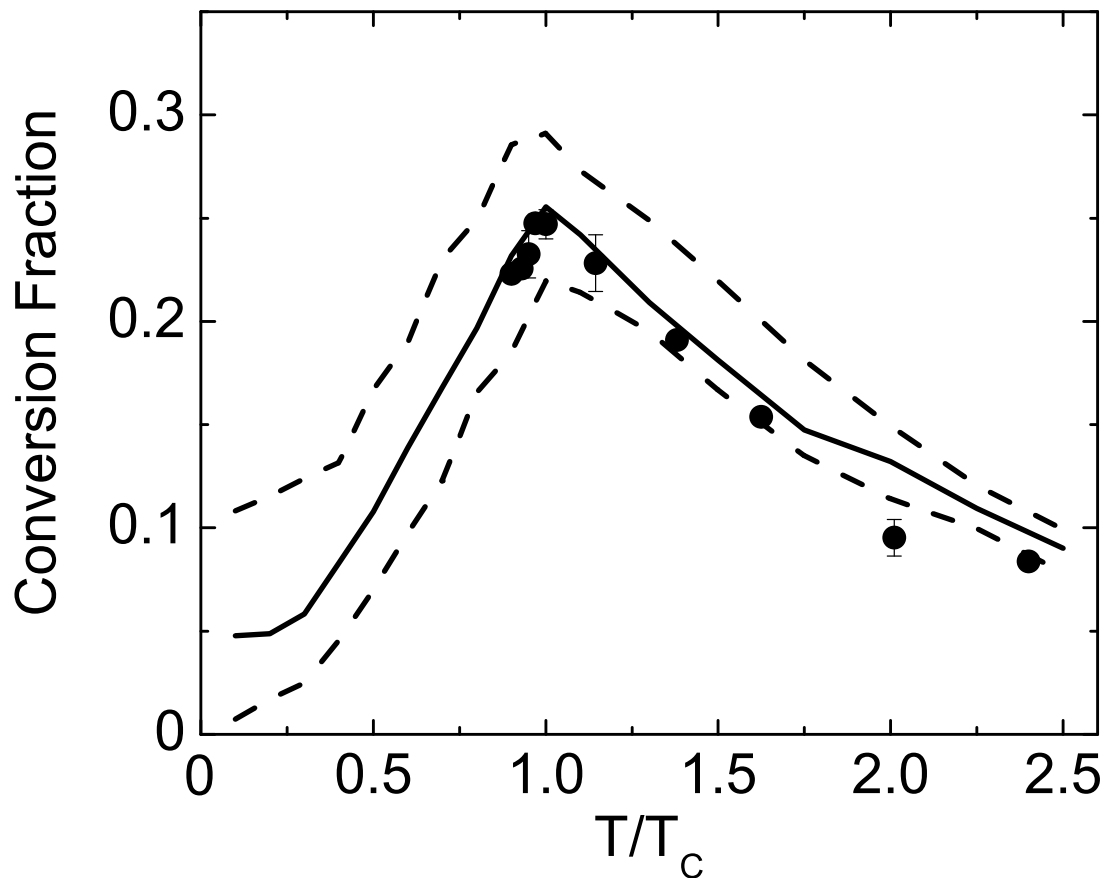


Figure 4.13: Temperature dependence of Feshbach molecule creation by rf association. Plotted is the molecule conversion fraction N_m/N_K as a function of T/T_c for the Rb atoms. The solid circles (\bullet) are experimental data and the curves are results of a Monte Carlo calculation. The dashed curves represent the uncertainty in the conversion fraction taking into account the uncertainty in the trap frequencies and atom numbers. The molecules are created starting from an atom gas mixture with $N_{\text{Rb}} = 3 \times 10^5$ and $N_K = 1 \times 10^5$. We observe maximum conversion efficiency of 25% at $T/T_c = 1$.

root-mean-squared size, σ_{RMS} , of the molecular gas as a function of expansion time after the optical trap is abruptly turned off. We fit the size to $\sigma_{RMS}(t) = (1/\omega_r)\sqrt{k_B T/m_{\text{KRb}}}\sqrt{1 + \omega_r^2 t^2}$ and obtain an expansion energy of $T = 310 \pm 20$ nK. Here, T is the only fit parameter, k_B is Boltzmann's constant, m_{KRb} is the mass of the KRb molecule, and ω_r is the radial angular trapping frequency for the molecule.

To confirm that the KRb molecules are trapped, we can look for sloshing of the molecule cloud after a perturbation to the trap potential. The lower part of Fig. 4.14 shows the position of the molecule cloud along a radial direction as a function of time after the optical trap was abruptly shut off for 1 ms and then turned back on. A fit to a damped sine wave (solid curve in the lower part of Fig. 4.14) gives a radial slosh frequency of 174 ± 3 Hz. To reduce collisional loss of the molecules, these data were taken after removing Rb atoms from the trap [36]. For comparison, using the same trapping fields, the measured frequencies for Rb and K atoms are 136 ± 2 Hz and 211 ± 4 Hz, respectively. The trapping frequency of the far-off-resonance optical dipole trap depends on the mass of the particle and its polarizability. Within the measurement uncertainties, the ratios of the Rb atom, K atom, and KRb Feshbach molecule trap frequencies are consistent with the weakly bound molecule having a mass equal to the sum of the atomic masses and a polarizability equal to the sum of the atomic polarizabilities, which is a reasonable assumption for these weakly bound molecules.

4.8 Binding Energy of the Feshbach Molecules

Rf association spectra, such as the one shown in Fig. 4.10, can be used to determine the binding energy of the molecules. We take the rf frequency at the peak of the molecule association feature and subtract the rf frequency of the atomic Zeeman transition to get a measure of the binding energy. The measured

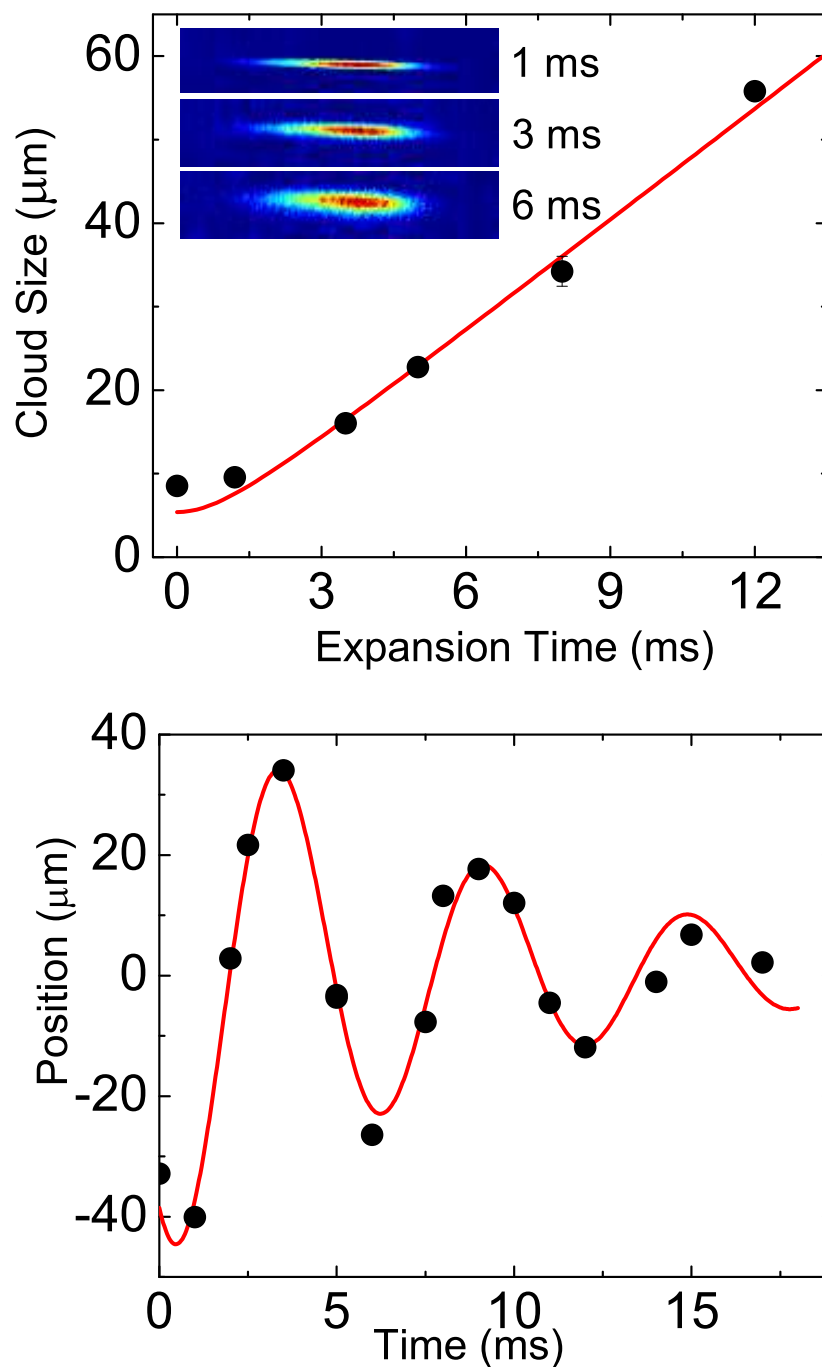


Figure 4.14: (Top inset) Images of the molecule cloud after release from the optical trap. (Top) Radial cloud size for the molecules after release from the optical trap. (Bottom) Splotch of the molecular cloud in the optical trap seen in images of the expanded gas. The expansion time was 3 ms. The observed oscillation in the molecule cloud's position demonstrates that the molecules are indeed trapped. The strong damping seen here is most likely due to anharmonicity of the optical trap.

binding energy can have a systematic shift because the initial atom pairs have a range of relative kinetic energies. We estimate that our measured binding energy could be systematically high by $0.6k_B T/h \approx 4$ kHz [61], where h is the Planck constant. For binding energies larger than about 0.5 MHz, the molecules are no longer resonant with the imaging light and we are no longer able to see the rf association feature by directly imaging the molecules. However, we can still detect molecule creation by measuring the loss of K atoms from the $|9/2, -7/2\rangle$ state. As the magnetic-field detuning from the Feshbach resonance increases, we also find that the maximum conversion fraction decreases, and a longer (as long as 20 s) rf pulse is required.

Figure 4.15 shows the measured molecule binding energy as a function of the magnetic field. We plot the negative of the molecule binding energy, $-E/h$, to indicate that the molecule is bound below the atomic Rb $|1, 1\rangle + \text{K } |9/2, -9/2\rangle$ threshold. We observe a quadratic dependence of the binding energy at magnetic fields near the resonance. However, far from the resonance, the binding energy becomes linear with magnetic field. The data in Fig. 4.15 are compared with two theoretical curves. The dashed black line shows the expected universal behavior very near the resonance [2, 70]. Here, the binding energy is given by $E = \hbar^2/(2\mu_{KRb}(a - \bar{a})^2)$, where a is the s-wave scattering length, μ_{KRb} is the ^{40}K and ^{87}Rb reduced mass, and $\bar{a} = 68.8 a_0$ is the mean scattering length determined by the long-range behavior of the potential [2] and a_0 is the Bohr radius. Near a Feshbach resonance, the scattering length is given by $a = a_{bg}(1 - w/(B - B_0))$ [71, 72], where $a_{bg} = -185a_0$ and $w = -2.9$ G for this resonance [65]. To calculate the molecule binding energy farther from the resonance, our collaborator, Paul Julienne, performed a multiple-channel calculation. The calculated magnetic-field location of the Feshbach resonance did not exactly match with our data. We therefore fit the experimental data using the coupled-channel calculation and one free

parameter, which is the Feshbach resonance position, B_0 . From this fit, we obtain $B_0 = 546.76 \pm 0.05$ G. We find excellent agreement between the data and the coupled-channel calculation (solid line in Fig. 4.15). This measurement of the resonance position disagrees with our previous measurements shown in Fig. 4.7 by nearly 0.3 G. The discrepancy could result from the relatively high atomic densities that could cause systematic shifts of the measured resonance location. See Sec. 4.2 for more details of the earlier measurement.

To provide a larger view of the Feshbach molecule state that we probe in the experiment, we show the results of Paul Julienne’s coupled-channel calculation for a much wider range of magnetic fields in Fig. 4.16. A Feshbach resonance occurs because of coupling between an atom scattering state and an energetically closed bound state. The channels used in the calculation are those having a total spin projection quantum number $M_F = m_f^{Rb} + m_f^K = -7/2$ and are therefore coupled to free atoms in the $|9/2, -9/2\rangle$ and $|1, 1\rangle$ states for K and Rb, respectively. For the s-wave Feshbach resonance at $B_0 = 546.76$ G, the dominant closed channel contribution comes from the K $|7/2, -7/2\rangle +$ Rb $|1, 0\rangle$ channel with vibrational quantum number corresponding to the second level below the dissociation limit in this channel.

We have seen that we can efficiently create heteronuclear Feshbach molecules starting from an ultracold gas of ^{40}K and ^{87}Rb atoms. This could provide a starting point for future experimental efforts aimed at creating polar molecules. Transfer of the Feshbach molecules to more deeply bound states could proceed using light or microwave fields. Therefore, it is useful to consider how basic properties of the Feshbach molecules, such as their typical size and their hyperfine character, depend on the magnetic-field detuning from the resonance. We can estimate properties of the molecules from the measured binding energy curve shown in Fig. 4.15.

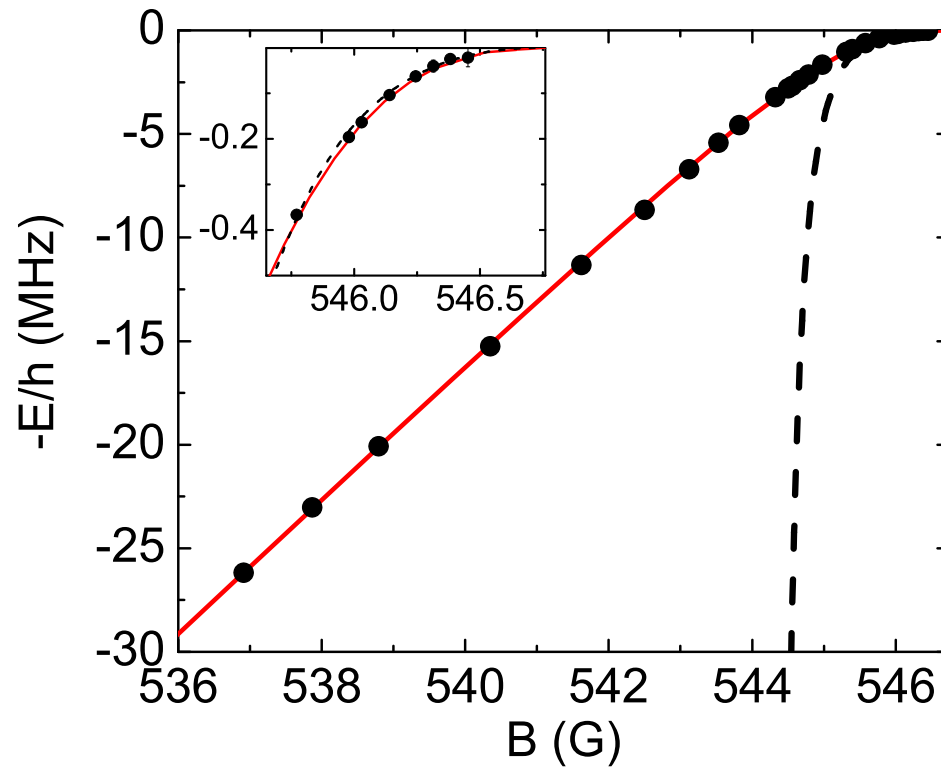


Figure 4.15: Energy of the heteronuclear Feshbach molecules, relative to the Rb $|1, 1\rangle + \text{K } |9/2, -9/2\rangle$ atomic threshold, plotted as a function of magnetic field. The data (solid circles) agree well with our calculation based on a full coupled-channel theory (solid line). Near the Feshbach resonance one expects a universal relationship between the s-wave scattering length and the binding energy. The black, dashed line shows the predicted binding energy using the universal prediction [2]. Inset: Same as the main plot but looking at the region close to the Feshbach resonance.

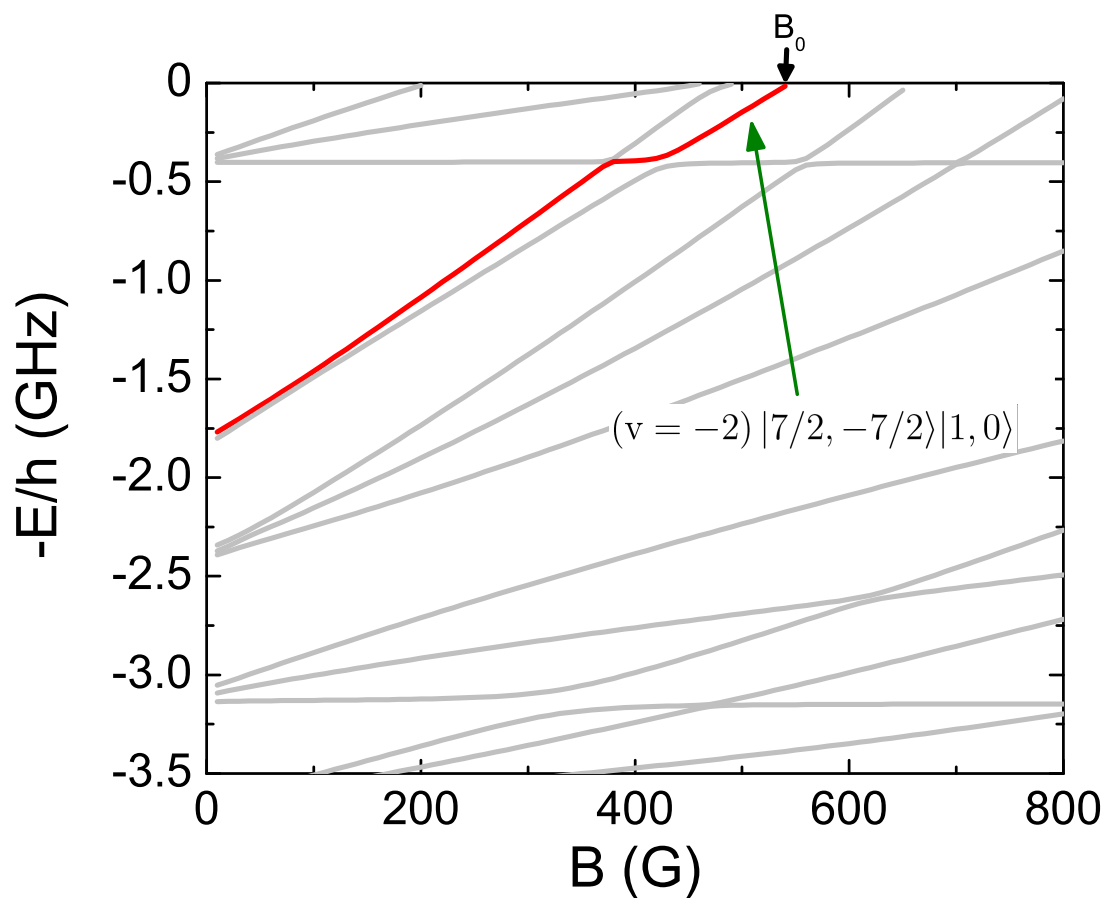


Figure 4.16: Calculated molecule energies near the K $|9/2, -9/2\rangle + \text{Rb } |1, 1\rangle$ atomic threshold. All levels have total spin projection quantum number $M_F = -7/2$. The level energies are calculated using a full coupled-channel calculation and have been scaled so that the zero in energy is the K $|9/2, -9/2\rangle + \text{Rb } |1, 1\rangle$ atomic threshold. The bold line is the adiabatic level associated with the 546.7 G Feshbach resonance.

4.9 Properties of the Feshbach Molecule

The properties of the Feshbach molecule, including its size, are determined by both the open channel and the dominant closed channel. The bare states associated with these channels have different magnetic moments, and this is, of course, why the molecule's binding energy is magnetic-field tunable. The open and closed channel contributions to the actual dressed-state molecule can then be determined from the molecule's magnetic moment relative to the open channel, which is simply the numerical derivative, $\frac{dE}{dB}$, of the measured binding energy shown in Fig. 4.15. Explicitly, we find the closed channel fraction, f_c , from the following equation: $f_c = \frac{1}{\Delta\mu} \frac{dE}{dB}$. Here, $\Delta\mu = 2.38 \times \mu_B$ is the difference of the atomic magnetic moments of the bare closed and open channels at a magnetic field near the Feshbach resonance and μ_B is the Bohr magneton. The closed channel fraction as a function of the magnetic field is shown in the inset of Fig. 4.17. For magnetic fields more than 2 G below the Feshbach resonance, we find that $f_c > 0.5$ indicating that molecule is predominantly closed channel in character.

We can also estimate the molecule size as a function of magnetic field, B . Near the resonance, where a is large, the molecule size is $r_{mol} = a/2$. However, far below the resonance, the molecule becomes dominated by the closed channel and the molecule size approaches that of the closed channel molecule. To capture this behavior, we use a simple estimate of the molecule size given by a weighted average of the closed and open channel sizes, r_c and r_o .

$$r_{mol} = f_c \times r_c + (1 - f_c) \times r_o. \quad (4.1)$$

r_c and r_o are calculated using a single-channel model incorporating the correct long-range behavior of the interatomic potential. Figure 4.17 shows our estimate of the size, r_{mol} , as a function of magnetic field near the Feshbach resonance.

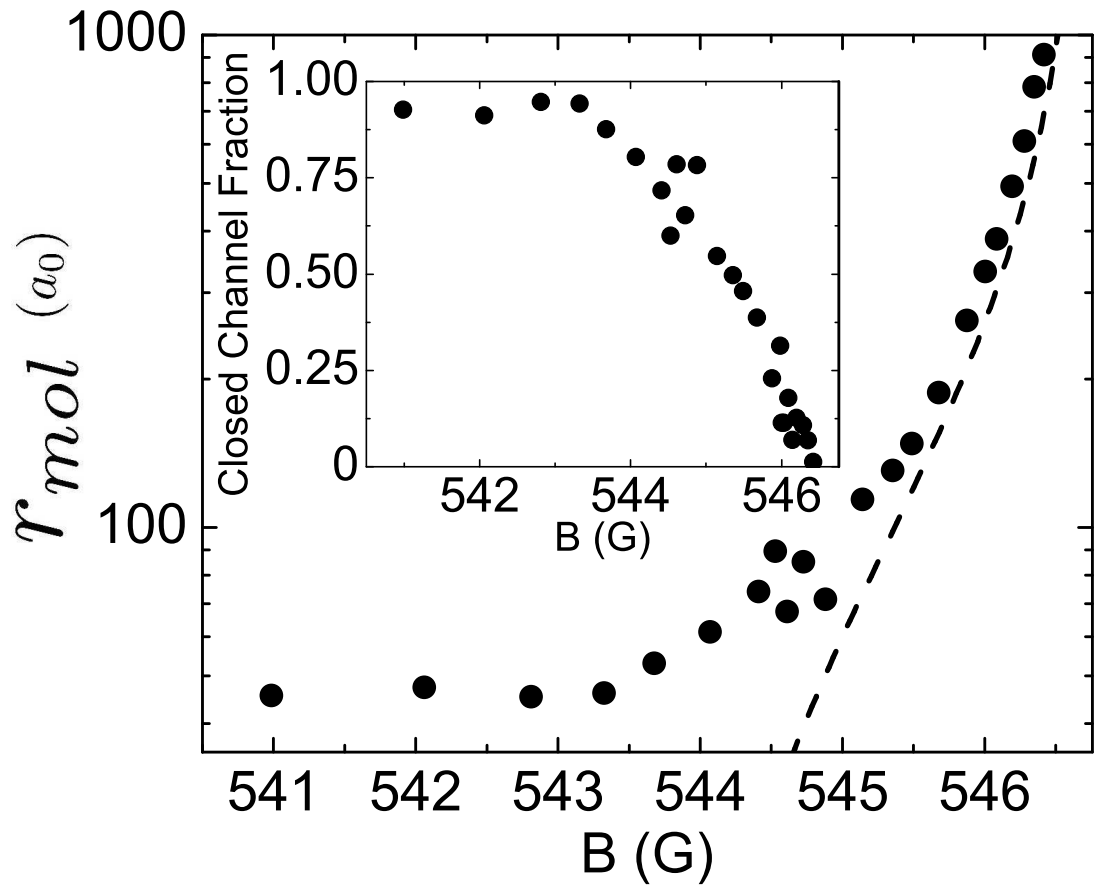


Figure 4.17: Estimated molecule size vs. magnetic field near the Feshbach resonance as extracted from the experimentally measured binding energy (\bullet). We compare to the universal size prediction, $a/2$ (dashed line). Inset: Closed channel fraction extracted from the experimentally measured binding energy (\bullet)(see Sec. 4.9).

To estimate r_c and r_o , we numerically solve the Schrödinger equation. Since the loosely bound vibrational wavefunctions have large amplitudes at large internuclear separation, it is important that our model internuclear potential has the correct long-range form. The short-range details of the potential are not as critical and simply contribute to the overall phase of the wavefunction. To simplify the calculation, we follow an approximation given by Gribakin and Flambaum [2] and use a model internuclear potential that incorporates the correct long-range behavior and has an impenetrable hard core with a radius R_0

$$U(r) = \begin{cases} \infty & r < R_0 \\ -\left(\frac{C_6}{r^6} + \frac{C_8}{r^8} + \frac{C_{10}}{r^{10}}\right) & r \geq R_0. \end{cases} \quad (4.2)$$

For C_6 , C_8 , and C_{10} we use the values reported by Pashov *et al.* [73]. R_0 controls the location of the bound states in the potential and the scattering length. Since this potential is a single-channel approximation to a multichannel potential, the value of R_0 is chosen to be large to avoid the significant divergence between the singlet and triplet potentials that occurs at small internuclear separation. However, R_0 must be small enough so the potential has an adequate number of bound states. For $R_0 \approx 22 a_0$ both criteria are satisfied.

Before calculating the size of the closed channel molecule, we first fine-tune R_0 so that the calculated background scattering length agrees with the known ^{40}K ^{87}Rb s-wave scattering length, $a_{bg} = -185 a_0$. We note that this procedure yields binding energies of the last three vibrational states that agree to within 7% with energies obtained using a much more accurate, multichannel potential. The second-to-last vibrational state with binding energy $E_{-2} \approx h \times 3.2 \text{ GHz}$ is responsible for the $B = 546.7 \text{ G}$ Feshbach resonance. We, therefore, use its wavefunction to calculate the closed-channel size, $r_c = \langle r \rangle \approx 40 a_0$.

Using a similar procedure, we calculate the open-channel size, r_o , which

depends on the magnetic field detuning from the Feshbach resonance. In this case, however, we vary R_0 to control the binding energy, E , of the weakest bound molecular state. For each E , we calculate the size, $r_o = \langle r \rangle$, from the calculated molecular wavefunction. For the smallest binding energies, the calculated size agrees with the universal prediction. At larger binding energies the molecular size is approximately the classical turning point. Figure 4.18 shows the behavior of r_o .

4.10 Conclusions

In conclusion, we have used rf association to create heteronuclear Feshbach molecules from an ultracold gas of ^{40}K and ^{87}Rb atoms confined in an optical dipole trap. Unlike previous work [63], we do not isolate pairs of atoms in individual wells of a deep optical lattice potential. Consequently, the atoms and the molecules are free to collide and pairs of atoms are initially in a near-continuum of motional quantum states. Nevertheless, by optimizing the pulse duration and frequency of the rf, as well as the initial atom gas temperature, we achieve comparable overall efficiency in converting atoms to weakly bound Feshbach molecules. We also demonstrate that these molecules are ultracold and trapped.

A gas of ultracold, heteronuclear Feshbach molecules can provide a starting point for optical manipulation to create a sample of ultracold polar molecules. In anticipation of such experiments, we have measured the magnetic-field dependent binding energy of the Feshbach molecules. We extend these measurements to magnetic fields much farther from resonance than what is typically of interest for ultracold atom experiments. We measure binding energies as large as 26 MHz and find that for magnetic fields more than 2 or 3 G detuned from resonance, the binding energy curve is linear. This means that by lowering the magnetic field to a few gauss below the resonance, one can have Feshbach molecules that are predominantly closed channel in character with the corresponding molecular size.

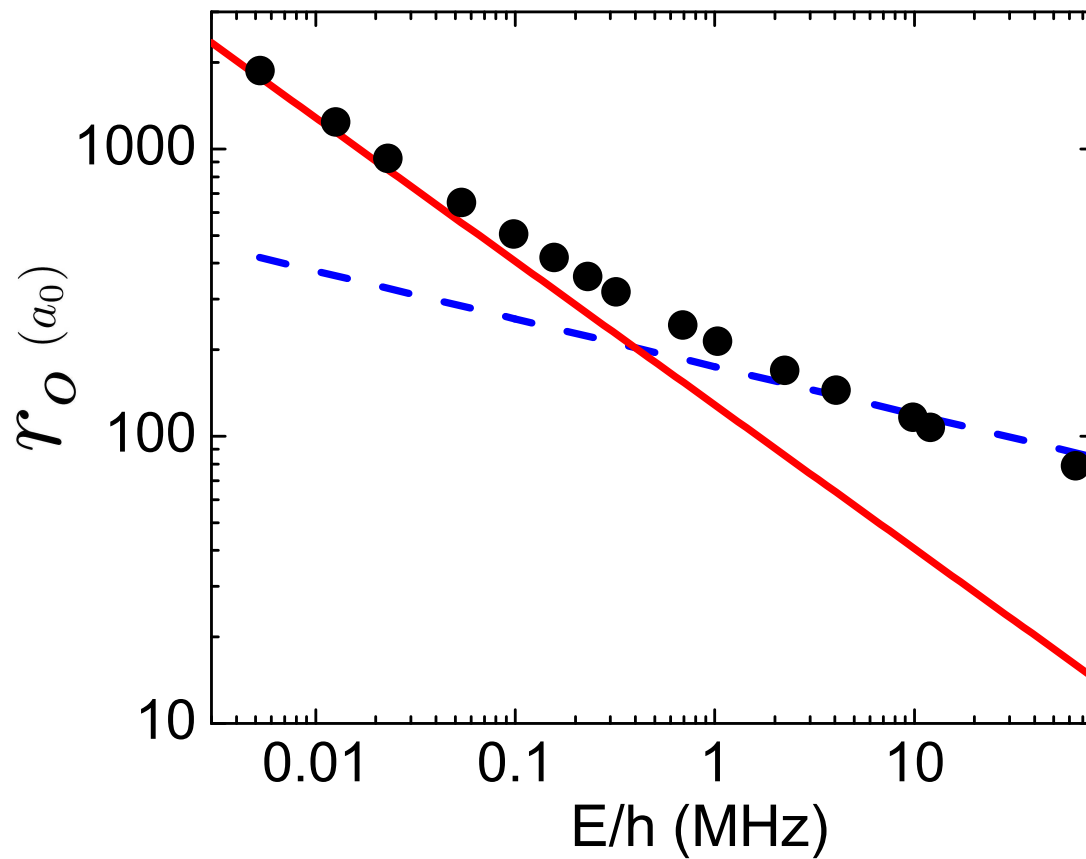


Figure 4.18: The calculated open-channel molecular size, r_o , as a function of binding energy. The solid red line is the universal prediction, $a/2$. The dashed blue line is the classical outer turning point of the KRb ground state potential.

This is important to improve the Franck-Condon overlap with other molecular states. Improved Franck-Condon overlap will increase the transfer efficiency to these other states.

Although the rf association technique was a useful tool for directly detecting the molecules and diagnosing problems with our apparatus, we no longer use rf association to form Feshbach molecules. The rf causes offset errors in our control electronics for the magnetic field so we have found that it is more convenient and stable to form the molecules using magnetic field sweeps across the resonance.

Chapter 5

Inelastic decay of the molecules

5.1 Introduction

In this chapter, I will present our study of inelastic collisions starting from a Bose-Fermi mixture of atoms near a heteronuclear Feshbach resonance. Using the magnetic-field controlled Feshbach resonance, we created ultracold heteronuclear molecules and studied their inelastic decay. We found that the dominating decay process arises from atom-molecule collisions and observed the effect of both fermionic suppression and bosonic enhancement on the inelastic collisions. The effects of quantum statistics arise because of indistinguishability of the colliding atom and one of the constituents of the molecule. With appropriate atomic collision partners, we observe molecular lifetimes as long as 100 ms. For large scattering length, a , experimental data are compared to theoretical predictions based on a numerical solution of the three-body Schrödinger equation [74].

As mentioned previously, Feshbach molecules are atoms that are weakly bound to one another [19]. These molecules have a large amount of vibrational energy that can be released through collisions with atoms and molecules in a process known as vibrational quenching. Often, this process leads to heating and loss of the atomic and molecular clouds. In most previous experiments using ultracold atoms to create Feshbach molecules the molecules are composite bosons. These studies are particularly interesting when the original atoms are fermions. In

this case, the vibrational quenching of the bosonic molecules is strongly suppressed due to Fermi statistics [67]. In contrast, when bosonic molecules are created from an atomic Bose gas, this suppression is not present and the molecules tend to have much shorter lifetimes [75]

5.2 Collisional Stability of Fermionic Feshbach Molecules

Understanding the loss mechanisms in Bose-Fermi mixtures near heteronuclear Feshbach resonances is essential for experiments attempting to explore interesting many-body effects in these systems [76]. Moreover, understanding and controlling these collisional loss processes is important for proposed experiments using heteronuclear Feshbach molecules as the starting point for the creation of ultracold polar molecules (see [77] and references therein).

For the experiments discussed in this chapter, we prepared a mixture of ultracold ^{40}K and ^{87}Rb held in an optical trap at the end of evaporative cooling. The mixture had 3×10^5 Rb at $T/T_c \sim 1$ and 1×10^5 K at $T/T_F \sim 0.6$ in the optical trap. The atoms are then converted into molecules using rf association as described in Chapter 4. The molecules are imaged in absorption using light resonant with the K $S|9/2, -9/2\rangle \rightarrow P|11/2, -11/2\rangle$ cycling transition at high magnetic field [63]. We measure the lifetime of the molecules in the weakly bound Feshbach state. We characterize the decay of the cloud by its $1/e$ lifetime, τ , and introduce a loss coefficient, β , which characterizes the strength of vibrational relaxation. This coefficient is related to τ by $\beta = \frac{1}{n_A \tau}$, where n_A is the initial average density of the dominant atomic collision partner, $n_A = \frac{1}{N} \int n(\mathbf{r})^2 d^3r$.

For Feshbach molecules, β will, in general, depend on the magnetic-field detuning from the Feshbach resonance, $B - B_0$. This detuning is related to the heteronuclear scattering length, which is given by $a = a_{bg}(1 - \frac{W}{B - B_0})$. The background scattering length is $a_{bg} = -185 a_0$, where a_0 is the Bohr radius, and the

Collision partners	Expected dependence for $a > 0$
X+BF	$\beta(a) \propto a^{-1}$ [78]
B+BF	$\beta(a) \propto P(a) \times a$ [79, 80, 81]
F+BF	$\beta(a) \propto a^{-3.12}$ [79, 80]
B+B+F	$K_3(a) \propto M(a) \times a^4$ [79, 80]

Table 5.1: Scattering length, a , dependence of the loss coefficient for various collision partners. ‘BF’ refers to the Feshbach molecule, ‘B’ to the boson, ‘F’ to the fermion, and ‘X’ to a distinguishable K atom. $P(a)$ and $M(a)$ are log periodic functions in a with modulations resulting from the formation of Efimov states.

width of the resonance is $W = -2.9$ G [65]. In the limit of zero temperature and large a ($a \gg r_{\text{vdW}}$, where $r_{\text{vdW}} = 72a_0$ is the van der Waals length [19]), β is predicted to have a universal power law dependence on a [79, 80]. The power laws are strongly dependent on the quantum statistics of particular collision partners (see Table 5.1). While our measurements are not fully in the limit of $T = 0$ and large a , we are able to observe the strong influence of the quantum statistics of the particles involved in an inelastic atom-molecule collision. For large a , we compare our experimental data with finite temperature numerical calculations. Our theory collaborator, Jose D’Incao, has performed these calculations by solving the Schrödinger equation in the hyperspherical adiabatic representation [74]. He assumed a simple finite range potential model for the interatomic potentials $v(r) = -D \text{sech}^2(r/r_{\text{vdW}})$, where r is the interatomic distance and D is adjusted to produce the desired scattering length variations. We limit our comparison between experiment and theory to a scattering length regime where the finite-range model can reproduce experimentally observed binding energies to within 20%. The cut-off occurs at $a = 700 a_0$. For each comparison with the experimental data the numerically calculated inelastic rate is scaled by a multiplicative factor. At finite temperature ($T \approx 150$ nK) there is collisional dissociation when the binding energy of the molecules is comparable to the collision energy, ($a \gtrsim 4500 a_0$)

[82, 79, 80]. We, therefore, restrict our measurements in a regime where collisional dissociation is not a problem.

5.3 Isolating Collision Partners

5.3.1 Distinguishable Atoms

In measuring the loss rate β , ideally one would like to isolate a particular inelastic collisional process. Experimentally, we control the internal states of the Rb and K atoms using applied rf fields. Combining this rf control with resonant light pulses, we are able to control the atom densities through selective removal from the trap. We first consider the case of distinguishable atoms colliding with molecules, where the quantum statistics of the colliding particles is not important. The distinguishable atom is chosen to be K in the $|9/2, -7/2\rangle$ state because it is easily accessed experimentally. The small Zeeman energy of this state causes it to be stable against inelastic two-body collisions with either K $|9/2, -9/2\rangle$ or Rb $|1, 1\rangle$ atoms. A nearly pure mixture of K $|9/2, -7/2\rangle$ atoms and Feshbach molecules is prepared by removing excess Rb atoms from the trap after creating molecules. Using a combination of microwaves to drive Rb atoms to the $|2, 2\rangle$ state and resonant light on the cycling transition, we remove 99% of the Rb atoms and leave the K $|9/2, -7/2\rangle$ atoms and molecules essentially unperturbed.

Figure 5.1 shows a plot of experimentally measured β as a function of the heteronuclear scattering length along with numerical calculations for this case. As predicted [78], the loss rate, β , decreases near the Feshbach resonance (increasing a). Even though the quantum statistics for this case is not important, β is expected to be suppressed as a^{-1} as a result of the repulsive character of the effective atom-molecule interaction. The suppression for smaller scattering lengths, but reasonably large molecule sizes, can be qualitatively explained by an intu-

itive argument involving poor wavefunction overlap with deeply bound molecular states. For our smallest scattering lengths, we find that β stops changing with decreasing a . Here, the universal prediction for the Feshbach molecule size, $a/2$, is no longer valid. To account for this effect we can instead plot β versus an improved estimate of the molecular size, $\langle r_{mol} \rangle$, which takes into account both closed and open channel contributions [3]. The calculation of the molecule size is discussed in Chapter 4. Fitting the data in Fig. 5.1 (inset) we find a power law of -0.97 ± 0.16 .

5.3.2 Bosonic Atoms

Next, we present measurements of molecule collisions with bosonic atoms. Here we measure the inelastic decay rates of Feshbach molecules when both Rb $|1, 1\rangle$ atoms and K $|9/2, -7/2\rangle$ atoms are present. The data was taken with the Rb density more than a factor of three larger than the K density. The contribution of collisions with distinguishable K is known (Fig. 5.1) and subtracted from the data to extract the loss coefficient, β , for collisions with Rb only.

Figure 5.2 shows a plot of β as a function of the heteronuclear scattering length, a . For large a , $a \gtrsim 1000 a_0$, we observe a distinct enhancement of β that increases with increasing a . This agrees with the expectation that Bose statistics should enhance the molecule decay rates due to the attractive character of the effective atom-molecule interaction [79, 80]. In addition, Efimov three-body bound states might induce enhanced resonant losses due to trimer formation [83, 82]. The present data do not rule out Efimov states. However, we also do not observe a clear signature of Efimov states for the range of scattering lengths and temperatures carried out in this work.

The measured molecular loss coefficients increase for decreasing a for $a \lesssim 1000 a_0$. This trend is reminiscent of collisions with distinguishable atoms. One

possible explanation is that the increasing closed channel fraction of the Feshbach molecule far from resonance makes the colliding free atom effectively distinguishable from the molecule's constituent atoms, and hence decreases the influence of bosonic enhancement.

5.3.3 Fermionic Atoms

To study collisions between molecules and fermionic atoms, we prepare a nearly pure mixture of K $|9/2, -9/2\rangle$ atoms and Feshbach molecules using the following procedure: after creation of the molecules, we remove Rb atoms from the trap and drive the remaining K atoms to the $|9/2, -9/2\rangle$ state with an rf π -pulse on the atomic transition. This rf pulse does not affect the molecules since its frequency is detuned by about five linewidths. After waiting a variable time for the molecule decay measurement, we drive the K atoms back into the dark $|9/2, -7/2\rangle$ state and image the remaining molecules.

Experimental results are shown in Figure 5.3. These data agree with the theoretical expectation that the decay is suppressed with increasing a . For our measurements at finite a , we observe β scaling as $a^{-1.6\pm 0.2}$. This trend qualitatively agrees with numerical calculations (solid curve in Fig. 5.3). The suppression of molecular decay allows for molecule lifetimes as long as 100 ms near the resonance (see inset of Fig. 5.3). We note that the calculated β eventually scales as $a^{-3.12}$ for larger a [79, 80].

For the fermionic case (Fig. 5.3), we observe a suppression of β_{F+BF} when compared to the decay rates due to collisions with distinguishable atoms (Fig. 5.1). In contrast, for the bosonic case (Fig. 5.2), we observe β_{B+BF} to be larger than the distinguishable atom case near the resonance. The generality of this behavior is an open question because β depends on short-range physics that will be different in other systems.

Molecule-molecule collisions might also contribute to the inelastic loss of molecules, but these are expected to be suppressed due to the fermionic character of the KRb molecules. In the analysis, we have assumed no molecular decay due to molecule-molecule collisions. From our longest molecule lifetimes, an upper limit on the molecule-molecule loss coefficient at a scattering length of $a = 1500 a_0$ is $\beta_{BF+BF} \leq 4 \times 10^{-11} \text{cm}^3/\text{s}$.

5.4 Three-Body Recombination

We also measured three-body recombination rates for atoms in a Bose-Fermi mixture near a heteronuclear Feshbach resonance. We extracted the three-body loss coefficient, K_3 , by analyzing measurements of the time-dependent loss of the atomic species as a function of a on both sides of the resonance (Fig. 5.4). Note that finite temperature will result in a saturation of the collisional decay with increasing scattering length. We find that near the Feshbach resonance, the loss rate K_3 is enhanced by many orders of magnitude. It follows the expected power law dependence $K_3 \propto |a|^4$ [79, 80] before saturating near the resonance due to the onset of unitarity for scattering lengths $|a| > 4000 a_0$ [84]. Fitting the data to $K_3 = \eta \times (a/a_0)^4$ on both sides of the resonance, we find $\eta = (9.4 \pm 1.2) \times 10^{-37} \text{cm}^6/\text{s}$.

5.5 Conclusions

In conclusion, we have created weakly bound fermionic molecules near a heteronuclear Feshbach resonance and studied inelastic, atom-molecule loss processes. We observe that the quantum statistics of the particles strongly affects vibrational quenching rates of the molecules near the Feshbach resonance. Our data are consistent with the expectation that collisions between identical fermionic molecules are suppressed. This allows for lifetimes of the fermionic heteronuclear

molecules as long as 100 ms, which is at least ten times longer than required for coherent manipulation steps and opens the possibility of production of ultracold polar molecules. However, when bosonic atoms are available to collide with the molecules, we observe enhanced decay rates. Therefore, studies of the many-body behavior of a Bose-Fermi mixture near a Feshbach resonance may prove challenging.

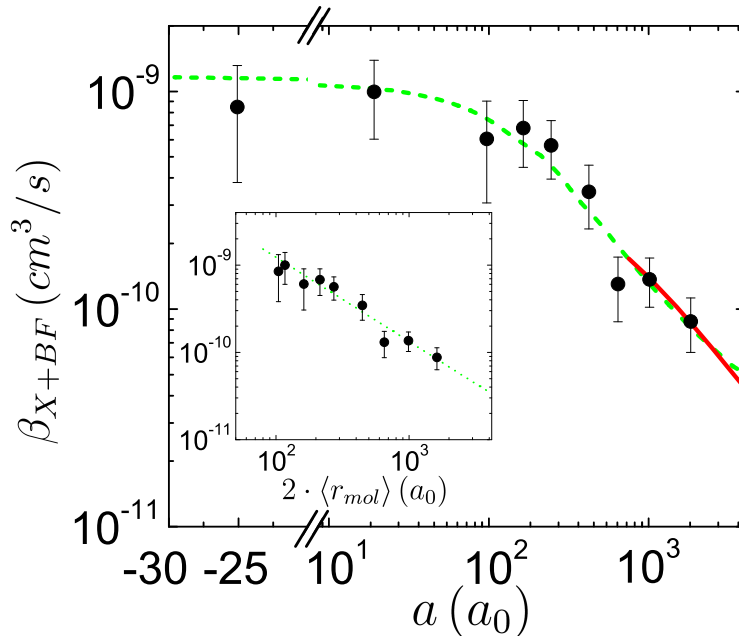


Figure 5.1: Molecule loss coefficient β for collisions with distinguishable atoms (K in the $|9/2, -7/2\rangle$ state) as a function of the heteronuclear scattering length. For large a , we observe β to decrease with increasing scattering length in agreement with numerical calculations (solid red curve). We observe β saturating for small a , ($a \sim 100 a_0$) where the molecular size, $\langle r_{mol} \rangle$, no longer has a strong dependence on a . Inset: β vs. molecule size $\langle r_{mol} \rangle$ as extracted from the measured binding energy of the Feshbach molecules [3]. The green dashed curve is a power law fit $\beta_{\text{fit}} \propto \langle r_{mol} \rangle^p$ to the experimental data; we obtain $p = -0.97 \pm 0.16$.

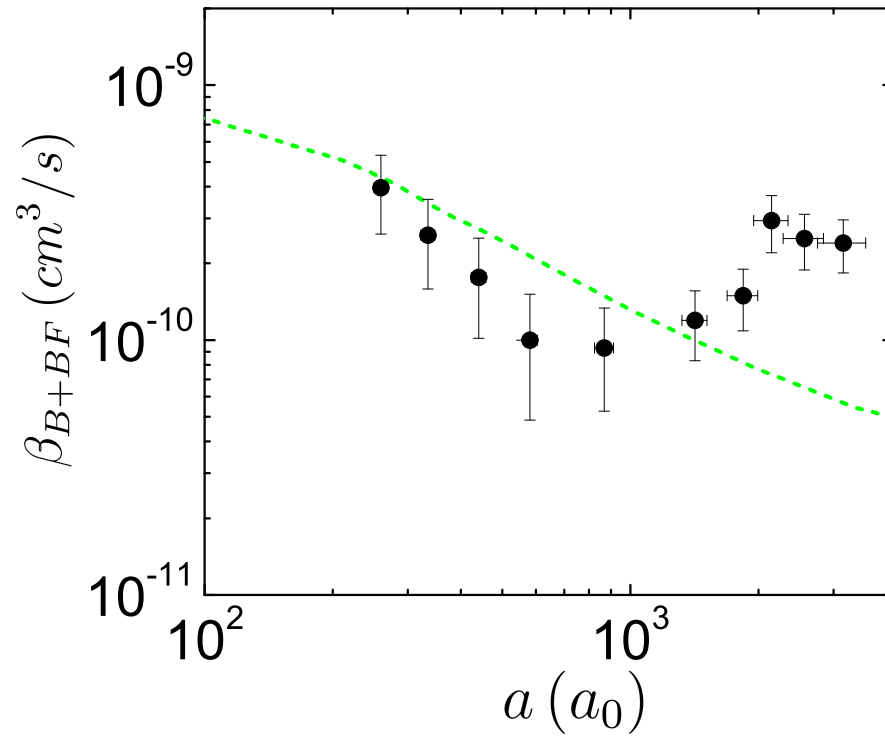


Figure 5.2: Molecule loss coefficient for collisions with indistinguishable bosons versus heteronuclear scattering length. For large a , β increases with increasing a . In this regime the molecular loss is enhanced compared to loss due to molecule collisions with distinguishable atoms (green dashed curve and Fig. 1). For small a , β increases with decreasing scattering length (see Section 5.3.2).

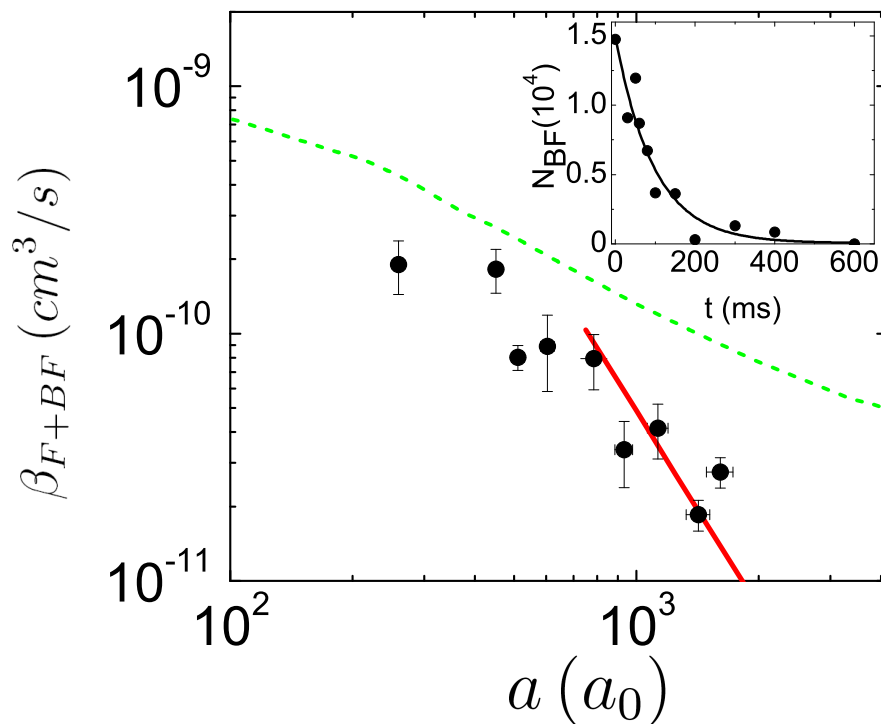


Figure 5.3: Molecule loss coefficient β for collisions with indistinguishable fermions. For large a we observe loss rates scaling as $a^{-1.6 \pm 0.2}$. The power law dependence is consistent with numerical calculations for this scattering length regime (solid red curve). In addition, the molecular loss is suppressed compared to inelastic decay of molecules due to collisions with distinguishable atoms (green dashed curve and Fig. 1). Inset: Molecule decay at $a \approx 1300 a_0$. The $1/e$ -lifetime of the molecular cloud is $\tau = 100 \pm 20$ ms

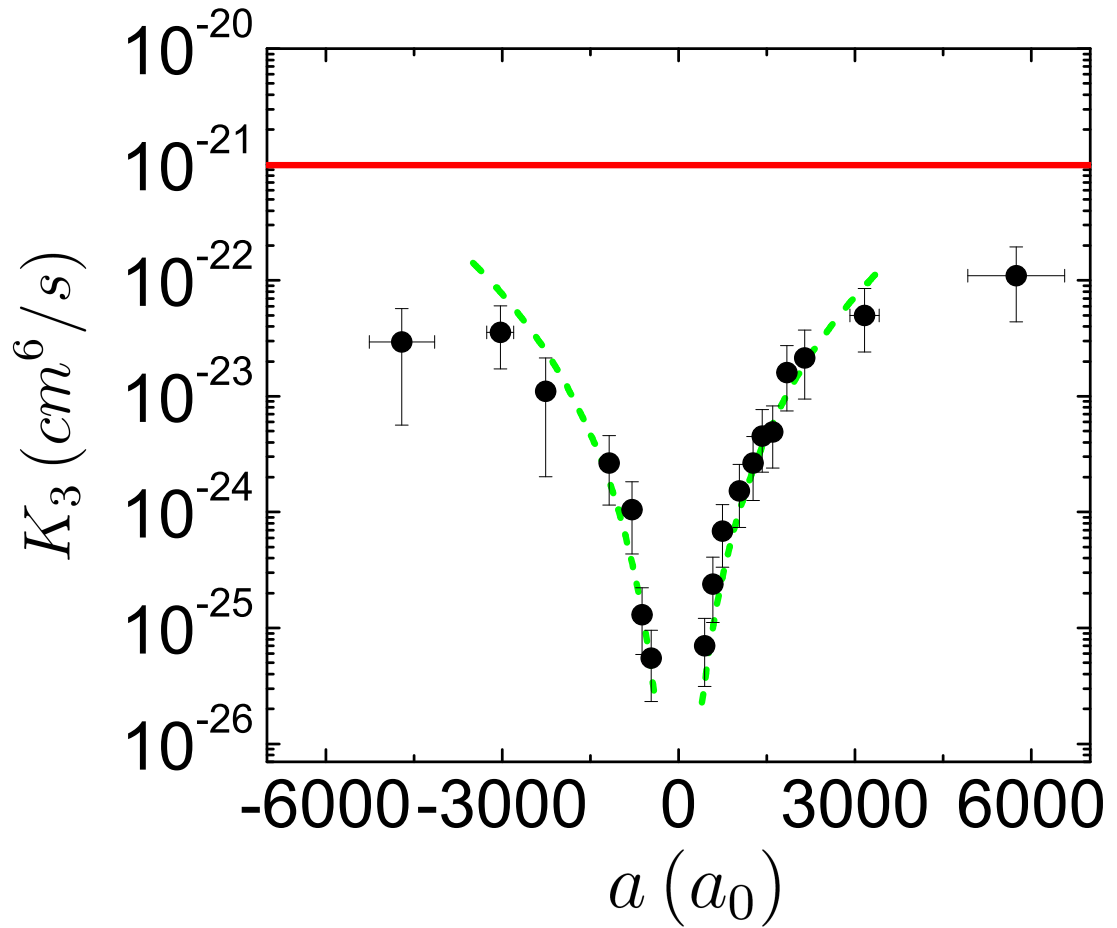


Figure 5.4: Three-body recombination near the heteronuclear Feshbach resonance. The measured K_3 varies as a^4 and saturates at large a due to the unitarity limit. The dashed curve is an a^4 fit to the data for $|a| < 4000 a_0$. The solid line is the unitarity limit at 150 nK.

Chapter 6

Conclusions and future directions

6.1 Conclusion

This thesis has presented work that has led to the creation of ultracold heteronuclear molecules from atomic gases of K and Rb. We used a magnetic-field tunable Feshbach resonance that affects interspecies collisions to associate atoms into loosely bound molecules. By measuring the molecular cloud position and its oscillations in the trap, we determined that the molecules were trapped by the optical trapping potential. Molecular properties such as binding energy, size, and temperature were characterized. Additionally, the inelastic atom-molecule collision properties were determined near the Feshbach resonance. It was shown that inelastic atom-molecule collisions were dramatically affected by not only the K+Rb scattering length but also by the quantum statistics of the atom involved in the atom-molecule collision. In particular, if the atom was a boson, we observed an increase in loss of molecules near the Feshbach resonance. If the atom was a fermion, we observed a decrease in the loss of molecules near the resonance. Finally, if the atom was distinguishable from the atoms in the molecule, we observed a decrease in the loss of molecules near the resonance but the suppression was not as pronounced as when the atom was a fermion.

This work is important for future studies because it characterized the Feshbach molecules that will be transferred to more deeply bound vibrational states of

the molecular potential. We also found that the molecules will need to be isolated from collisions with atoms as early as possible. If the intermediate-state molecules are allowed to collide with “distinguishable” atoms, their lifetimes will be greatly reduced. However, once inelastic collisions have been eliminated, the prospects look bright.

6.2 Future Work

At the time this thesis was written, there has already been considerable progress in our experiment toward the goal of producing more deeply bound molecules using STIRAP techniques [85]. These techniques rely on transferring the Feshbach molecules to a tightly bound molecular state using an intermediate, excited state.

At the very end of my work in the lab, we began driving transitions from the Feshbach molecule state to electronically excited states having an energy that was lower than the atomic D1 line of Rb. This induces loss of the Feshbach molecules when we tune the frequency of the laser to an excited vibrational state. A level diagram is shown in Fig. 6.1. The number of Feshbach molecules remaining after exciting them with different frequencies of light is shown in Fig. 6.2. Here we used an optical wavemeter to determine the frequency. Each minimum corresponds to different hyperfine state of an electronically excited vibrational level.

Choosing one of the excited states, we measured the loss rates of the Feshbach molecules caused by illuminating the molecules with the laser light. The results are shown in Fig. 6.3. The loss rates are high because of improved Franck-Condon overlap between the Feshbach molecule and the excited state. To estimate how much having Feshbach molecules has improved the Franck-Condon overlap, it is useful to compare the bound-bound transition rate of Fig. 6.3 to a free-bound transition rate. We measured the free-bound transition rate by preparing a mix-

ture of atoms under the same conditions as the Feshbach molecules except. We then illuminate the atom mixture with the laser light. The results are shown in Fig. 6.4. The ratio of the two time constants, τ , gives an estimate of the improvement in Franck-Condon overlap using Feshbach molecules instead of unbound atoms. The ratio is approximately 500.

In the future, STIRAP may be able to efficiently and coherently transfer the Feshbach molecules into the tightly bound rovibrational ground-state. Then one could consider looking for signatures of polar character in the final molecular states.

Such polar molecules will allow many studies of novel quantum dynamics that arise from anisotropic, long-range dipolar interactions between the molecules. For example, molecule-molecule interactions can be affected by applying an external electric field [86, 87]. Using these molecules confined to individual optical lattice sites, there are proposals to create quantum simulators of condensed matter systems [88, 89, 90]. Along the same lines, using ultracold polar molecules as qubits for a quantum computer has been proposed [10]. Ultracold, fermionic, polar molecules will certainly have an exciting future.

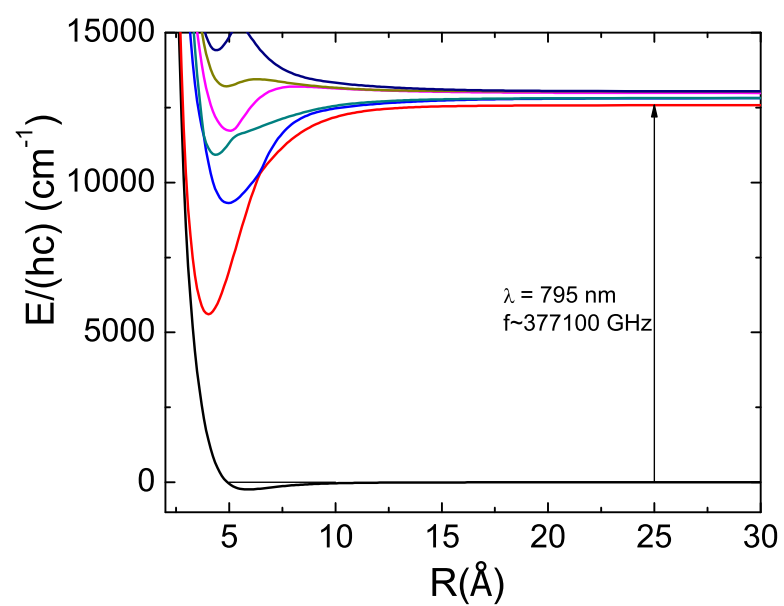


Figure 6.1: Diagram showing the laser frequency we initially used to find excited molecular states. The laser was tuned energies lower than the D1 line of atomic Rb. This corresponds to wavelengths longer than 795 nm.

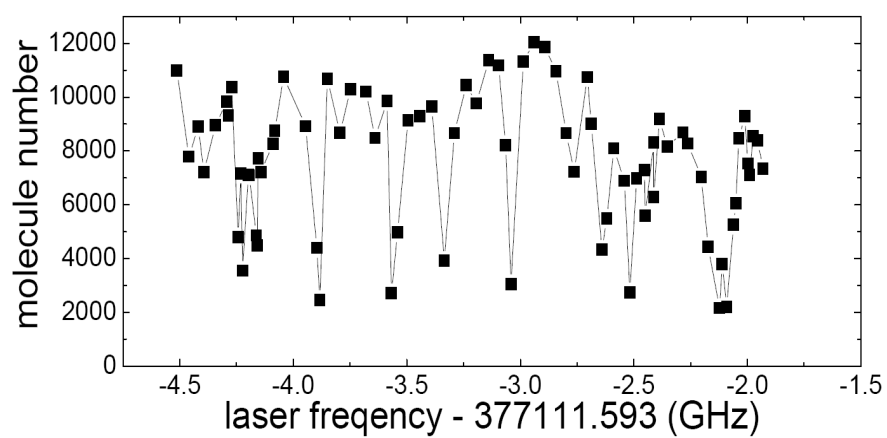


Figure 6.2: Observed molecule loss due to excitation to excited electronic states of the KRb molecule. Here we start with Feshbach molecules and illuminate them with laser light having the indicated frequency. The Feshbach molecules are lost when the laser light excites them to states where they spontaneously decay and are lost from the trap.

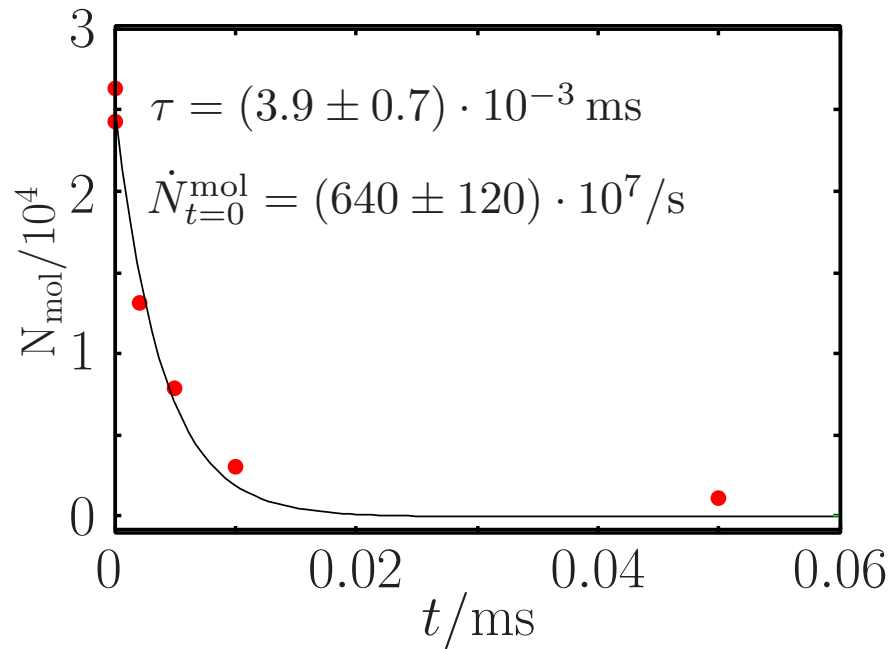


Figure 6.3: Loss of molecules in the Feshbach state resulting from optical excitation to an excited, bound molecular state of KRb. All experimental parameters were the same as in Fig. 6.4 except here, the initial state is the Feshbach molecular state instead of freely colliding atom pairs. Here, τ is shorter by a factor of 500 compared to freely colliding atom pairs.

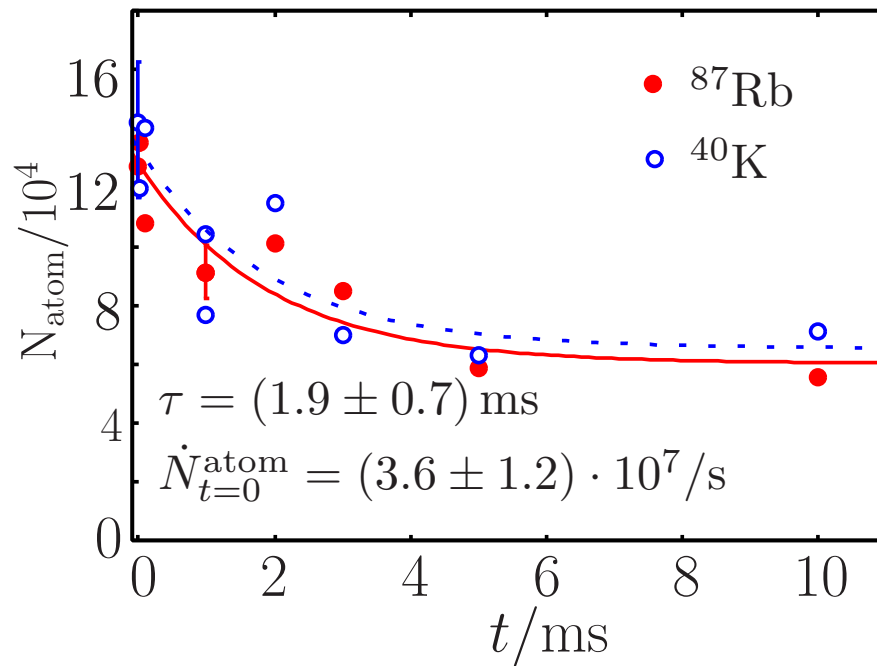


Figure 6.4: Loss of atoms resulting from photoassociation into an excited, bound molecular state of KRb. The τ for this data is about a factor of 500 longer than the data shown in Fig. 6.3.

Bibliography

- [1] S. Rousseau, A. R. Allouche, and M. Aubert-Frecon, Theoretical Study of the Electronic Structure of the KRb Molecule, *J. Mol. Spectrosc.* **203**, 235 (2000).
- [2] G. F. Gribakin and V. V. Flambaum, Calculation of the scattering length in atomic collisions using the semiclassical approximation, *Phys. Rev. A* **48**, 546 (1993).
- [3] J. J. Zirbel, K.-K. Ni, S. Ospelkaus, T. L. Nicholson, M. L. Olsen, C. E. Wieman, J. Ye, D. S. Jin, and P. S. Julienne, Heteronuclear molecules in an optical dipole trap, *Phys. Rev. A*, *in press*, *arXiv:0712.3889v1* (2007).
- [4] P. G. H. Sandars, Measurability of the Proton Electric Dipole Moment, *Phys. Rev. Lett.* **19**, 1396 (1967).
- [5] M. G. Kozlov and L. N. Labzowsky, Parity violation effects in diatomics, *J. Phys. B: At. Mol. Opt. Phys.* **28**, 1933 (1995).
- [6] E. R. Hudson, H. J. Lewandowski, B. C. Sawyer, and J. Ye, Cold Molecule Spectroscopy for Constraining the Evolution of the Fine Structure Constant, *Phys. Rev. Lett.* **96**, 142004 (2006).
- [7] S. M. Blinder, Dipole Moment of HD, *J. Chem. Phys.* **32**, 105 (1960).
- [8] M. Trefler and H. P. Gush, Electric Dipole Moment of HD, *Phys. Rev. Lett.* **20**, 703 (1968).
- [9] S. Lepp and J. Shull, Molecules in the early universe, *Ap. J.* **280**, 465 (1984).
- [10] D. DeMille, Quantum Computation with Trapped Polar Molecules, *Phys. Rev. Lett.* **88**, 067901 (2002).
- [11] H. L. Bethlem, G. Berden, and G. Meijer, Decelerating Neutral Dipolar Molecules, *Phys. Rev. Lett.* **83**, 1558 (1999).
- [12] B. C. Sawyer, B. L. Lev, E. R. Hudson, B. K. Stuhl, M. Lara, J. L. Bohn, and J. Ye, Magnetoelectrostatic Trapping of Ground State OH Molecules, *Phys. Rev. Lett.* **98**, 253002 (2007).

- [13] J. D. Weinstein, R. deCarvalho, T. Guillet, B. Friedrich, and J. M. Doyle, Magnetic trapping of calcium monohydride molecules at millikelvin temperatures, *Nature* **395**, 148 (1998).
- [14] S. A. Rangwala, T. Junglen, T. Rieger, P. W. H. Pinkse, and G. Rempe, Continuous source of translationally cold dipolar molecules, *Phys. Rev. A* **67**, 043406 (2003).
- [15] H. R. Thorsheim, J. Weiner, and P. S. Julienne, Laser-Induced Photoassociation of Ultracold Sodium Atoms, *Phys. Rev. Lett.* **58**, 2420 (1987).
- [16] A. J. Kerman, J. M. Sage, S. Sainis, T. Bergeman, and D. DeMille, Production and State-Selective Detection of Ultracold RbCs Molecules, *Phys. Rev. Lett.* **92**, 153001 (2004).
- [17] J. Kleinert, C. Haimberger, P. J. Zabawa, and N. P. Bigelow, Trapping of Ultracold Polar Molecules with a Thin-Wire Electrostatic Trap, *Phys. Rev. Lett.* **99**, 143002 (2007).
- [18] S. J. J. M. F. Kokkelmans, H. M. J. Vissers, and B. J. Verhaar, Formation of a Bose condensate of stable molecules via a Feshbach resonance, *Phys. Rev. A* **63**, 031601(R) (2001).
- [19] T. Kohler, K. Goral, and P. S. Julienne, Production of cold molecules via magnetically tunable Feshbach resonances, *Rev. Mod. Phys.* **78**, 1311 (2006).
- [20] C. E. Wieman, D. E. Pritchard, and D. J. Wineland, Atom cooling, trapping, and quantum manipulation, *Rev. Mod. Phys.* **71**, S253 (1999).
- [21] W. D. Phillips, Nobel Lecture: Laser cooling and trapping of neutral atoms, *Rev. Mod. Phys.* **70**, 721 (1998).
- [22] S. Chu, The manipulation of neutral particles, *Rev. Mod. Phys.* **70**, 685 (1998).
- [23] C. N. Cohen-Tannoudji, Manipulating atoms with photons, *Rev. Mod. Phys.* **70**, 707 (1998).
- [24] E. A. Cornell and C. E. Wieman, Nobel Lecture: Bose-Einstein condensation in a dilute gas, the first 70 years and some recent experiments, *Rev. Mod. Phys.* **74**, 875 (2002).
- [25] W. Ketterle, Nobel lecture: When atoms behave as waves: Bose-Einstein condensation and the atom laser, *Rev. Mod. Phys.* **74**, 1131 (2002).
- [26] B. DeMarco and D. S. Jin, Onset of Fermi degeneracy in a trapped atomic gas, *Science* **285**, 1703 (1999).

- [27] B. DeMarco, Quantum behavior of an atomic Fermi gas, Ph.D. thesis, University of Colorado - Boulder, 2001.
- [28] D. M. Eagles, Possible pairing without superconductivity at low carrier concentrations in bulk and thin-film superconducting semiconductors, *Phys. Rev.* **186**, 456 (1969).
- [29] P. Nozieres and S. Schmitt-Rink, Bose condensation in an attractive fermion gas: From weak to strong coupling superconductivity, *J. Low-Temp. Phys.* **59**, 195 (1985).
- [30] A. J. Leggett, Superfluidity, *Rev. Mod. Phys.* **71**, S318 (1999).
- [31] M. Holland, S. J. J. M. F. Kokkelmans, M. L. Chiofalo, and R. Walser, Resonance Superfluidity in a Quantum Degenerate Fermi Gas, *Phys. Rev. Lett.* **87**, 120406 (2001).
- [32] M. L. Chiofalo, S. J. J. M. F. Kokkelmans, J. N. Milstein, and M. J. Holland, Signatures of Resonance Superfluidity in a Quantum Fermi Gas, *Phys. Rev. Lett.* **88**, 090402 (2002).
- [33] Y. Ohashi and A. Griffin, BCS-BEC Crossover in a Gas of Fermi Atoms with a Feshbach Resonance, *Phys. Rev. Lett.* **89**, 130402 (2002).
- [34] C. A. Regal, M. Greiner, and D. S. Jin, Observation of Resonance Condensation of Fermionic Atom Pairs, *Phys. Rev. Lett.* **92**, 040403 (2004).
- [35] M. W. Zwierlein, C. A. Stan, C. H. Schunck, S. M. F. Raupach, A. J. Kerman, and W. Ketterle, Condensation of Pairs of Fermionic Atoms near a Feshbach Resonance, *Phys. Rev. Lett.* **92**, 120403 (2004).
- [36] J. J. Zirbel, K.-K. Ni, S. Ospelkaus, J. P. D’Incao, C. E. Wieman, J. Ye, and D. S. Jin, Collisional Stability of Fermionic Feshbach Molecules, *Phys. Rev. Lett.* **100**, 143201 (2008).
- [37] S. B. Papp, Experiments with a two-species Bose-Einstein condensate utilizing widely tunable interparticle interactions, Ph.D. thesis, University of Colorado-Boulder, 2008.
- [38] S. Kobayashi and T. Kimura, Injection locking in AlGaAs semiconductor laser, *Quantum Electronics, IEEE Journal of* **17**, 681 (1981).
- [39] B. Dahmani, L. Hollberg, and R. Drullinger, Frequency stabilization of semiconductor lasers by resonant optical feedback, *Opt. Lett.* **12**, 876 (1987).
- [40] T. Pawletko, M. Houssin, M. Knoop, M. Vedel, and F. Vedel, High power broad-area diode laser at 794 nm injected by an external cavity laser, *Optics Communications* **174**, 223 (2000).

- [41] Y. Ishikawa, T. Yoshimura, and M. Arai, Effect of surface oxide layers on deuterium permeation through stainless steels with reference to outgassing reduction in ultra- to extremely high vacuum, *Vacuum* **47**, 357 (1996).
- [42] L. Westerberg, B. Hjrvarsson, E. Walln, and A. Mathewson, Hydrogen content and outgassing of air-baked and vacuum-fired stainless steel, *Vacuum* **48**, 771 (1997).
- [43] B. DeMarco, H. Rohner, and D. Jin, An enriched ^{40}K source for fermionic atom studies, *Rev. Sci. Instrum.* **70**, 1967 (1999).
- [44] D. E. Pritchard, Cooling Neutral Atoms in a Magnetic Trap for Precision Spectroscopy, *Phys. Rev. Lett.* **51**, 1336 (1983).
- [45] T. L. Nicholson, Optical Trapping in a Cold Molecule Experiment, 2006.
- [46] S. B. Papp and C. E. Wieman, Observation of Heteronuclear Feshbach Molecules from a ^{85}Rb - ^{87}Rb Gas, *Phys. Rev. Lett.* **97**, 180404 (2006).
- [47] S. B. Papp, J. M. Pino, and C. E. Wieman, Studying a dual-species BEC with tunable interactions, *arXiv:0802.2591v1* (2008).
- [48] E. Hodby, S. T. Thompson, C. A. Regal, M. Greiner, A. C. Wilson, D. S. Jin, E. A. Cornell, and C. E. Wieman, Production Efficiency of Ultracold Feshbach Molecules in Bosonic and Fermionic Systems, *Phys. Rev. Lett.* **94**, 120402 (2005).
- [49] W. Petrich, M. H. Anderson, J. R. Ensher, and E. A. Cornell, Behavior of atoms in a compressed magneto-optical trap, *J. Opt. Soc. Am. B* **11**, 1332 (1994).
- [50] H. J. Lewandowski, D. M. Harber, D. L. Whitaker, and E. A. Cornell, Simplified System for Creating a Bose-Einstein Condensate, *J. Low Temp. Phys.* **132**, 309 (2003).
- [51] H. J. Metcalf and P. van der Straten, *Laser Cooling and Trapping* (Spring, New York, 1999).
- [52] J. L. Roberts, Bose-Einstein condensates with tunable atom-atom interactions: The first experiments with ^{85}Rb BECs, Ph.D. thesis, University of Colorado - Boulder, 2001.
- [53] S. L. Cornish, N. R. Claussen, J. L. Roberts, and E. A. C. and C. E. Wieman, Stable ^{85}Rb Bose-Einstein condensates with widely tunable interactions, *Phys. Rev. Lett.* **85**, 1795 (2000).
- [54] T. Weber, J. Herbig, M. Mark, H.-C. Ngerl, and R. Grimm, Three-Body Recombination at Large Scattering Lengths in an Ultracold Atomic Gas, *Phys. Rev. Lett.* **91**, 123201 (2003).

- [55] J. L. Roberts, J. P. Burke, Jr., N. R. Claussen, S. L. C. E. A. Donley, and C. E. Wieman, Improved characterization of elastic scattering near a Feshbach resonance in ^{85}Rb , *Phys. Rev. A* **64**, 024702 (2001).
- [56] J. L. Roberts, N. R. Claussen, S. L. Cornish, E. A. D. and E. A. Cornell, and C. E. Wieman, Controlled collapse of a Bose-Einstein condensate, *Phys. Rev. Lett.* **86**, 4211 (2001).
- [57] N. R. Claussen, E. A. Donley, S. T. Thompson, and C. E. Wieman, Microscopic dynamics in a strongly interacting Bose-Einstein condensate, *Phys. Rev. Lett.* **89**, 010401 (2002).
- [58] E. A. Donley, N. R. Claussen, S. T. Thompson, and C. E. Wieman, Atom-molecule coherence in a Bose-Einstein condensate, *Nature* **417**, 529 (2002).
- [59] C. A. Regal, C. Ticknor, J. L. Bohn, and D. S. Jin, Creation of ultracold molecules from a Fermi gas of atoms, *Nature* **424**, 47 (2003).
- [60] J. Stenger, S. Inouye, M. R. Andrews, H.-J. Miesner, D. M. Stamper-Kurn, and W. Ketterle, Strongly Enhanced Inelastic Collisions in a Bose-Einstein Condensate near Feshbach Resonances, *Phys. Rev. Lett.* **82**, 2422 (1999).
- [61] S. T. Thompson, E. Hodby, and C. E. Wieman, Ultracold Molecule Production via a Resonant Oscillating Magnetic Field, *Phys. Rev. Lett.* **95**, 190404 (2005).
- [62] J. P. Gaebler, J. T. Stewart, J. L. Bohn, and D. S. Jin, p-Wave Feshbach Molecules, *Phys. Rev. Lett.* **98**, 200403 (2007).
- [63] C. Ospelkaus, S. Ospelkaus, L. Humbert, P. Ernst, K. Sengstock, and K. Bongs, Ultracold Heteronuclear Molecules in a 3D Optical Lattice, *Phys. Rev. Lett.* **97**, 120402 (2006).
- [64] S. Inouye, J. Goldwin, M. L. Olsen, C. Ticknor, J. L. Bohn, and D. S. Jin, Observation of Heteronuclear Feshbach Resonances in a Mixture of Bosons and Fermions, *Phys. Rev. Lett.* **93**, 183201 (2004).
- [65] F. Ferlaino, C. D'Errico, G. Roati, M. Zaccanti, M. Inguscio, G. Modugno, and A. Simoni, Feshbach spectroscopy of a K-Rb atomic mixture, *Phys. Rev. A* **73**, 040702 (2006).
- [66] C. Ticknor, C. A. Regal, D. S. Jin, and J. L. Bohn, Multiplet structure of Feshbach resonances in nonzero partial waves, *Phys. Rev. A* **69**, 042712 (2004).
- [67] D. S. Petrov, C. Salomon, and G. V. Shlyapnikov, Weakly Bound Dimers of Fermionic Atoms, *Phys. Rev. Lett.* **93**, 090404 (2004).

- [68] C. A. Regal, M. Greiner, and D. S. Jin, Lifetime of Molecule-Atom Mixtures near a Feshbach Resonance in K, *Phys. Rev. Lett.* **92**, 083201 (2004).
- [69] S. T. Thompson, E. Hodby, and C. E. Wieman, Spontaneous Dissociation of ^{85}Rb Feshbach Molecules, *Phys. Rev. Lett.* **94**, 020401 (2005).
- [70] T. Kohler, T. Gasenzer, and K. Burnett, Microscopic theory of atom-molecule oscillations in a Bose-Einstein condensate, *Phys. Rev. A* **67**, 013601 (2003).
- [71] A. J. Moerdijk, B. J. Verhaar, and A. Axelsson, Resonances in ultracold collisions of ^6Li , ^7Li , and ^{23}Na , *Phys. Rev. A* **51**, 4852 (1995).
- [72] F. H. Mies, E. Tiesinga, and P. S. Julienne, Manipulation of Feshbach resonances in ultracold atomic collisions using time-dependent magnetic fields, *Phys. Rev. A* **61**, 022721 (2000).
- [73] A. Pashov, O. Docenko, M. Tamanis, R. Ferber, H. Knockel, and E. Tiemann, Coupling of the $X^1\Sigma^+$ and $a^3\Sigma^+$ states of KRb, *Phys. Rev. A* **76**, 022511 (2007).
- [74] H. Suno, B. D. Esry, C. H. Greene, and J. P. Burke, Three-body recombination of cold helium atoms, *Phys. Rev. A* **65**, 042725 (2002).
- [75] V. A. Yurovsky, A. Ben-Reuven, P. S. Julienne, and C. J. Williams, Atom loss from Bose-Einstein condensates due to Feshbach resonance, *Phys. Rev. A* **60**, R765 (1999).
- [76] D. V. Efremov and L. Viverit, p -wave Cooper pairing of fermions in mixtures of dilute Fermi and Bose gases, *Phys. Rev. B* **65**, 134519 (2002).
- [77] J. Doyle, B. Friedrich, R. V. Krems, and F. Masnou-Seeuws, Quo vadis, cold molecules? - Editorial review, *Eur. Phys. J. D* **31**, 149 (2004).
- [78] J. P. D’Incao and B. D. Esry, Suppression of molecular decay in ultracold gases without Fermi statistics, *arXiv:0711.3238v1* (2007).
- [79] J. P. D’Incao and B. D. Esry, Mass dependence of ultracold three-body collision rates, *Phys. Rev. A* **73**, 030702 (2006).
- [80] J. P. D’Incao and B. D. Esry, Scattering Length Scaling Laws for Ultracold Three-Body Collisions, *Phys. Rev. Lett.* **94**, 213201 (2005).
- [81] E. Braaten and H.-W. Hammer, Enhanced dimer relaxation in an atomic and molecular Bose-Einstein condensate, *Phys. Rev. A* **70**, 042706 (2004).
- [82] E. Braaten and H.-W. Hammer, Universality in few-body systems with large scattering length, *Phys. Rep.* **428**, 259 (2006).

- [83] T. Kraemer *et al.*, Evidence for Efimov quantum states in an ultracold gas of caesium atoms, *Nature* **440**, 315 (2006).
- [84] J. P. D’Incao, H. Suno, and B. D. Esry, Limits on Universality in Ultracold Three-Boson Recombination, *Phys. Rev. Lett.* **93**, 123201 (2004).
- [85] S. Ospelkaus, A. Pe’er, K.-K. Ni, J. J. Zirbel, B. Neyenhuis, S. Kotochigova, P. S. Julienne, J. Ye, and D. S. Jin, Efficient state transfer in an ultracold dense gas of heteronuclear molecules, *Nat Phys* **advanced online publication**, (2008).
- [86] C. Ticknor and J. L. Bohn, Long-range scattering resonances in strong-field-seeking states of polar molecules, *Phys. Rev. A* **72**, 032717 (2005).
- [87] C. Ticknor, Collisional Control of Ground State Polar Molecules and Universal Dipolar Scattering, *Phys. Rev. Lett.* **100**, 133202 (2008).
- [88] B. Sun and L. You, Observing the Einstein–de Haas Effect with Atoms in an Optical Lattice, *Phys. Rev. Lett.* **99**, 150402 (2007).
- [89] M. Lewenstein, A. Sanpera, V. Ahufinger, B. Damski, A. Sen, and U. Sen, Ultracold atomic gases in optical lattices: mimicking condensed matter physics and beyond, *Advances in Physics* **56**, 243 (2007).
- [90] G. Pupillo, A. Griessner, A. Micheli, M. Ortner, D.-W. Wang, and P. Zoller, Cold Atoms and Molecules in Self-Assembled Dipolar Lattices, *Phys. Rev. Lett.* **100**, 050402 (2008).

Appendix A

Magnetic Trap Trouble

In the summer of 2006 our new Ioffe-Pritchard trap failed. This failure showed itself after we abused the trap by not cooling the Ioffe bars and pinch coils during just one experimental cycle. The abuse itself wasn't enough to burn the coils but it was clear that at least one coil did not function properly afterwards.

The symptoms of failure were consistent with the Ioffe bar coils either having an electrical short or moving vertically. This was because the atoms' position were randomly shifting vertically after every experimental cycle. The position shifts had a standard deviation of about $10\ \mu\text{m}$. This could be caused either by an intermittent electrical short or by the coil itself was somehow shifting vertically shot-to-shot.

We naively suspected that a short between two windings of a coil would cause all of the current to flow to avoid the shorted winding. Such a short would've caused our atom cloud to be shifted by about a millimeter. This large of a shift was not observed. In addition, when we measured the resistances of the coils during experimental cycles, they agreed with the expected resistance to much better than the resistance of a single winding of the coil. This suggested that the coil wasn't shorted.

Another alternative was that the coil had a winding break free from the bulk of the coil and it was randomly shifting after each experimental cycle from

the relatively strong magnetic forces. This explanation was nice because it agreed with the qualitative observation that the atoms were shifting randomly. However, the position fluctuations of the atoms were much larger than we could expect from reasonable movement of all of the windings. This made the movement requirement of just the one winding even larger. We measured that the entire coil moved by less than $6 \mu\text{m}$ during and after each experimental cycle.

As it turned out, the correct answer was probably a combination of the two. In the Ioffe coil below the cell, we had an intermittent short but not a *complete* short. Such a short changed slightly after each experimental cycle due to minute changes of the shorted windings' relative positions caused by magnetic forces. This explanation was supported by evidence that the coil's resistance was changing up to 0.2% after each experimental cycle. These shifts in resistance were so small that they were initially masked by fluctuations in the resistance from temperature changes of the water. Since copper's thermal coefficient of resistance is about $\eta_{\text{Cu}} = 0.39\%/K$, only a small temperature shift would cause a similar resistance shift. To account for this effect, we simultaneously measured the resistance and temperature of the coils. In Fig. A.1 I have plotted the resistance of the coil versus the water temperature. The family of lines all have slopes that are consistent with the thermal coefficient of resistance for copper. Each transition from one line to the other occurred after mechanical perturbations of the bottom Ioffe coil such as moving the coil's leads by hand or tightening retaining screws. These resistance changes were about 5 times larger than when the coil's current was cycled normally in an experimental sequence.

We also measured the position of the cloud and found that it too was correlated to resistance shifts of the coil. Figure A.2 shows this correlation. The effect of the coil's temperature on the resistance has been accounted for and subtracted in this measurement. We measured the linear slope of the data to be

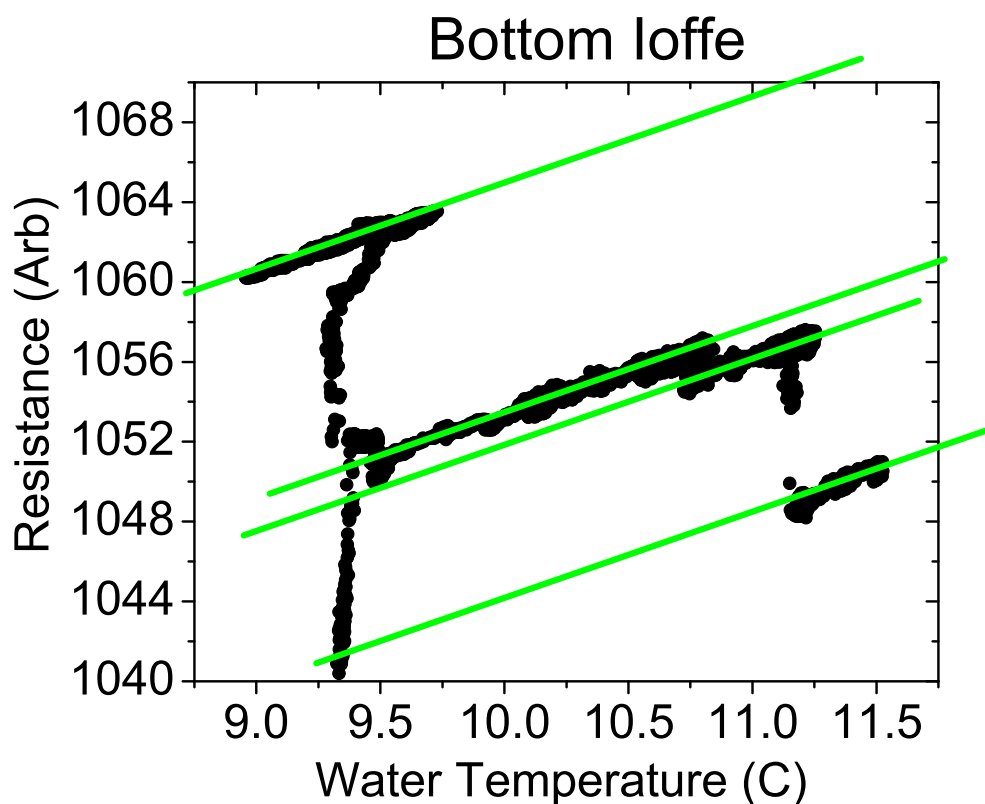


Figure A.1: The resistance of the coil plotted against the temperature of the water flowing through the coil. The slope of the curves is consistent with the thermal coefficient of resistance of copper. The vertical resistance shifts are caused by mechanical perturbations of the coil. These shifts are relatively small at about 1% of the total resistance of the coil. For comparison, if a complete winding were shorted, it would have a shift 13 times larger.

about $70 \pm 15 \mu\text{m}/\%$ which is roughly consistent with the slope predicted by a numerical calculation.

These observations led to further inspection of the coils. We learned that the short was probably caused by the initial winding procedure for the Ioffe coils. Because of the geometry of the Ioffe coil, there is a transition region for the coil's interior lead that circumvents the rest of the coil (See Fig. A.3). This region causes the edges of adjacent copper tubes to slip past and press into one another during winding. This pressure causes the polyimide (Kapton [®]) coating to rub off at this region and is particularly bad for the tubing we used because of its square cross-section, which has a relatively sharp edge.

It is remarkable and insidious how weakly the adjacent windings were shorted. Presumably the polyimide's adhesive was providing enough resistance to prevent a full electrical short. Since the slippage past the two tubes caused the short, we fixed this by wrapping the bad location with more polyimide after winding the coil. After the fix, we performed the same set of tests on the bottom Ioffe coil and found no problems. However, even though we checked all of the coils, they could still have similar problems that have not yet presented themselves.

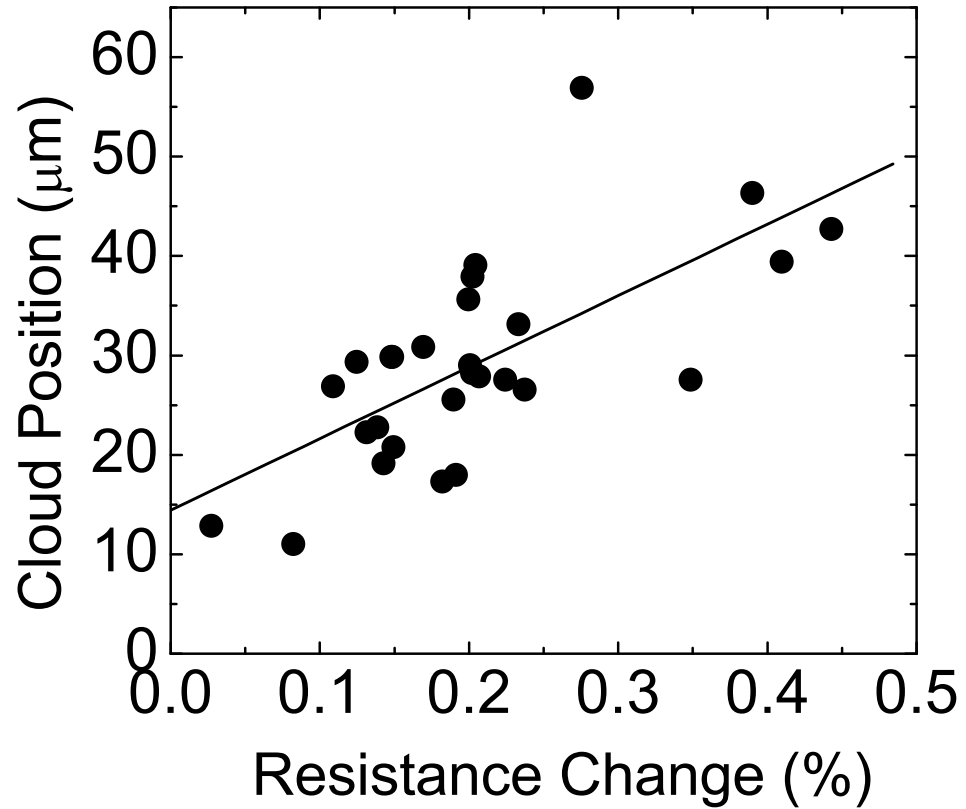


Figure A.2: Correlation between the cloud's measured position and percent resistance change. The data was taken after releasing from the magnetic trap for 15ms of free expansion. The slope is roughly consistent with the slope predicted by a numerical calculation.

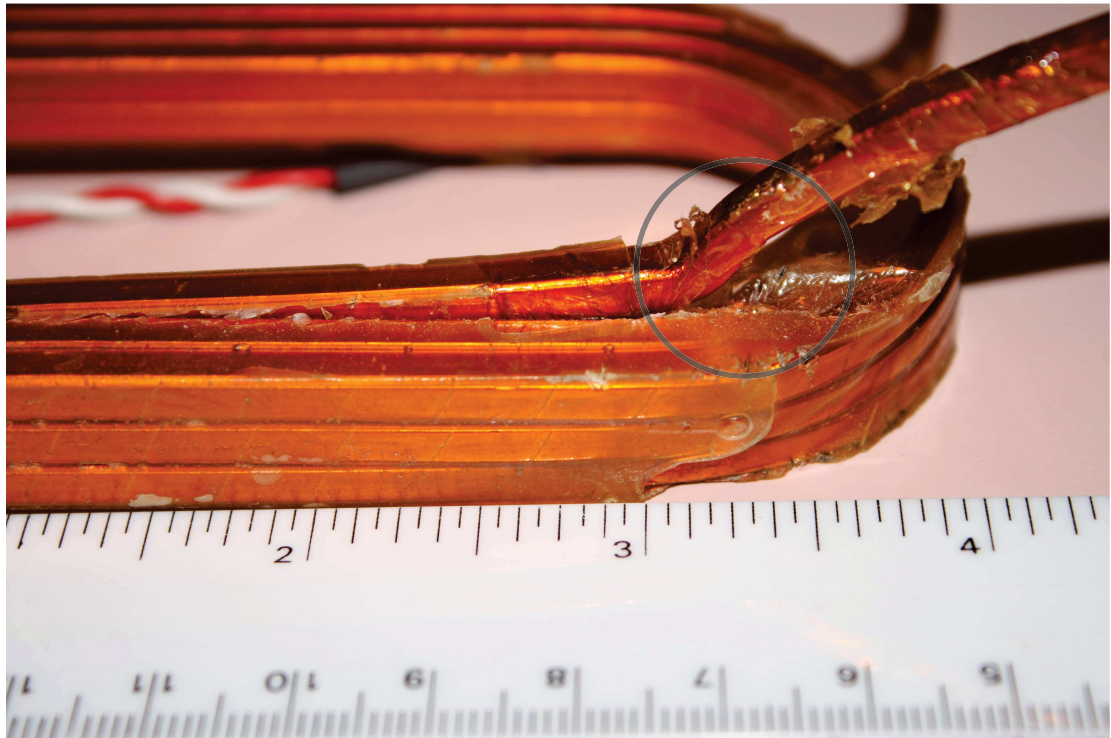


Figure A.3: A view of the Ioffe coil's problematic lead. The pressure between the wires at this transition point caused an incomplete short to other windings through the polyimide coating.